NASA-CR-201976

NACW-3150

STUDY OF THE RADIATIVE PROPERTIES OF INHOMOGENEOUS

STRATOCUMULUS CLOUDS

A Thesis

Submitted to the Faculty

of

Purdue University

by

Michael Batey

In Partial Fulfillment of the

Requirements for the Degree

of

Master of Science

August 1996

ACKNOWLEDGMENTS

I first give thanks to the God of Heaven for allowing me to continue my education. I also would like to thank my father and mother for the support and encouragement they have given me over the past two years.

I am grateful to Dr. Harshvardhan for seeing my potential, and having the time and patience to direct me in my education and research. I also thank my committee members Dr. Petty and Dr. Clayson for their help and suggestions in the final stages of my thesis.

A special thanks must be extended to Dr. Steve Gollmer a great friend and support with whose guidance helped me handle a very hard to understand research topic.

I would like to give my appreciation to Bob Green and Dan Vietor for the many times they were able to help me with difficult computer questions. Especially to Bob who would be very patient with all the frustrations I had and then willing to take the time to solve them.

I thank Jon Schrage for all his encouragement, for his friendship and for helping me with a wide array of difficult personal computer questions. I also thank Jim Vasilj and Mark Conner, along with Jon, for all of the good times we were able to have together.

I would like to recognize the members of the Radiation Group especially Jaya for helping to liven and lighten up the many long nights in front of the computers. To Ray Espinoza who was always willing for a quick chat whenever I would stop by his office. Finally to Surabi Menon for lightening up my time here in the first couple of semesters.

TABLE OF CONTENTS

LIST OF TABLES

LIST OF FIGURES

ABSTRACT

Batey, Michael. M.S.. Purdue University. August, 1996. Study of the Radiative Properties of Inhomogeneous Stratocumulus Clouds. Major Professor: Harshvardhan

Clouds play an important role in the radiation budget of the atmosphere. A good understanding of how clouds interact with solar radiation is necessary when considering their effects in both general circulation models and climate models.

This study examined the radiative properties of clouds in both an inhomogeneous cloud system, and a simplified cloud system through the use of a Monte Carlo model. The purpose was to become more familiar with the radiative properties of clouds, especially absorption, and to investigate the excess absorption of solar radiation from observations over that calculated from theory. The first cloud system indicated that the absorptance actually decreased as the cloud's inhomogeneity increased, and that cloud forcing does not indicate any changes.

The simplified cloud system looked at two different cases of absorption of solar radiation in the cloud. The absorptances calculated from the Monte Carlo is compared to a correction method for calculating absorptances and found that the method can over or underestimate absorptances at cloud edges. Also the cloud edge effects due to solar radiation points to a possibility of overestimating the retrieved optical depth at the edge, and indicates a possible way to correct for it. The effective cloud fraction (N_e) for a long time has been calculated from a cloud's reflectance. From the reflectance it has been observed that the N_e for most cloud geometries is greater than the actual cloud fraction (N_C) making a cloud appear wider than it is optically. Recent studies we have performed used a Monte Carlo model to calculate the N_e of a cloud using not only the reflectance but

also the absorptance. The derived N_e's from the absorptance in some of the Monte Carlo runs did not give the same results as derived from the reflectance.

This study also examined the inhomogeneity of clouds to find a relationship between larger and smaller scales, or wavelengths, of the cloud. Both Fourier transforms and wavelet transforms were used to analyze the liquid water content of marine stratocumulus clouds taken during the ASTEX project. From the analysis it was found that the energy in the cloud is not uniformly distributed but is greater at the larger scales than at the smaller scales. This was determined by examining the slope of the power spectrum, and by comparing the variability at two scales from a wavelet analysis.

CHAPTER 1. INTRODUCTION

Clouds are an integral part of the earth-atmosphere system. As such, clouds play a major role in the many changes brought about by the subsystems existing between the earth and its atmosphere. One of those subsystems is the hydrological cycle. This is the process by which water evaporates, rises, and condenses to become clouds. They then complete the cycle by returning the condensed water back to the earth's surface as precipitation. On the meso-scale, clouds can interact with even the smallest region by taking the form of thunderstorms.

Another subsystem with which clouds interact is that of the earth's solar energy. Clouds reflect a percentage of the sun's radiation back to space and at the same time absorb both solar and infra-red (IR) radiation. These interactions play a big part in the earth's energy budget.

The role that clouds play in absorbing solar radiation has been under considerable study for at least the last four decades. One of the first experiments of cloud solar absorption was done by Fritz and MacDonald (1951), who looked at cloud optical properties in many different locations across the US. These studies were carried out both by airborne and ground based instruments. At each of these locations the value of absorption of solar radiation by clouds was measured and in each case the absorption was significantly greater than those shown in the theoretical calculations.

Since Fritz and MacDonald's observations on solar radiation by clouds there have been many more studies to examine and to understand why this discrepancy exists. Stephens and Tsay (1990) compiled data on studies based on aircraft borne instrument measurements completed over the past four decades. This study examined possible causes for excess absorption and expressed some uncertainties in the absorption.

Some of the more recent studies on excess cloud absorption were done by Cess et al. (1995), Ramanathan et al. (1995), Pilewskie and Valero (1995), Chou et al. (1995), and Harshvardhan et al. (1996). These studies focused on the ratio of cloud forcing at the surface, CF^{SFC}, to cloud forcing above the cloud layer, CF^{TOA}. Cloud forcing is the difference between cloudy-sky and clear-sky net SW fluxes. A value greater than unity (or 1.0) for the cloud forcing ratio, CF^{SFC}/ CF^{TOA}, implies that clouds absorb greater amounts of solar radiation. The first three studies showed that the cloud forcing ratio was greater than one. In fact, it averaged 1.5. This is greater than the value calculated by radiative transfer models which was close to unity.

Ramanathan et al. (1995) looked at the heat budget of the Pacific warm pool and deduced that cloud absorption is needed to balance the energy budget in that region. Cess et al. (1995) examined satellite and surface measurements of solar radiation at different locations throughout the globe and compared them with model calculations. They found that across the globe the models underpredicted the absorption of solar radiation by 25 $W\ m^{-2}$ when compared to actual measurements. Pilewskie and Valero used measurements from aircraft that flew during TOGA-COARE and CEPEX. Their results were the same showing that clouds absorb more solar radiation than theoretically expected. Chou et al. (1995) used a radiation model to conclude that in order to reach a ratio of 1.5 the cloud specific absorption, $1 - \varpi_o$, in a model using theoretical values would have to be increased beyond the measurements taken from aircraft. Harshvardhan et al. (1996) discussed the need to study different spectral regions in order to address some of the cloud absorption uncertainties, as well as the necessity of including the effects of horizontal inhomogeneities.

It is still unknown whether the excess absorption of clouds in the real atmosphere is due to their inhomogeneities. It has actually been observed by Davies et al. (1984), and Harshvardhan et al. (1996) that the more inhomogeneous a modeled cloud is the less the cloud will absorb. However, these cloud absorption studies have been comparing measurements of inhomogeneous clouds to theoretical values found from plane-parallel clouds.

Clouds have always been modeled as homogeneous plane-parallel clouds in general circulation models (GCMs) and climate models. A plane-parallel cloud does not have any horizontal variations in its physical or optical structure and the cloud properties at a given level are assumed to be uniform throughout. This implies that solar radiation will interact within a cloud the same way at any point within the cloud. When looking at the problems between the inhomogeneous nature of clouds and the homogeneous models one can not stop at the problems with absorption. The contribution of clouds to the global radiation budget involves all aspects of the cloud optical properties, and over simplifying the structural nature of a cloud can lead to large errors. Cahalan et al. (1994a) point out that a decrease of 10% in the albedo can reduce the surface temperatures back to that of the last ice age. Cahalan goes on to observe that current climate models can cause biases of up to 10% in the albedo due to the plane-parallel cloud assumption.

An understanding of how clouds interact with the atmosphere and the environment is important when studying the global radiation budget. The manner in which a cloud is expressed optically in GCMs or climate models can greatly influence the outcome of the global radiation budget in the model. Since clouds are inhomogeneous and can be considered turbulent, they will interact with the sun's radiation in an inhomogeneous way.

Some of the studies that have been done to examine the cloud inhomogeneities are Cahalan et al. (1994a,b), Marshak et al. (1995a,b), Davis et al. (1994), and Gollmer et al. (1995). Cahalan et al. (1994a,b) developed a one dimensional cloud model from the analysis of liquid water path data collected during the First ISCCP Regional Experiment (FIRE). The cloud model was part of a Monte Carlo study to estimate the plane-parallel bias of marine stratocumulus clouds through a comparison of the independent pixel approximation and the Monte Carlo results. Marshak et al. (1995a) used the one dimensional cloud model from Cahalan et al. (1994a,b) and expanded it to a two dimensional model. Davis et al. (1994) and Marshak et al. (1995b) realized that clouds are multifractal in nature and that the cloud structure can be analyzed by looking at the different frequencies, or scales, of a cloud's spectral nature. Gollmer et al. (1995) used a new analysis method called 'Wavelet Analysis' along with Fourier analysis to find a

relationship between larger and smaller scales in clouds. This was done by using liquid water path data from FIRE, and from this data developed a one dimensional cloud model similar to Cahalan's.

The objective of the research involved in this thesis is to study both the excess absorption of solar radiation by clouds, and the inhomogeneous nature of a cloud's structure. The purpose is to present a further understanding of both concepts, and to find a possible relationship between them. A Monte Carlo routine will be used to study the absorption of solar radiation by clouds. The Monte Carlo algorithm developed by Marshak et al. (1995a) will be discussed in Chapter 2 including changes made for this study. Chapter 3 will present cloud absorption results from the Monte Carlo model both with the cloud model from Marshak et al. (1995a) and with a simplified cloud system for studying edge effects. To examine cloud structure a data set from the Atlantic Stratocumulus Experiment (ASTEX) was analyzed. The data set is a one dimensional liquid water content data set taken by a PVM-100A probe (Gerber et al., 1994). A description of the ASTEX project, the PVM-100A probe, and the data set will be discussed in Chapter 4. To analyze the nature of a cloud's structure by looking at the different scales and how the scales may relate to each other, Wavelet and Fourier analysis is used. Chapter 5 discusses the use of the newer analysis technique of wavelets. Chapter 6 will present results from the analysis of the liquid water content data set. Finally, chapter 7 will contain a summary of the cloud absorption and structure studies.

CHAPTER 2. MONTE CARLO MODEL

Due to faster and more efficient computers Monte Carlo (MC) models have gained popularity today among the many disciplines of science. Instead of using equations to study a physical behavior over a time period, the MC model uses a brute force method to simulate stochastic processes. What is meant by brute force is that the model will literally look at each individual occurrence of an event, and then keep a tabulated record of all events. The term "Monte Carlo" comes from the roulette games which use the same method generating random numbers (Binder, 1984). The method used is just to spin the "wheel" over and over again, and see how often the ball will land at each of the possible numbers.

The use of the MC model in studying radiative properties is one of the more simple methods in use today, especially for the introduction of clouds into an atmospheric system. Although the use of MC methods for use in general circulation models (GCMs) and climate models is still not yet possible due to the amount of computer time needed, they can be used to study how to optimize cloud models to be used in GCMs and climate models. The method used to study radiative properties in the atmosphere for the MC models is not unlike the random number generator of the roulette wheel. A photon is introduced into the system, atmosphere and/or cloud, then the probability of what happens to the photon within the system is based on random chance.

1. Model Description

The MC model that was used in this study is based on a model produced by Marshak et al. (1995a). The model determines a set of optical properties for an atmospheric system, and then introduces a specified number of photons. The MC uses a

two dimensional system, where the system is a simulation of the atmosphere, including clouds. The system is broken down into individual components called pixels. The optical properties produced by the original model are the reflectance and transmittance for each pixel. The reflectance and transmittance are determined by the probability of the photons ultimate destination, scattered upward or downward. While the photon is within the system the probabilities are based on the interaction of the photon with a scattering medium.

The process of the MC starts with determining a cloud for the system and the properties, both physical and optical, for each pixel within the cloud. The cloud properties start with specifying a single scatter albedo (ϖ), height and width of the cloud, and the mean optical depth (τ_o) of the whole system. Also specified is direction of solar illumination by setting a zenith angle (θ) and azimuth angle (ϕ). There is a choice of phase functions to characterize the scattering properties of the cloud. The most used phase function is the Henyey-Greenstein which is accompanied by an asymmetry parameter that can be set. Other choices for the phase function are Isotropic, Rayleigh, Haze and Cloud C.1.

One of the more complex parts of the cloud field to model is the inhomogeneous nature of the cloud field. Since the MC is looking at radiative properties, the property that is the most logical to model as inhomogeneous is the optical depth of each pixel within the system. Marshak et al. (1995) use a 2-D cascade model with random but identical distributed weights. The cascade model is based on the 1-D bounded cascaded model for stratocumulus clouds from Cahalan et al. (1994a). First consider the system as homogeneous with τ_o as the optical depth for the whole system. Next divide the system equally into four sections (Figure 2.1, as viewed from above) and then redistribute τ_o into each of the four parts as $\tau_o W_{11}$, $\tau_o W_{12}$, $\tau_o W_{13}$, $\tau_o W_{14}$, where the Ws are weights for the four sections. The Ws are randomly determined, and are distributed such that their mean will be unity (Marshak et al., 1995a). This process can go another step further so that each of the four sections are divided into four subsections, where the new optical depth in each of the four sections is redistributed as $\tau_o W_{1i} W_{2j}$ (i,j = 1,...,4). This process is then

Homogeneous
System with
optical depth = τ_o

First Cascade - Four
sections with optical
depths = $\tau_{1,1}$, $\tau_{1,2}$, $\tau_{1,3}$,
and $\tau_{1,4}$

Second Cascade - 16
sections with optical
depths = $\tau_{2,1}$,....,$\tau_{2,16}$
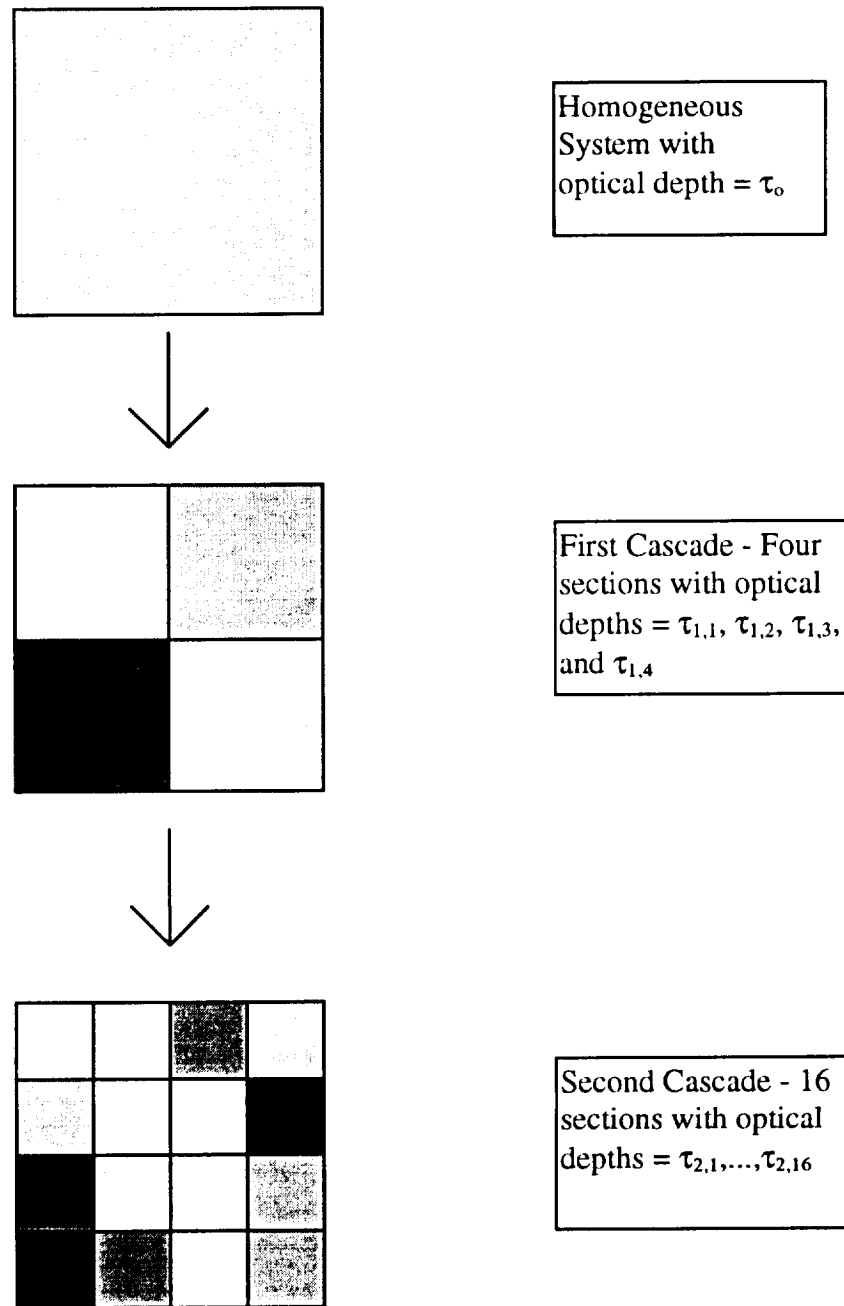
Figure 2.1 The first two steps of a 2-D bounded cascade cloud model. The top
square represents a homogeneous system before the cascade. The middle square
represents the first cascade, where $\tau_{1,i}=\tau_oW_{1,i}$ (i=1,...,4). The bottom square
represents the second cascade, where $\tau_{2,k}=\tau_oW_{1,i}W_{2,j}$ (i,j=1,...,4). All three squares
are a top view

generalized so that the system can be divided into 4^n subsystems each having an optical depth, τ_n, that was based on the optical depth, τ_{n-1}, of the higher subsystem multiplied by the weight for that subsystem. Each of the 4^n subsystems are then considered to be the individual pixels of the system. Figure 2.1 demonstrates the first two steps of the process (Marshak et al., 1995a).

After the parameters have been determined for the 2-D cloud system the simulation program begins by introducing each photon into the cloud one at a time. As the photon enters the cloud its original entry position is determined by a random number generator, and the angle at which it enters is determined by θ and ϕ. The photon then travels through the system until it encounters a scattering point. The distance it travels is called the mean free path length. The mean free path length of the photon is one of the more complicated things to simulate for an inhomogeneous system. The scheme used to simulate the photon's mean free path length by Marshak is called the maximal cross-section method, taken from Marchuk et. al. (1980). When the photon comes to a scatter point the new position of the photon is determined. If the photon is still within the cloud system it continues until it is scattered out of the cloud or is absorbed. If the new position of the photon is found to be out of the cloud it is considered to be reflected back to space, positioned over the system, or transmitted toward the ground, positioned under the system. The system is considered to be cyclic, so if a photon exits a lateral boundary, the photon is considered to have reentered the cloud from the opposite side from which it left. So if a photon is found to have been reflected, the pixel it left from is determined and the reflectance for that pixel is increased, and the same is done for the transmittance.

2. Model Changes

In order for the MC model to be used for this study there were a couple of key changes that needed to be made to the model. The first thing was to make an account for the absorption of photons in each pixel of the system. The model allows the ϖ to be set for the system allowing for absorption to take place, but made no accounting for the probability of absorption. This meant that there was no way of knowing what the

absorptance is for each of the pixels in the system. Therefore, to account for the absorption, the ϖ for the system in the model was changed so that there could be an independent $\varpi_{i,j}$ ($i,j=1,...,n$; 4^n pixels) set for each pixel. The absorption is then calculated as follows:

$$w_o = 1.0 \tag{2.1}$$

$$w_k = w_{k-1} * \varpi_{i,j} \tag{2.2}$$

$$abs_k = w_{k-1} - w_k \tag{2.3}$$

$$tabs_k = tabs_{k-1} + abs_k \tag{2.4}$$

The w's refer to the weight of the photon not to be absorbed when it reaches a scattering point. The w_o is the starting weight of the photon as it enters the system, meaning that to start with there is no probability of the photon being absorbed. The k subscript refers to each time the photon is scattered in the system. In (2.2) the weight from the previous scatter, w_{k-1} is multiplied by the ϖ_{ij} of the pixel that it is currently occupying to give the current weight, w_k, this along with (2.3) increases the probability of absorption. This is reasonable since the more times that a photon scatters in any atmospheric medium there is a greater chance for the photon to be absorbed. In (2.4) $tabs_k$ is the tabulated absorptance for the pixel. A similar technique was used by Davis et al. (1979).

Another change that was needed was to place a toggle that would turn the bounded cascade model of the cloud off so that the optical depth of each pixel could be defined independently.

CHAPTER 3. MODEL ANALYSIS

To study the radiative properties of the atmosphere with the MC model, it was run for two different cloud situations. The first used the cloud model cascade developed by Marshak et al. (1995a) over the entire system. The cascade modeled the cloud in six steps, from a plane parallel cloud to a very inhomogeneous case. The second used a simple cloud/clear system that examined the absorptance of the system by varying the cloud geometry and absorption properties. This part of the MC analysis was broken up into two studies, one for conservative droplet scattering for different vapor absorption and the other for absorption in a vapor window. The second study can loosely be considered the same as increasing liquid water in the cloud. The MC model was used also to analyze other radiative properties including the transmittance and reflectance in all situations.

1. Cloud Cascade Model

The cascade used in modeling a marine stratocumulus cloud is discussed by Marshak et al. (1995a) and explained in the previous chapter. The main focus of using the cascade was to study how the absorptance changed across the system as the cloud was modeled to be more and more inhomogeneous, along with changes made to the single scatter albedo, ϖ. The method used to analyze the absorption in the cloudy system is by cloud forcing, which looks at the cloud contribution by itself.

a. Cloud Forcing

Cloud forcing in overcast conditions is basically the difference between the clear net flux and the cloudy net flux. The following discussion comes from Harshvardhan et al. (1996), which can be referred to for a more detailed explanation. For the situation above

the cloud system, also considered as the top of the atmosphere (TOA), the cloud forcing is expressed as

$$CF^{TOA} = F_{NC}^{TOA} - F_{NL}^{TOA} \qquad (3.1)$$

The terms F_{NL}^{TOA} and F_{NC}^{TOA} are the net downward fluxes for clear sky conditions and cloudy sky conditions respectively (Harshvardhan et al., 1996). They are expressed as

$$F_{NL}^{TOA} = F_{DL}^{TOA} - F_{UL}^{TOA} \qquad (3.2)$$

$$F_{NC}^{TOA} = F_{DC}^{TOA} - F_{UC}^{TOA} \qquad (3.3)$$

where the suffixes U, D, and N represent upward, downward, and net fluxes respectively, and the suffixes L and C are the clear and cloudy indicators. The same relationship in 3.1 for cloud forcing at the top of the atmosphere can be expressed for cloud forcing at the surface, or under the cloud. The cloud forcing at the surface, CF^{SRF}, is expressed as

$$CF^{SRF} = F_{NC}^{SRF} - F_{NL}^{SRF} \qquad (3.4)$$

The equations for F_{NL}^{SRF} and F_{NC}^{SRF} will be the same as 3.2 and 3.3 but at the surface. For this study the surface albedo is considered zero and the downward flux at the top of the atmosphere is the insolation, therefore, equations 3.1 and 3.4 become

$$CF^{TOA} = - F_{UC}^{TOA} \qquad (3.5)$$

and

$$CF^{SRF} = F_{DC}^{SRF} - F_{DL}^{SRF} \qquad (3.6)$$

It also can be shown that

$$CF^{SRF} = CF^{TOA} + A_L - A_C \qquad (3.7)$$

The ratio of the cloud forcing at the surface to the cloud forcing at the top of the atmosphere, $R = CF^{SRF}/CF^{TOA}$, is one way of comparing their relative magnitudes to show excess amounts of absorption. Due to equation (3.7), if $R > 1.0$, there is an increase in absorption in the atmosphere; if $R < 1.0$, there will be a decrease in atmospheric absorption; and if $R = 1.0$, there is no change in absorption.

b. Model Setup

As was mentioned earlier, this simulation analyzes the radiative properties in a cloud system by starting out with a plane-parallel cloud, and then analyzing the change in the radiative properties with increased steps of inhomogeneity, up to six steps. To simulate an increase in the cloud inhomogeneities the number of pixels in the cloud system is increased, while leaving the cloud geometry and mean optical depth, τ_o, the same. For the plane-parallel case the whole system is considered to be one pixel, which is equivalent to a 1×1 pixel 2-D cloud system. Since each step of the cascade increases the number of pixels by a factor of four, the first increase in inhomogenizing the cloud would be a 2×2 pixel cloud, or 4 pixels. This can then be generalized to $2^n \times 2^n$ number of pixels where n = $(0,...,5)$. The number of pixels, N, used is in Table 3.1.

The other variable that was changed for each of the six increases in inhomogeneity in the cloud is ϖ. The value of ϖ starts at conservative scattering, $\varpi = 1.0$, to an extreme case where almost everything is absorbed, $\varpi = 0.8$. The values for ϖ are in Table 3.1.

Many of the variables were held constant over each of the MC runs. These variables are the mean optical depth, τ_o, the zenith angle, θ, the azimuth angle, ϕ, the width and depth of the cloud system, the number of photons, and the phase function, $P(\Theta)$ along with an asymmetry parameter, g. Each the these values are presented in Table 3.1.

$\tau_o = 10.0$	$\theta = 60°$
Width = 6.4 km	$\phi = 0°$
Depth = 0.3 km	# of Photons = 1×10^6
Henyey-Greenstein P(Θ)	
$P(\Theta) = \dfrac{(1 - g^2)}{(1 + g^2 - 2g\cos\Theta)^{3/2}}$	
$g = 0.85$	
$\varpi = (1.0, 0.995, 0.99, 0.95, 0.9, 0.8)$	
$N = (1, 4, 16, 64, 256, 1024)$	

Table 3.1 Variables and Constants used in the Monte Carlo runs.

c. Results and Analysis

The mean values of reflectance, transmittance, and absorptance for the entire system are plotted in Figure 3.1 against $\sqrt{N}$, or the number of pixels on one side. There are separate plots for four of the ϖ (1.0, 0.99, 0.95, and 0.9). The analysis of the MC results follows Harshvardhan et al. (1996).

Figure 3.1 illustrates that relating the inhomogeneity of clouds to the excess absorption can be difficult. Instead of an increase in absorption with an increase in the cloud inhomogeneity, there is a decrease. The decrease in absorptance becomes more pronounced as the system becomes more absorbing, i.e. decrease in ϖ. There is actually an increase in the transmittance for the system as it becomes more inhomogeneous, while the reflectance also decreases.

The cloud forcing ratio, R, for all the ϖ's is presented in Table 3.2. The table lists the values by R_N, where N = 1,2,....,32 is the number of pixels on one side of the system. Therefore R_1 will be the ratio for the plane-parallel case, 1×1 pixels. From these ratios it is shown that the amount of absorption in the atmosphere stays relatively unchanged as the cloud system becomes more inhomogeneous for a given ϖ. There is a small decrease in the ratios for the more absorbing cases, but it is not enough to have a significant effect. Therefore, the ratio is not affected by increases in the inhomogeneity of the cloud.
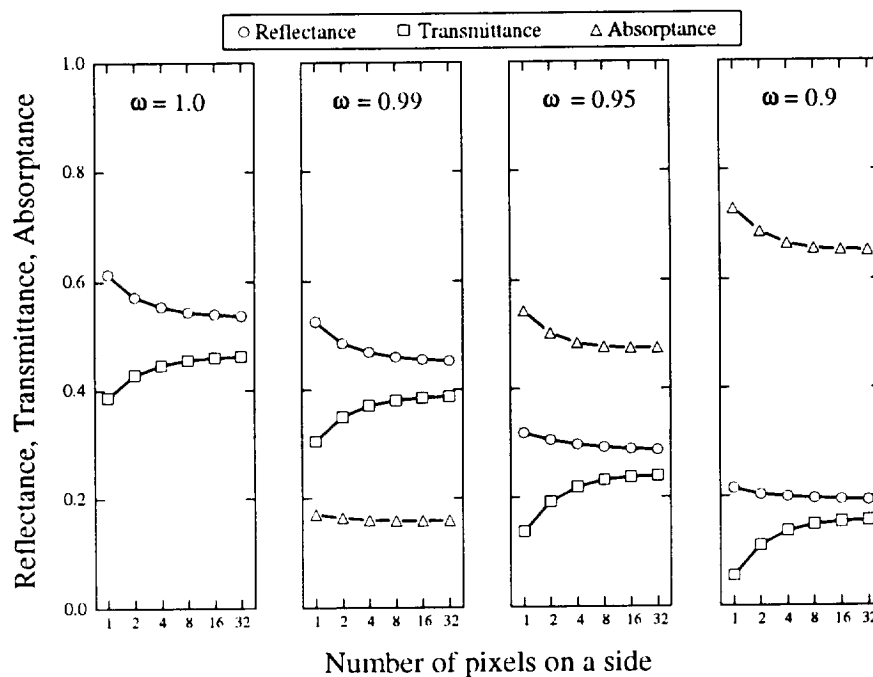
Figure 3.1 Area mean transmittance, reflectance, and absorptance for four of the single scatter albedos, ω (Harshvardhan, 1996).

ω	R_1	R_2	R_4	R_8	R_{16}	R_{32}
1.00	1.00	1.00	1.00	1.00	1.00	1.00
0.995	1.17	1.17	1.17	1.18	1.18	1.18
0.99	1.32	1.34	1.34	1.35	1.35	1.35
0.95	2.70	2.65	2.63	2.64	2.65	2.66
0.9	4.40	4.38	4.34	4.35	4.38	4.39
0.8	8.81	8.59	8.52	8.54	8.58	8.62

Table 3.2 The ratio of the cloud radiative forcing at the surface to that at the top of the atmosphere (Harshvardhan, 1996).

2. Cloud/Clear Model

The cloud/clear model is a simplified cloud model consisting of a 32×32 pixel 2-D system where it is divided into a homogeneous cloudy portion and a clear portion. Figure

3.2 illustrates a vertical profile of this system, such that the properties in both portions are the same for the direction perpendicular to the figure. Since the MC model is cyclical the cloudy portion will start again after the clear, which will be considered a new cloud.

The main focus of using this simplified model was to examine the radiative properties over the vertical profile from the cloudy to the clear portion, to examine partly cloudy effects and the effects of the sun on the cloud's edge. Similar work has been done by Hayasaka et al. (1995). The MC studies were run for different cloud geometries and single scatter albedos. The single scatter albedos were used to simulate an increase in vapor or increase in liquid, depending on the study. A comparison was also done of the actual absorptance, calculated from the MC, with an absorptance correction method discussed by Hayasaka et al. (1995) and proposed by Ackerman and Cox (1982).

a. Model Setup

Figure 3.2 is an example of the setup used for both studies of the cloud/clear MC runs. The zenith angle is set at 60°, and the azimuth angle is an arbitrary angle perpendicular to the right edge of the cloud.

The geometric values modified for the cloudy part, for which a separate MC run was executed, are the cloud fraction and the aspect ratio. The cloud fraction (N_c) is simply the percentage of cloudiness of the whole system. The aspect ratio, a, is the horizontal length, lx, of the cloud divided by the depth of the cloud, z (i.e., a = lx/z). The MC was run for seven different cloud fractions, N_c = 12.5%, 25%, 37.5%, 50%, 62.5%, 75% and 87.5%. Each of the seven N_cs were run with four different aspect ratios: 0.25, 0.5, 1.0, and 2.0. Figure 3.2 is an example of a vertical profile with N_c = 50% and a = 0.25. One thing to note is that as the cloud fraction and aspect ratio are changed the area of the cloud face that is shadowed will also change (Figure 3.3); this will be discussed later. Table 3.3 displays all of the geometric values for which the MC was run.

The first of the two studies in which the MC was run was for conservative droplet scattering for different vapor absorption, or changes in the vapor amount across the

Sun

θ

τ_1 and ϖ_1 τ_2 and ϖ_2 ...

Cloudy   Clear
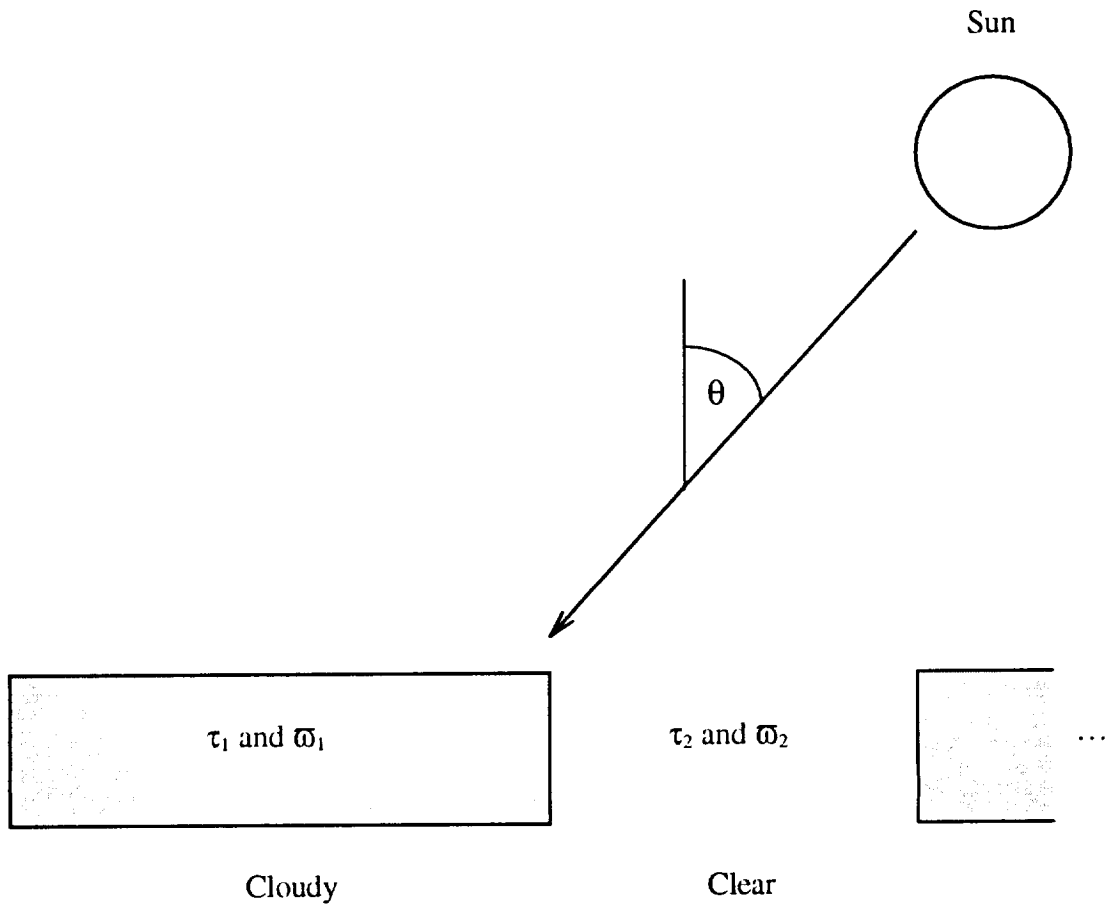
Figure 3.2 Cloud schematic for generating radiative properties. The above is set up for a cloud fraction of 50% and an aspect ratio of 0.25.
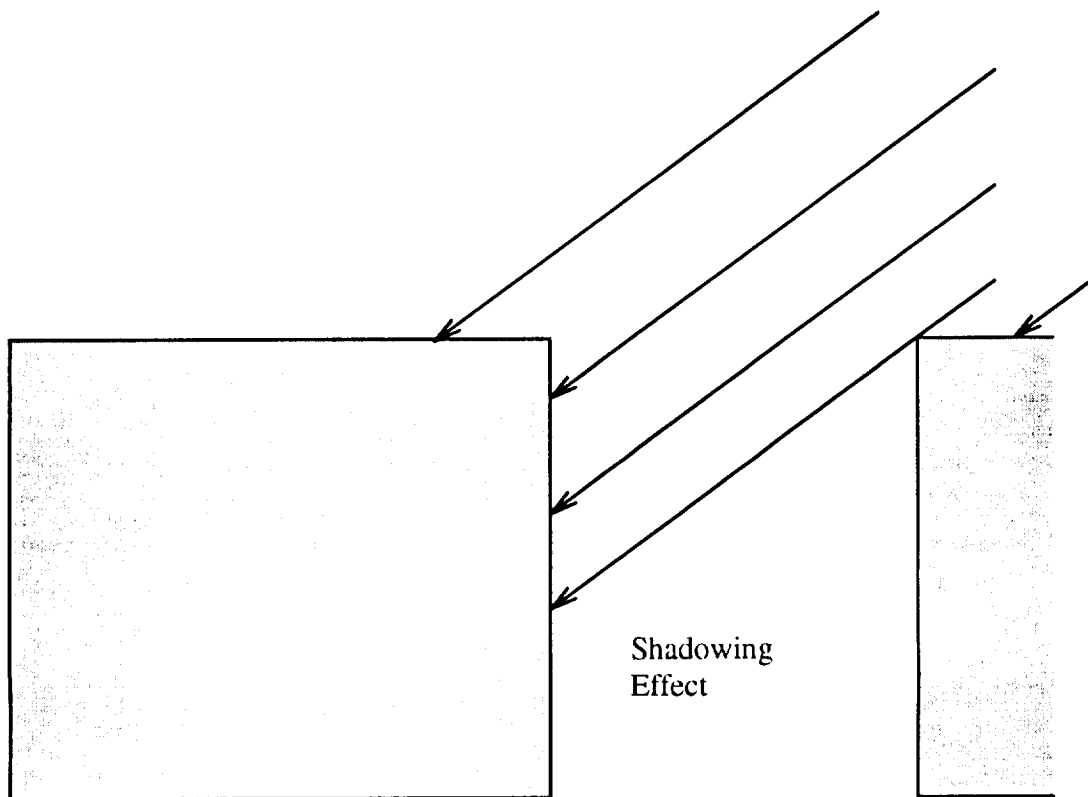
Figure 3.3 Example of the shadowing effect from one cloud onto another as the geometric properties of clouds are changed.

system. This can also be thought of as running the MC over different vapor wavelengths that absorb in the near IR. For each of the four aspect ratio cases the scattering optical depth for the cloudy portion, τ_{cs}, was set to 20.0 and the scattering optical depth in the clear portion, τ_{ls}, was set to 0.0. The clear portion is considered to only have an absorbing effect, due to the vapor. To model the effect of increasing the vapor absorption the absorption optical depth, τ_a, was increased. τ_a was first set to zero for conservative scattering and increased to 5.0 for an extreme case. Altogether, for each of the aspect ratios, the MC was run for six different values of τ_2 – 0.0, 0.1, 0.5, 1.0, 2.0, and 5.0. The total optical depth in the cloudy portion is $\tau_1 = \tau_{cs} + \tau_a$, and in the clear part is $\tau_2 = \tau_{ls} + \tau_a$ = τ_a. The single scatter albedo for the cloudy portion, ϖ_1, is determined by

$$\varpi_1 = \frac{\tau_{cs}}{\tau_{cs} + \tau_a} \tag{3.8}$$

Therefore, the ϖ_1s corresponding to the six τ_a values are 1.0, 0.995, 0.976, 0.952, 0.909, and 0.8 respectively. These different values for the single scatter albedo can be thought of as different wavelengths, where $\varpi_1 = 1.0$ would be the same as wavelengths in the visible, and the other five would correspond to wavelengths in the near IR. The single scatter albedo for the clear portion, ϖ_2, is 0.0 since only absorption takes place. Table 3.3 displays all of the τ and ϖ values in the first study.

The second study ran the MC model for zero vapor absorption at wavelengths in the vapor absorption windows, but for increasing amounts of liquid water droplets in the system. In this case since vapor absorption is zero in the clear portion, the total absorption in the clear portion will be zero. Therefore, $\tau_a = 0.0$, $\tau_1 = 20.0$, and $\tau_2 = 0.0$ for all the MC runs. To simulate the different wavelengths in a vapor window, or increasing the liquid water droplets, the single scatter albedo for the cloud, ϖ_1, was changed. The values of ϖ_1 for which the MC was run for each aspect ratio are 1.0 (conservative scattering), 0.995, 0.99, 0.95, and 0.9. As with the first study, the clear portion is considered to have only an absorbing effect, therefore, $\varpi_2 = 0.0$, but as mentioned, no

absorption will take place. Table 3.3 displays the optical values of τ and ϖ in the second study.

As with the cascade case, several of the variables in the model were held constant. They are the phase function, $P(\Theta)$, asymmetry parameter, g, number of pixels, N, the length of the system, and the number of photons. These are listed in Table 3.3.

Study 1	Study 2
1) $\tau_1 = 20.0$, $\tau_2 = 0.0$, $\varpi_1 = 1.0$	1) $\varpi_1 = 1.0$
2) $\tau_1 = 20.1$, $\tau_2 = 0.1$, $\varpi_1 = 0.995$	2) $\varpi_1 = 0.995$
3) $\tau_1 = 20.5$, $\tau_2 = 0.5$, $\varpi_1 = 0.976$	3) $\varpi_1 = 0.99$
4) $\tau_1 = 21.0$, $\tau_2 = 1.0$, $\varpi_1 = 0.952$	4) $\varpi_1 = 0.95$
5) $\tau_1 = 22.0$, $\tau_2 = 2.0$, $\varpi_1 = 0.909$	5) $\varpi_1 = 0.9$
6) $\tau_1 = 25.0$, $\tau_2 = 5.0$, $\varpi_1 = 0.8$	$\varpi_2 = 0.0$, $\tau_1 = 20.0$, $\tau_2 = 0.0$
$\varpi_2 = 0.0$	

$N_C = (12.5\%, 25\%, 37.5\%, 50\%, 62.5\%, 75\%, 87.5\%)$

$a = (0.25, 0.5, 1.0, 2.0)$

Henyey-Greenstein $P(\Theta)$

$$P(\Theta) = \frac{(1 - g^2)}{(1 + g^2 - 2g\cos\Theta)^{3/2}}$$

$g = 0.843$

Width = Length = 8.0 km

$\theta = 60°$

N = 1024 (32x32)

# of Photons = 1×10^7

Table 3.3 Variables and Constants used in both MC studies

Figure 3.4 from Espinoza and Harshvardhan (1996) illustrates the two studies by looking at the spectral distribution of water vapor absorption. The outer plot represents the incoming radiation at the top of the atmosphere, the dotted line is the total absorption

of the clear sky in the near IR, and the two solid lines represent the absorption of a semi-infinite cloud with droplets of size 8 and 20 μm. The first study is illustrated by the areas of clear sky vapor absorption, represented by the dotted line. That is the model is looking at wavelengths where vapor absorption is important for both the clear, dotted line, and the cloudy portions, solid lines. The second study is illustrated by the dips in the dotted line where vapor does not absorb, also called vapor windows. This is where absorption by liquid droplets of the cloud becomes important and is shown by the cloud absorption lines. These lines show that there is absorption due to the liquid at wavelengths in the vapor window.
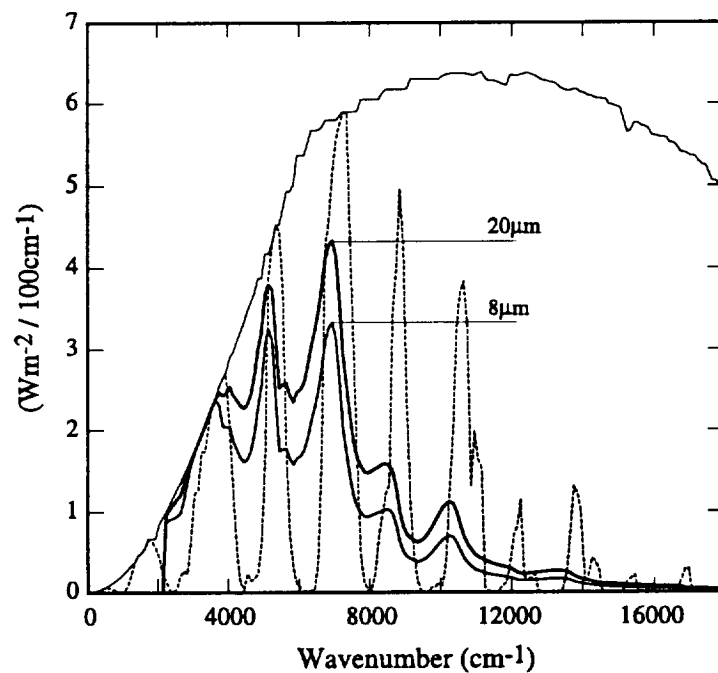
Figure 3.4 Spectral characteristics of water vapor and liquid water absorption in the near IR (Espinoza and Harshvardhan, 1996).

The optical depths discussed so far for the cloud are for the vertical direction, but not for the horizontal. The horizontal optical depth, τ_h, of the cloud, like the horizontal

distance of the cloud, is linked to the aspect ratio. The total τ_h across the cloud can be expressed as

$$\tau_h = \tau_v/a \qquad\qquad (3.9)$$

where τ_v is the vertical optical depth of the cloud. This means that the horizontal optical depth of each cloud pixel for a vertical profile, τ_i ($i = 1,...,n$; $n = $ # of pixels), is also different from τ_v. Each τ_i can be found by dividing τ_h by the total number of pixels, expressed as

$$\tau_i = \tau_v/(a \bullet P) \qquad\qquad (3.10)$$

where P is the number of horizontal pixels in the vertical profile. For example let $N_C = 50\%$, $a = 0.25$, and $\tau_v = 20.0$. The number of horizontal cloud pixels in the vertical profile will be 16 (32 × N_C). the resulting optical depths come out to be $\tau_h = 80.0$ and $\tau_i = 5.0$.

b. Results

The results for the first study are shown in Figures 3.5 - 3.16 and for the second study in Figures 3.17 to 3.28. Results are only shown for $N_C = 12.5\%$, 50% and 87.5% for all aspect ratios. The values that are plotted are the reflectance, transmittance, and absorptance from the MC (actual) and the absorptance calculated using the correction method from Ackerman and Cox (1982) (corrected). The plots are a vertical profile of the cloud/clear system where the one dimensional pixel unit is the corresponding pixel on that side. To show the cyclical, or periodic, effect due to the wrap-around of the photons in the MC, half of the system is repeated. The values of each of the radiative properties are an average of the 32 pixels in the direction perpendicular to the vertical cross section given in Figure 3.2.

c. Observations

From comparing the output of both studies a major difference shows up in the results for transmittance and the MC absorptance, or actual absorptance. It should be noted that since the scattering properties for a given single scatter albedo does not change for the cloud in both studies there is little or no difference in reflection. An example of the difference is seen by comparing Figures 3.5b and 3.17b, and Figures 3.5c and 3.17c. The difference in the absorptances is obvious from the initial conditions set for both studies. The first study examined the increase in vapor absorption by decreasing the single scatter albedo across the system which includes the clear portion. Therefore, as the ability of the vapor to absorb increases, the absorptance will increase. The decrease in absorption for a particular single scatter albedo in the cloud is due to scattering and reflectance by cloud droplets taking prominence over the absorptance and transmittance. Since the clear portion has very little scattering taking place when the ability of the vapor to absorb is low, the transmittance will be high.

On the other hand the second study focuses on wavelengths that fall in the vapor absorption window, or increasing the absorption due to the liquid droplets. Again it is obvious that there is no absorption taking place in the clear portion since vapor absorption is neglected. Therefore, just about any photon that enters the clear portion will be transmitted giving the transmittance a value close to 1.0.

The above observations become distorted as the clouds become large enough so that the shadowing has some effect. There is little or no difference in the transmittances for $N_C = 87.5\%$ (Figures 3.14b - 3.16b compared with Figures 3.25b - 3.28b). In this case the clear portion is small enough that it is almost completely shadowed. The photons have a much greater probability of being scattered which increases the probability for reflectance. Also since the mean free path length of the photon increases there is a greater potential for absorption in the first study.

Another observation that must be made is the effect on the edge of the cloud facing the sun, or edge effect. Since a greater area of the cloud is exposed to the photons there is an increase in the activity at the edge of the cloud and the portion of the cloud

near the edge. The increase in activity is most prominent for smaller aspect ratios; this can be seen in Figures 3.5, 3.9, 3.13 and 3.17, 3.21, and 3.25 where there is a peak in the reflectance, transmittance and absorptance at or near the cloud edge. As the clouds become taller the shadowing of one cloud onto another starts to reduce the area with direct contact to the photons, reducing the peaks.

d. Analysis

Since one of the main focuses of this study is to examine the absorption of solar radiation in clouds, a look at how absorption is retrieved is needed. When a photon enters a cloud only three things can happen to it: it can be reflected back to space, transmitted to the surface, or absorbed by the cloud. Therefore, the combined probability of all three events happening is

$$R + A + T = 1.0 \qquad (3.11)$$

where R is reflectance, A is absorptance and T is transmittance. The absorptance A is then given by rearranging (3.11); i.e., $A = 1 - R - T$; this is called the apparent absorptance. This calculation of absorptance will not always be correct for non plane-parallel cloud systems. The calculated absorptance can actually go negative; which is not correct since the absorptance must be between zero and one. Figures 3.29 and 3.30 are examples of the apparent absorptance in the cloud/clear system for both studies with geometric values of $N_C = 50\%$ and $a = 0.25$. The absorptance in both studies can have negative or low values in part of the clear region closest to the cloud. It would appear, at first, that the transmittance has been overestimated in the clear portions (Figures 3.9b and 3.21b). This increase is not an over estimate, but is due to an increase in photons being transmitted into those pixels, from the photons leaking in from the cloud's edge.

A correction method for dealing with this problem in the near IR absorption was discussed by Hayasaka et al. (1995) and originally introduced by Ackerman and Cox (1982). The corrected absorptance in the near IR region is found by subtracting the

apparent absorptance of the visible from the apparent absorptance of the near IR. This can be expressed as

$$A_{NIR} = (1 - R - T)_{NIR} - (1 - R - T)_{VIS} \qquad (3.12)$$

According to Hayasaka et al. (1995) there are two assumptions that have to be made. The first is that absorption by liquid water and vapor in the visible region is negligible. The second assumption is that the scattering radiative properties for the IR region are the same as in the visible region. The result of the corrected absorptance for both studies is shown in Figures 3.5d through 3.28d.

Figures 3.31 to 3.44 are plots of the difference between the actual, or MC, absorptance and the corrected absorptance from Ackerman and Cox for all geometric values. The first vertical line indicates the first cloud edge and the beginning of the clear portion, and the second vertical line indicates the start of the second cloud. The difference plots show that the correction method works well in some places but not in others. One instance that the correction method works well is for cases where the absorption is small. This can be observed in all of the plots where the single scatter albedo approaches conservative scattering the difference becomes small. This is realistic since both of the apparent absorptances become small as the probability of absorption decreases resulting in smaller differences. Another instance where the correction method does better is within the cloud as the cloud fraction increases beyond 50%. As the cloud fraction approaches 100% the cloud becomes closer to a plane-parallel cloud where the optical properties are homogeneous. This adheres to the second assumption made be Hayasaka et al. (1995) where scattering for the visible and near IR is uniform. Therefore, the reflectance, transmittance, and absorptance in the cloud will behave more like equation 3.11 resulting in the corrected and actual absorptances being similar. This does not work for the cases involved in the second study. In Figures 3.38 through 3.44 as the cloud becomes bigger, by increases in N_c and aspect ratio, and the shadowing of the second cloud becomes larger the more the correction method overestimates the absorption. As the clear portion is

shadowed there are fewer directly transmitted photons. The correction method mistakes the clear portion as having absorption even though it was initially specified to have no absorption. The correction method does well also for smaller cloud fractions and aspect ratios (Figures 3.31a and 3.38a). In the smaller sized clouds the photons scattering outside the cloud will interfere with a smaller region of the clear portion. The part of the clear portion that remains unaffected will experience the same homogeneity of optical properties as does a plane-parallel cloud.

The correction method is far from being flawless, especially at the cloud edge exposed to the sun. It has many problems for cloud fields where the cloud fraction is neither small nor large, with small aspect ratio. A good example of this is in Figure 3.34a and b. The correction method is underestimating the absorption in the clear portion while at the same time it is overestimating the absorption in the cloudy portion. In both cases since the aspect ratio is small the second cloud will not be tall enough to shadow the first cloud. When a photon leaves the side of the cloud the correction method erroneously assumes that the photon will be scattered and not absorbed due to the second assumption. Another problem with the second assumption is that it assumes that scattering and absorption are uniform throughout the cloud. This is not true, most of the scattering and absorption of photons takes place in the upper portion of a cloud with fewer and fewer photons making it to the lower parts of the cloud.

It also must be noted that there may be limits to the MC model. Figures 3.38c and d, and 3.39c and d show that the MC is causing a large overestimate of the absorption at the cloud edge. An increase in the absorption is reasonable due to the excess illumination of the cloud's edge, but it is unlikely that it would experience such a large increase.

Another problem deals with calculating absorption for either a specific spectral region or over the broad band. Hayasaka et al. (1995) used the correction method over the broad band of both the visible and the near IR regions in their MC study. From their findings it could be concluded that the correction method works well over the broad band. The problem comes in with a specific spectral region. The findings in this study focused in

on spectral regions and found that the correction method could overestimate or underestimate the absorption at higher absorbing wavelengths.

A conclusion that can be made from these comparisons is that the correction method works well with a cloud field where the cloud is closer to being plane-parallel and covers a large area. A cloud field, such as stratocumulus clouds, where there is little variation in radiative properties and there is little difference in geometry would be a good example where the correction method would work. On the other hand as the cloud field becomes more random such that the geometric and radiative values change more rapidly, or for a cloud field with broken cloud cover, the correction method would not give good results.

Figures 3.45 and 3.46 are plots of the mean system absorptance and reflectance for the first study vs. the cloud fraction, and Figures 3.47 and 3.48 are plots of the mean system absorptance and reflectance for the second study. Each of the graphs plot the four aspect ratios, and each graph represents a different cloud single scatter albedo.

The first study is the same as looking at wavelengths where cloud droplets are conservative scatterers and the vapor is doing the absorbing. In the clear portion the photons are either transmitted or absorbed by the vapor - none are reflected back to space. There is an apparent reflection of photons when N_C increases to a point where scattered photons from the cloud enter the clear portion as they escape back to space. Extending the cloud by increasing N_C is the same effect as increasing the scattering cloud droplets in the clear portion. This increase in cloud droplets increases scattering which then increases the path length of the photon. As the path length increases the probability of absorption by vapor will increase, but since the cloud droplets being conservative scatterers there will be no droplet absorption. However, some of the photons will be reflected. In this case the increase in reflection dominates. Therefore, as N_C increases, there is an increase in the amount of reflectance of the system, (Figure 3.46), and a decrease in the absorption across the system (Figure 3.45).

The second study looks at the other side where the wavelengths are strong for absorbing cloud droplets but weak for vapor. Here absorption is absent in the clear portion from the assumption that vapor is not absorbing causing the photons to be directly transmitted (Figures 3.17b to 3.28b). As N_C increases, the amount of absorbing droplets increases in the system, which has the opposite effect of the first study on the absorption across the system in that absorption increases (Figure 3.47).

The difference in the behavior of the absorption between the two studies sets up a tradeoff between wavelengths that absorb for vapor, and wavelengths that absorb for liquid water. The tradeoff of absorption gives an indication that the excess absorption observed in clouds may occur in certain spectral regions. This was pointed out by Harshvardhan et al. (1996).

The radiative properties in the shadowed part of the clear area between clouds has been mentioned above to behave like a cloud. This can change the actual cloud fraction to an apparent, or effective cloud fraction, N_e. The effective cloud fraction is the fraction of the system whose radiative properties behave like a plane-parallel cloud at a normal cloud fraction, N_C, which may be different from N_e. One way to compare N_C with N_e is by the ratio of N_e to N_C (N_e/N_C). If the ratio is unity then there is no difference between both cloud fractions, but if $N_e/N_C > 1.0$ (or < 1.0) the cloud will appear to be larger (smaller) for the radiative properties. As N_C approaches 100% N_e and N_C come closer to being the same.

The concern is that N_e has always been calculated with respect to reflectance, since it is an easier variable to use, and not absorptance. Through the MC studies N_e can be estimated for the simplified clouds, from Figures 3.45 through 3.48, by absorptance, the same way it is estimated from reflectance (Harshvardhan and Thomas, 1984). Since each increase in the cloud fraction forces the cloud into a non-reflecting clear portion it is more a calculation of cloud forcing than of absorptance. If the ratio is unity the trend of absorptance vs. increasing cloud fraction would be linear, this is the behavior in the first study for the more absorbing cases (Figures 3.45c and d). This same behavior can also be seen in the reflectance (Figures 3.46c and d) from the first study. So in this case the

absorptance and reflectance agree on a ratio of unity, or $N_e \approx N_C$, at least for higher absorbing wavelengths. For the less absorbing cases in the first study N_e is harder to determine with the absorptance, since the trend is more horizontal, and must be done with the reflectance.

Since the second study displays a completely different set of results the ratio, N_e/N_C, will be different from the first study. The reason for this is that there is more absorption taking place in the cloud than in the first study. In this study as the cloud becomes more absorbing there is more of a difference between the results of the aspect ratio. For smaller aspect ratios the trend is linear, a = 0.25 in Figure 3.47, but as the cloud increases the trend becomes convex. The more the trend is convex the higher the cloud fraction ratio will be, for example a = 2.0 in Figure 3.47. As N_C increases it reaches a point where the absorptance becomes saturated, reaching the plane-parallel absorptances, as shown in Figure 3.47c and d for N_C greater than 60%. The majority of the activity of the photons is in the top part of the cloud. If the aspect ratio were to be developed for just the part of the cloud's depth that the photons interact it would be different from the geometrical aspect ratio, called the photon aspect ratio, a_p. As the cloud increases in geometry the a_p decreases to where the part of the cloud that the photons are absorbed is similar to a plane-parallel cloud causing saturation in the absorption.

The absorptance results for N_e is contradictory to the results from the reflectance in the second study. As the absorptance increases the trend of the reflectance becomes more linear pointing to a ratio closer to 1.0 which is less than the ratio determined from the absorptance trends. Future work dealing with N_e should take into account the fact that N_e found from the reflectance may not always be the same as the absorptance.

As has been pointed out earlier, the edge of the cloud can easily be detected in both studies. The first place this is evident is in the reflectance and transmittance plots, Figures 3.5-3.28a and b. More important is the reflectance since the reflected photons are what a satellite will see in the near IR. Since the sun is shining from the right side of the cloud/clear system the right side of the cloud, and the first few pixels within the cloud, will

receive a large portion of the photons. The pixels on the cloud's edge or close to the edge will experience an increase in the amount of scattering events, therefore, increasing the probability of both reflection and transmission to take place. This can easily be seen in Figure 3.9a and b. There is a definite maximum in the amount of transmittance right at the edge, and a reflectance maximum occurring a few pixels into the cloud. The reason for the reflectance dropping off at the edge is that with an increase in interaction at the cloud's edge also brings an increase in the amount of absorption. Figure 3.9c shows a maximum in the absorptance at the cloud's edge.

There are two effects that will make it harder to detect the edge with the reflectance; one is geometric the other is radiative. The geometric effect is the aspect ratio: as the aspect ratio increases, the cloud's edge becomes harder to see. As the cloud becomes taller the cloud to its left, due to the cyclical nature of the MC, will start to shadow the first cloud (Figure 3.3). This will decrease the intensity of the activity in the side of the cloud and shift the reflectance maximum toward the center of the cloud (Figure 3.12a). The radiative effect is the increase in the amount of absorption allowed to take place in the cloud, i.e., changes in ϖ_l. In both studies as the absorption is increased the magnitude of the maximum at the edge decreases. See Figure 3.9a again, the magnitude of the maximum is quite different for conservative scattering, $\varpi_l = 1.0$, and $\varpi_l = 0.909$, and disappears for the extreme case of $\varpi_l = 0.8$.

The reason for looking at the edge effects due to reflectance is to explore the feasibility of future studies into the problem of retrieving the optical depth at a cloud's edge from satellite. Most of the optical depth retrieval routines calculate the optical depth at the edge the same way as the rest of the cloud. As can be observed from the reflectance plots there exists a maximum at the edge for clouds with smaller aspect ratios. The satellite only sees an increase in the reflected solar radiation and may be perceived by the retrieval as an increase in the optical depth. A possible correction for this is to apply a ratio of the reflectance, or radiance, at a more absorbing wavelength to that of a visible wavelength where $\varpi_l = 1.0$. The reason for this is due to the change in magnitude of the spike, or maximum at the edge as can be observed from the MC reflectance output from

both studies. Due to the problem of losing the maximum with higher aspect ratios this correction may not be used on taller type clouds. It, though, could be very useful for stratocumulus and stratus type clouds, which have much smaller aspect ratios. This is currently being studied by Davis et al. (1994) and Marshak et al. (1995b) among others.
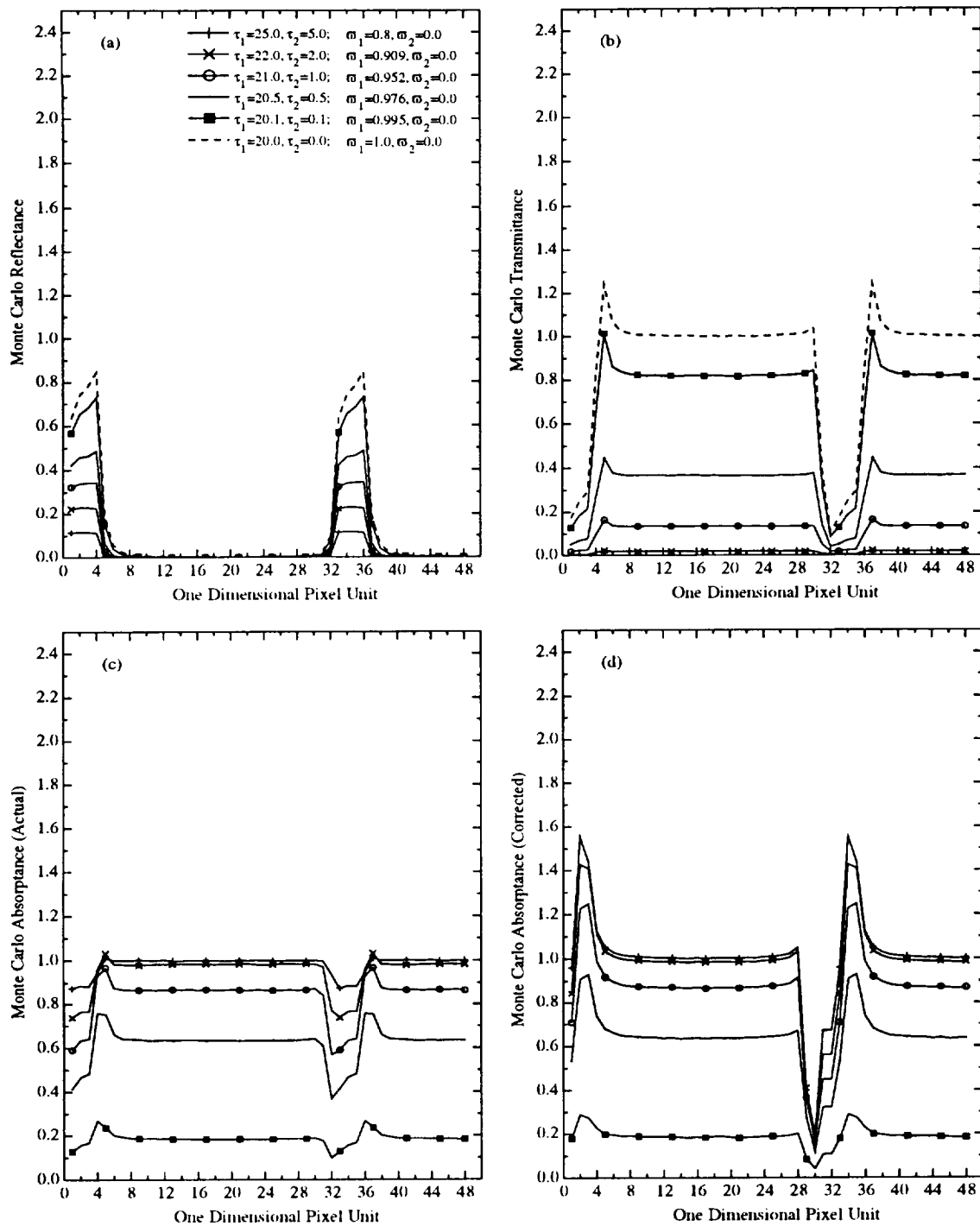
Figure 3.5 Monte Carlo (a) reflectance, (b) transmittance, (c) absorptance, and (d) corrected absorptance for the first study with a cloud fraction of 12.5% and aspect ratio of 0.25.
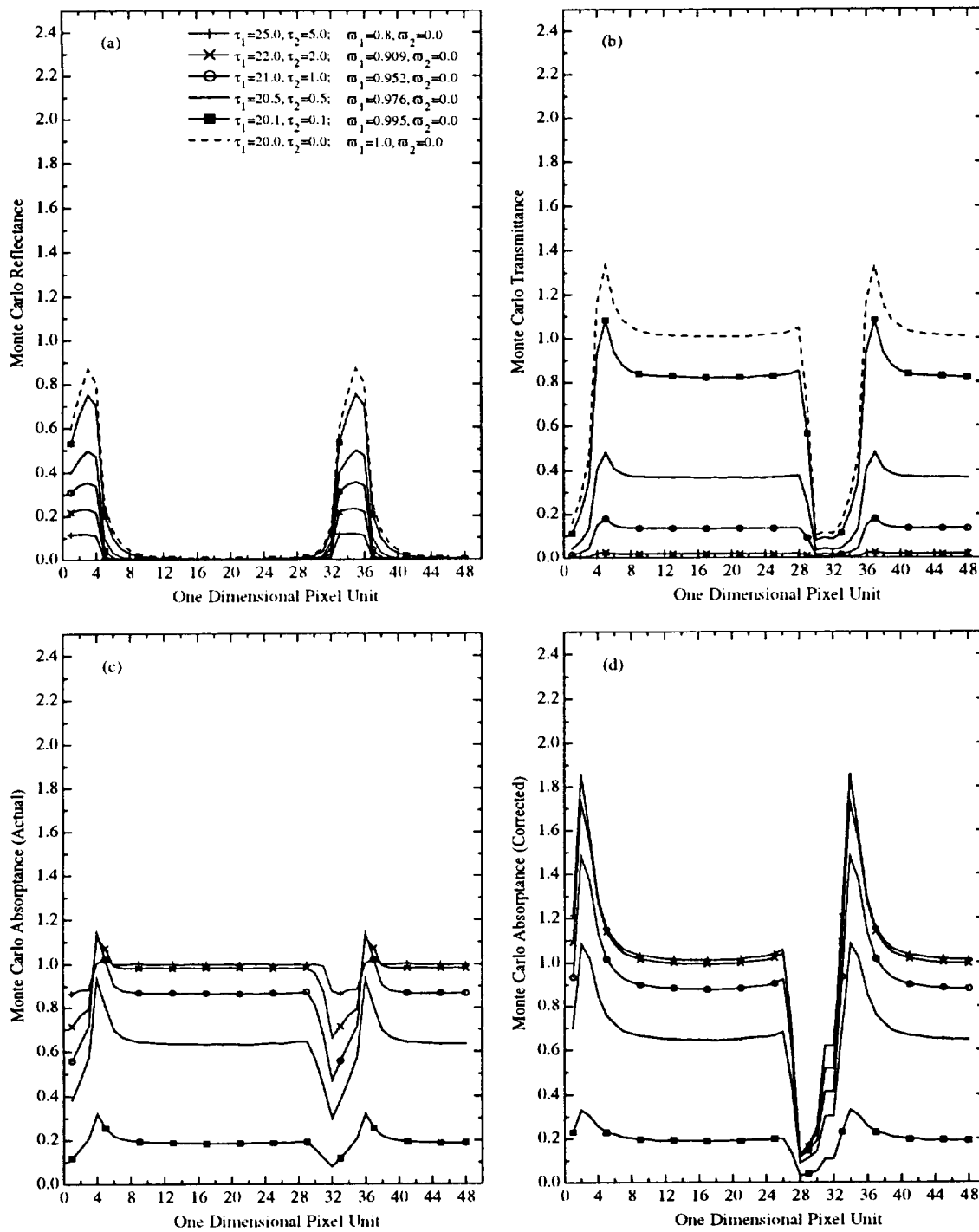
Figure 3.6 Same as Figure 3.5 except for a cloud fraction of 12.5% and aspect ratio of 0.5.
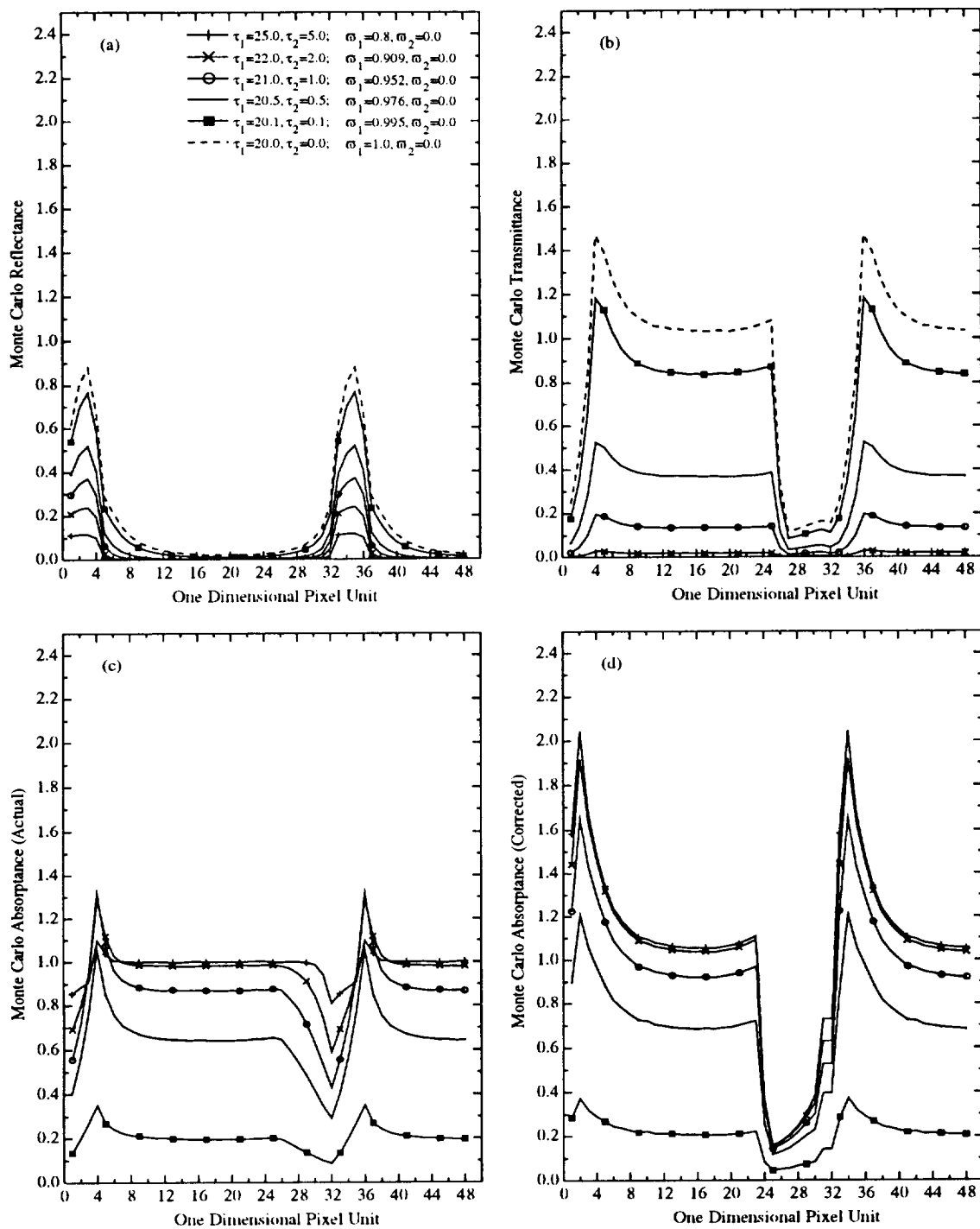
Figure 3.7 Same as Figure 3.5 except for a cloud fraction of 12.5% and aspect ratio of 1.0.
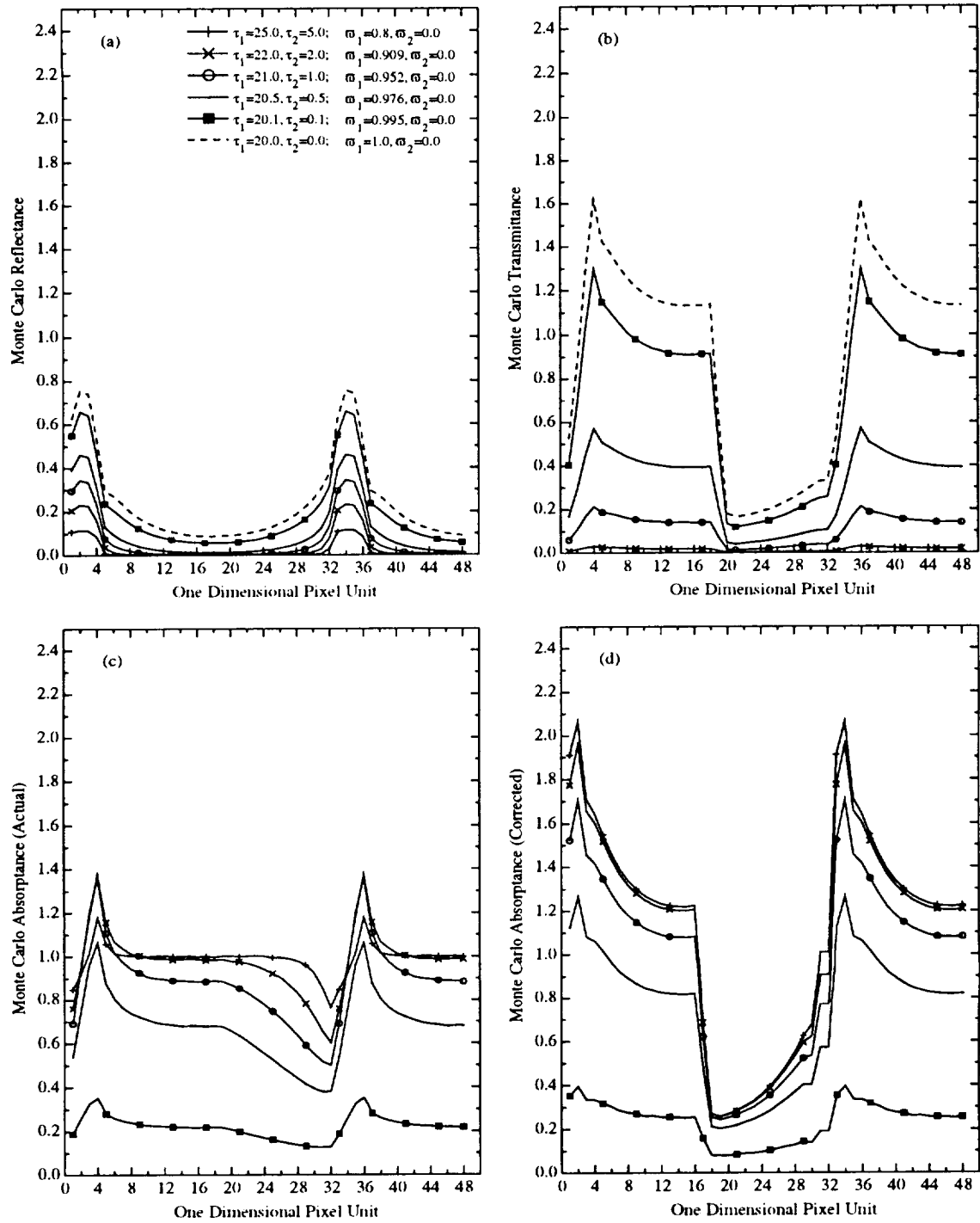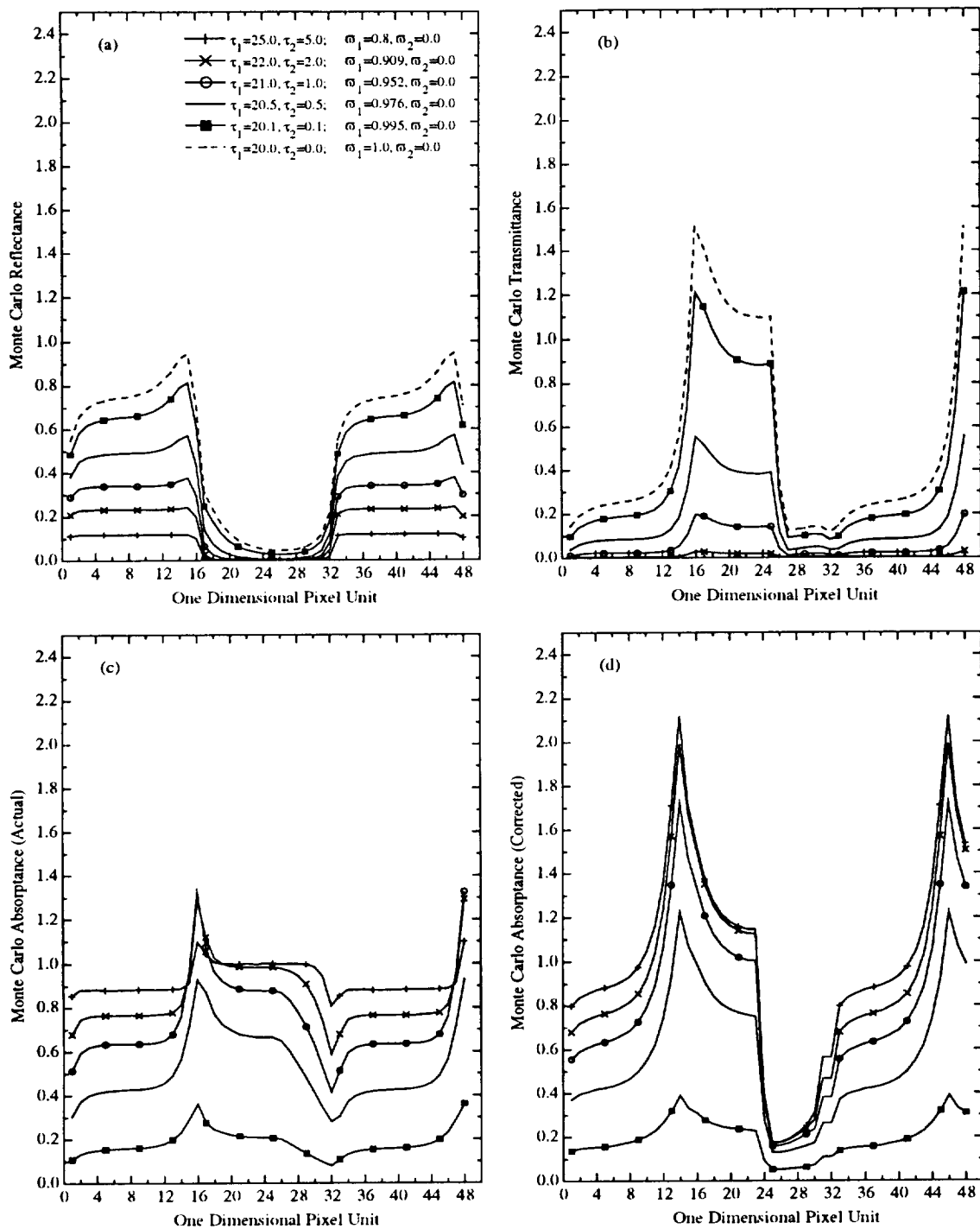
Figure 3.8   Same as Figure 3.5 except for a cloud fraction of 12.5% and aspect ratio of 2.0.

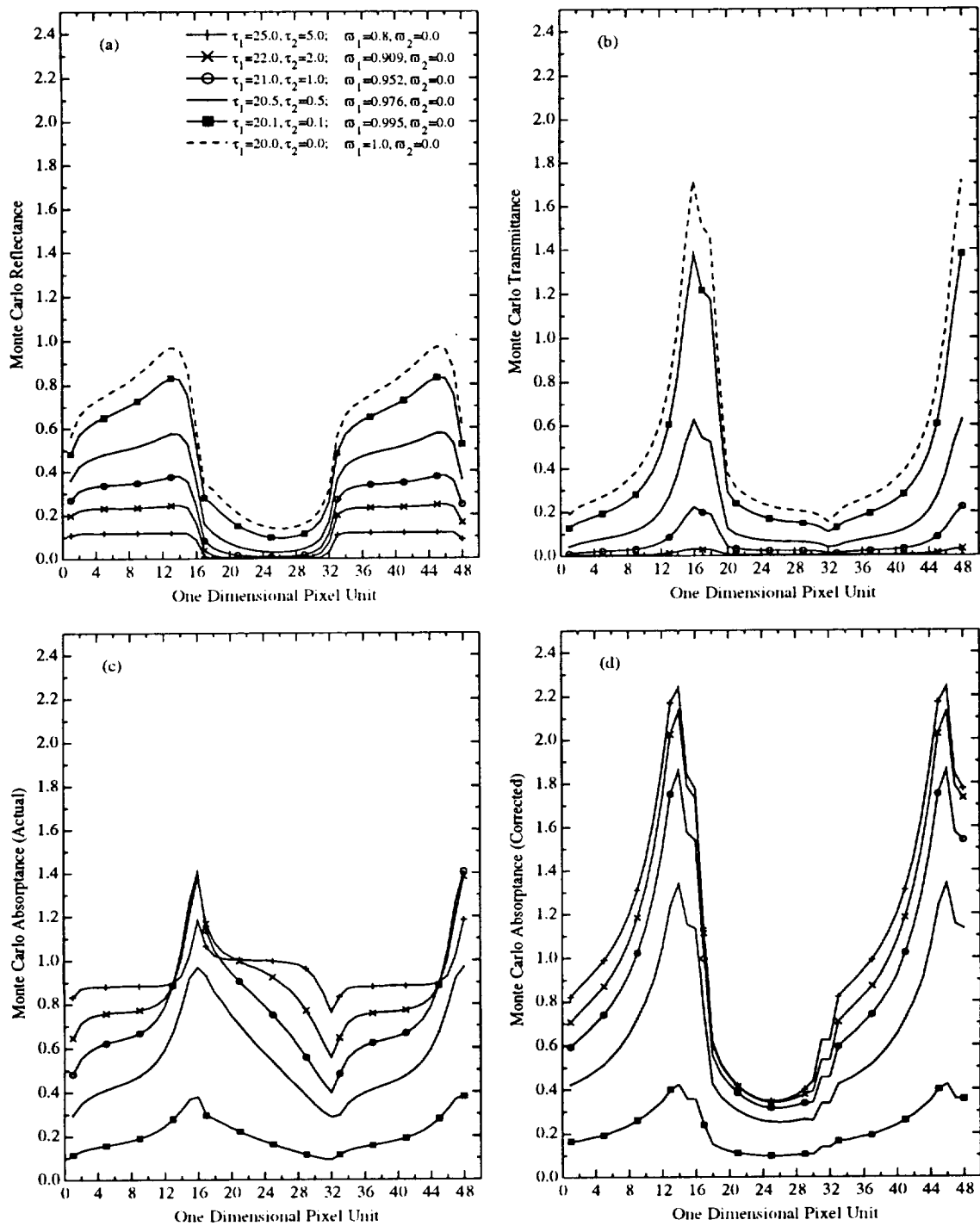Figure 3.9 Same as Figure 3.5 except for a cloud fraction of 50% and aspect ratio of 0.25.

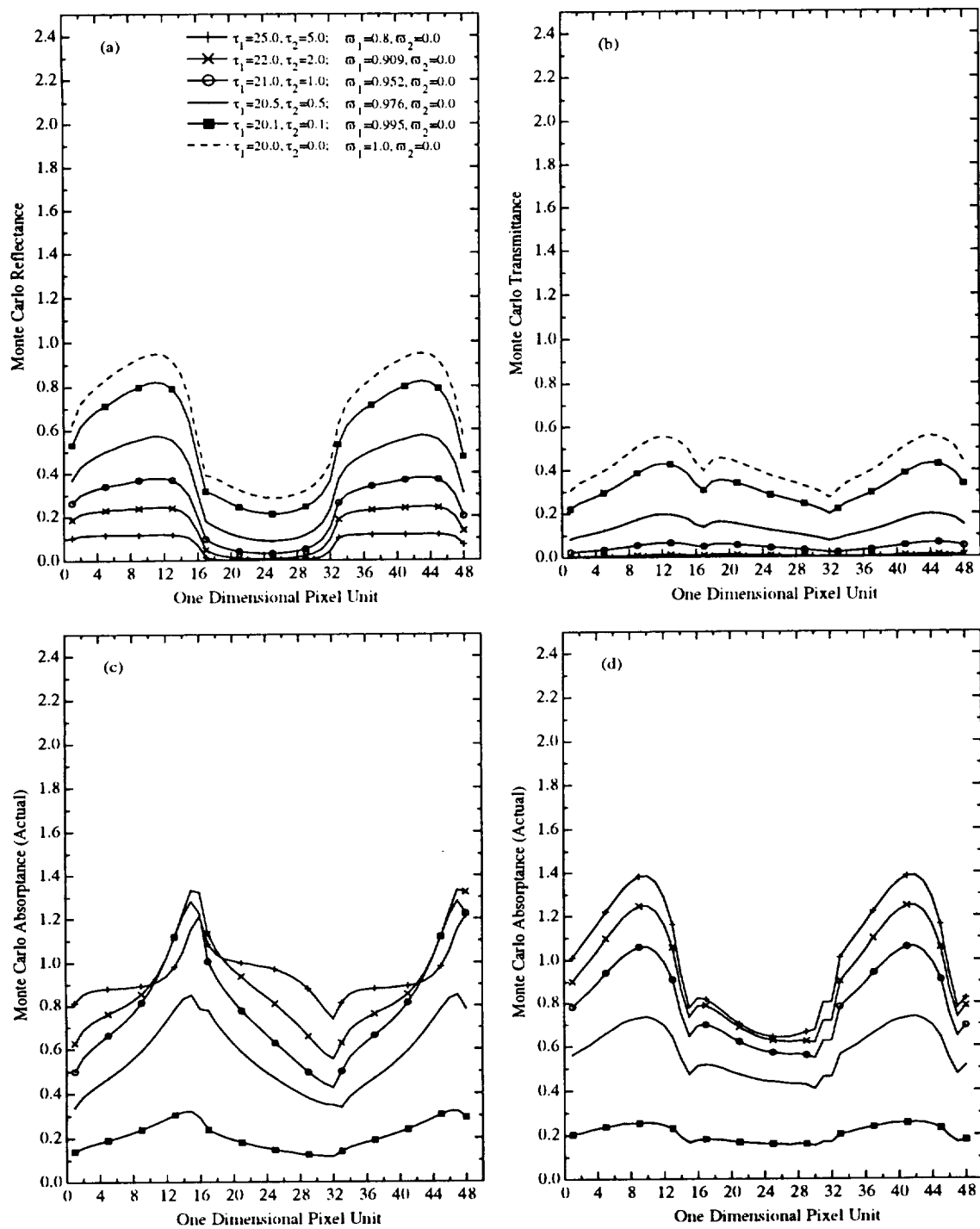Figure 3.10 Same as Figure 3.5 except for a cloud fraction of 50% and aspect ratio of 0.5.

Figure 3.11   Same as Figure 3.5 except for a cloud fraction of 50% and aspect ratio of 1.0.
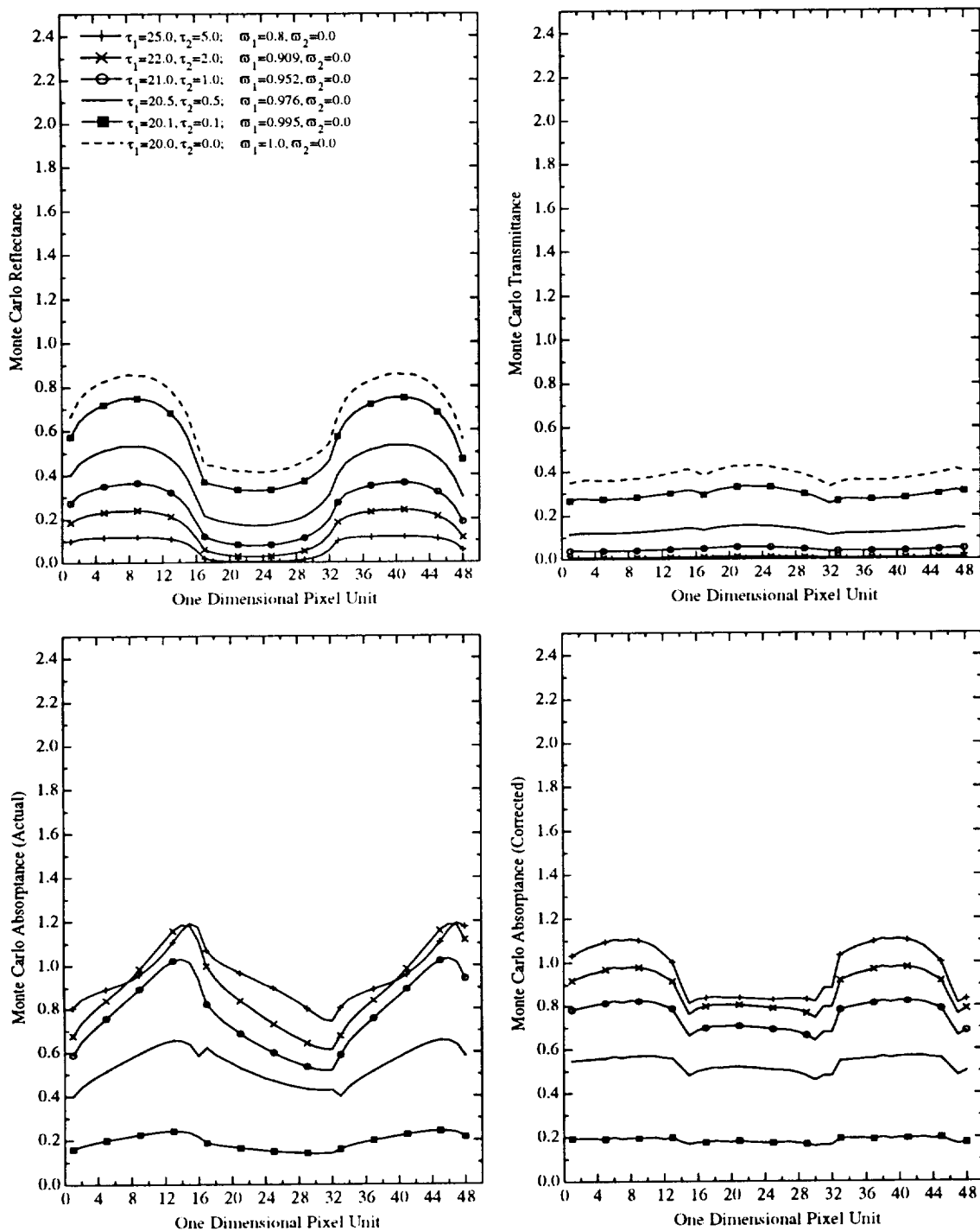
Figure 3.12 Same as Figure 3.5 except for a cloud fraction of 50% and aspect ratio of 2.0.
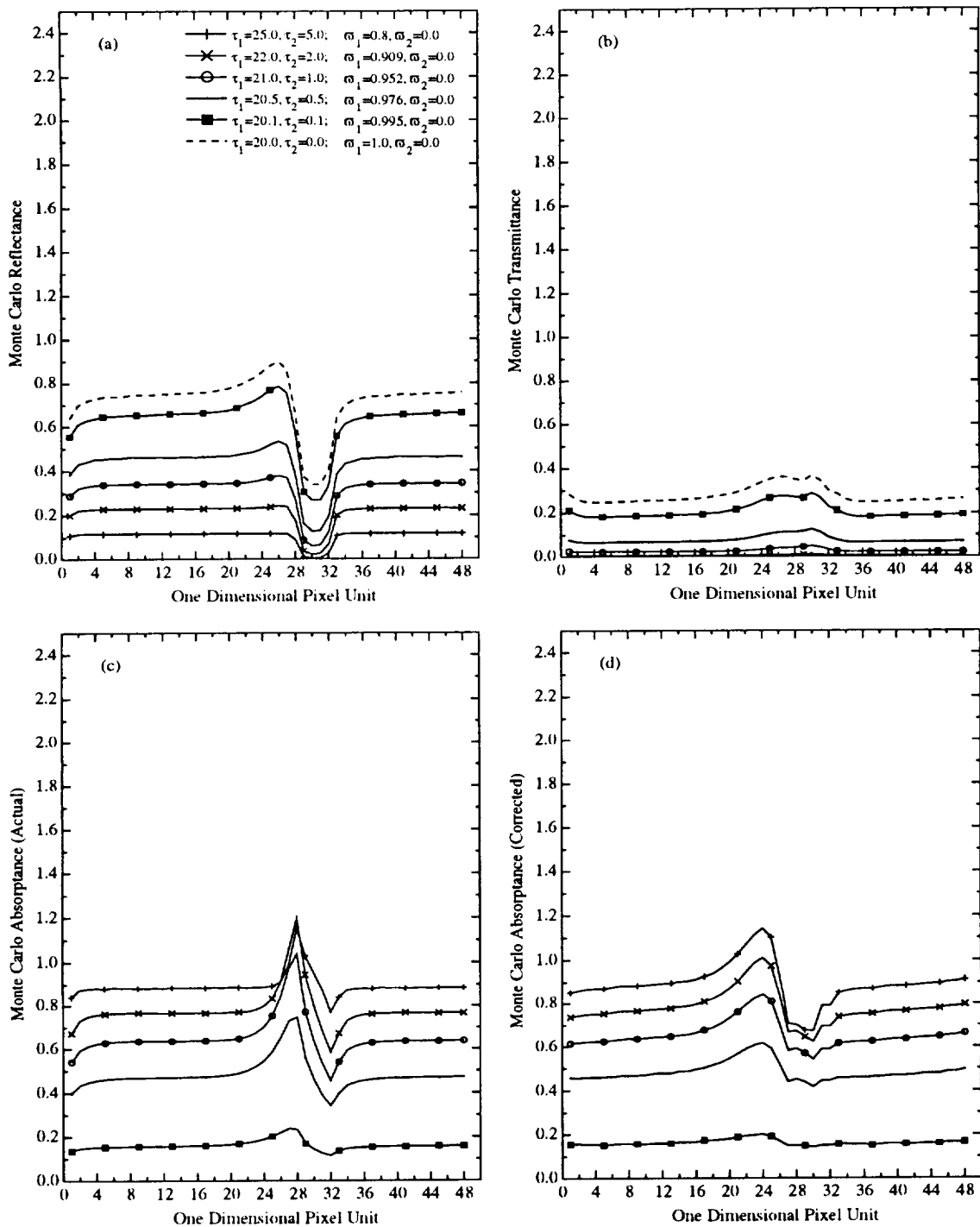
Figure 3.13 Same as Figure 3.5 except for a cloud fraction of 87.5% and aspect ratio of 0.25.
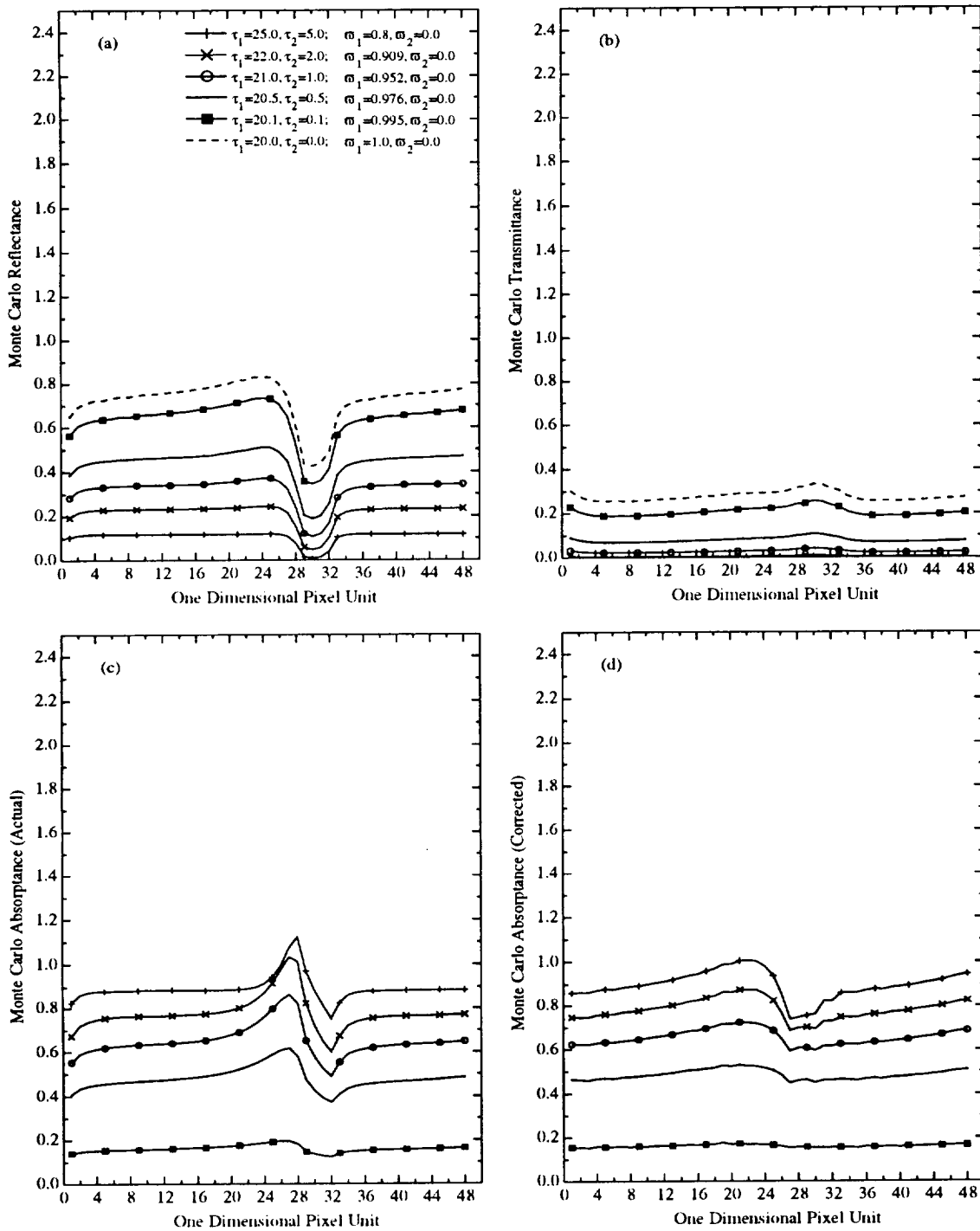
Figure 3.14 Same as Figure 3.5 except for a cloud fraction of 87.5% and aspect ratio of 0.5.
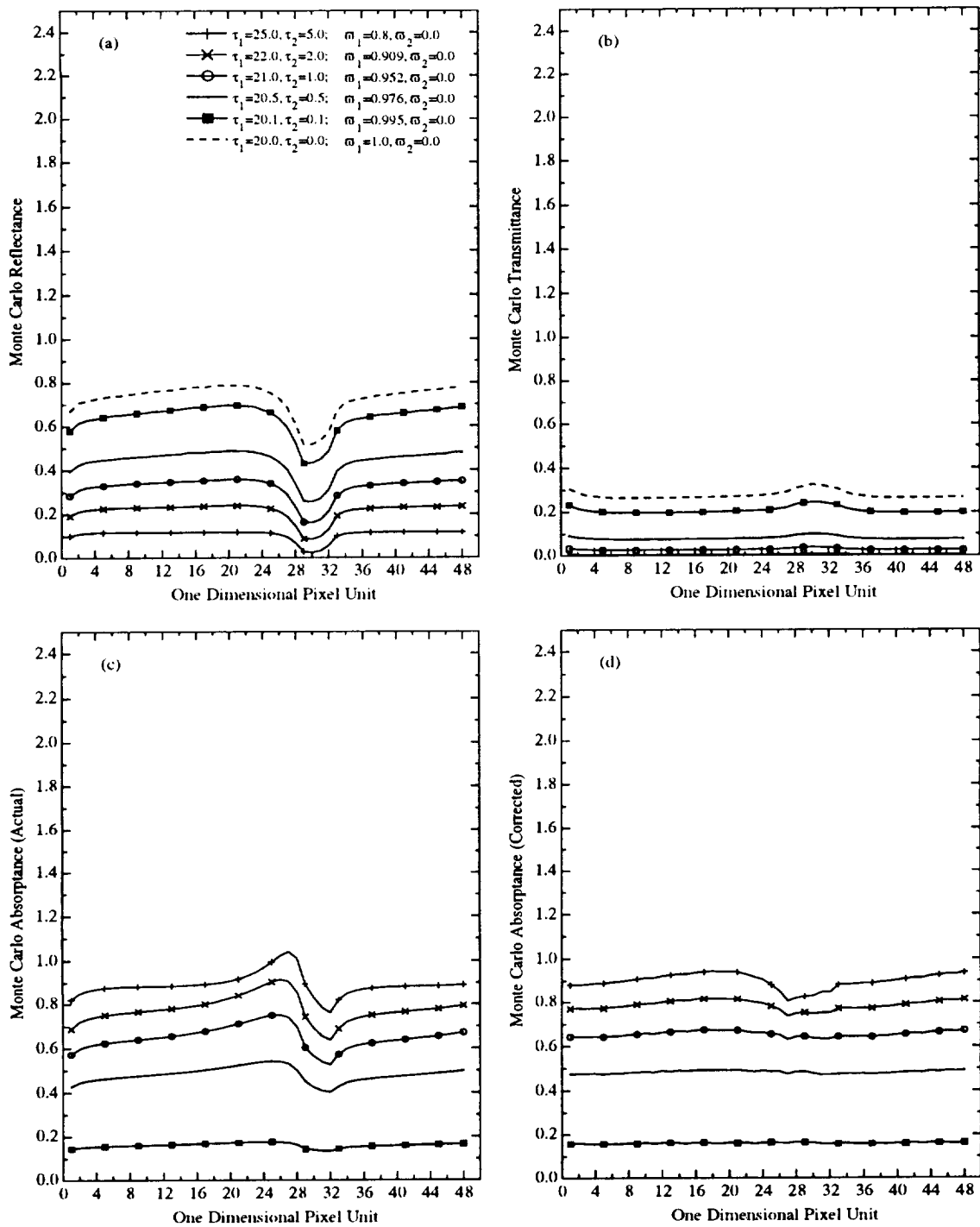
Figure 3.15 Same as Figure 3.5 except for a cloud fraction of 87.5% and aspect ratio of 1.0.
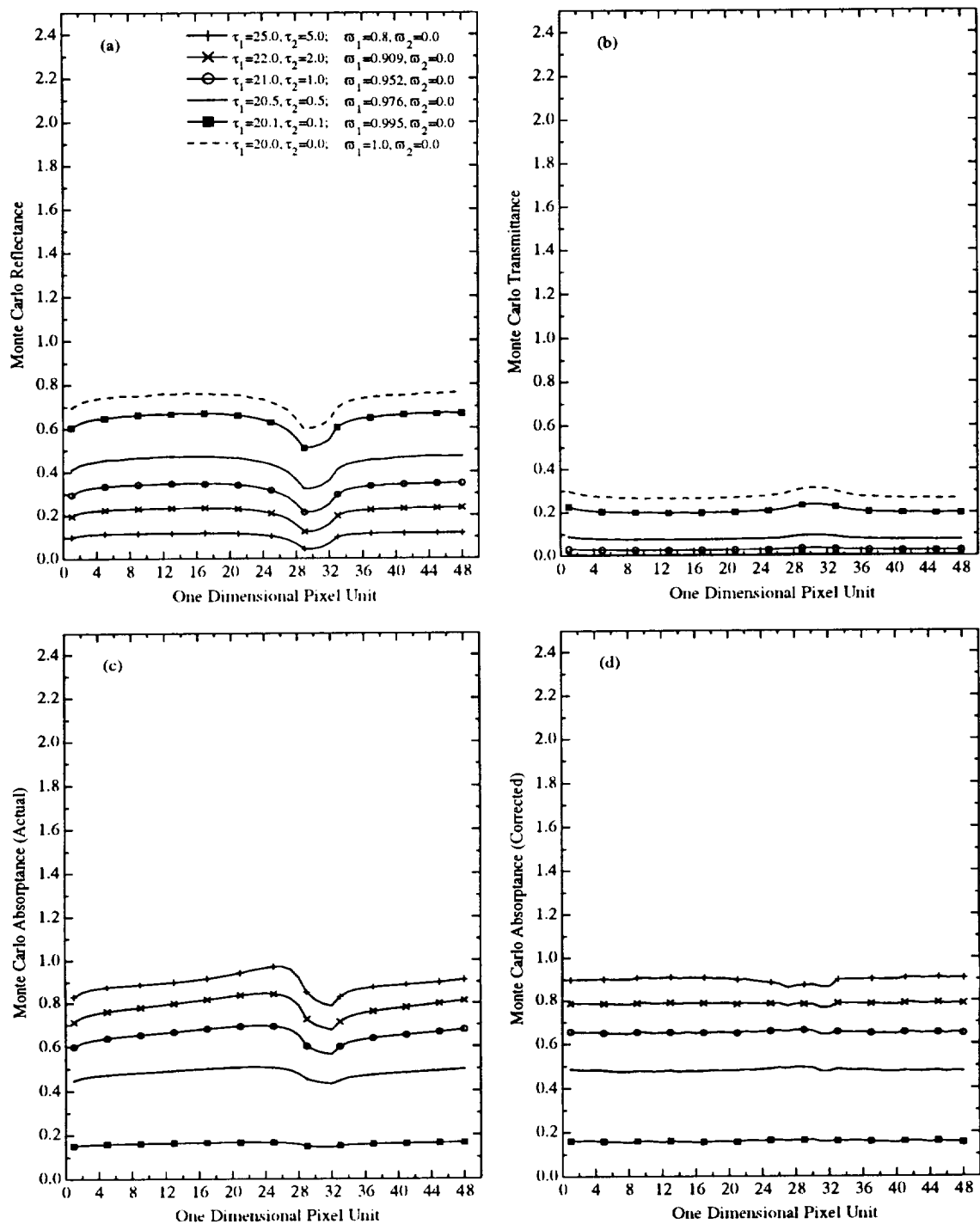
Figure 3.16 Same as Figure 3.5 except for a cloud fraction of 87.5% and aspect ratio of 2.0.

Figure 3.17   Monte Carlo (a) reflectance, (b) transmittance, (c) absorptance, and (d) corrected absorptance for the second study with a cloud fraction of 12.5% and aspect ratio of 0.25.

Figure 3.18 Same as Figure 3.17 except for a cloud fraction of 12.5% and aspect ratio of 0.5.

Figure 3.19 Same as Figure 3.17 except for a cloud fraction of 12.5% and aspect ratio of 1.0.

Figure 3.20 Same as Figure 3.17 except for a cloud fraction of 12.5% and aspect ratio of 2.0.

Figure 3.21 Same as Figure 3.17 except for a cloud fraction of 50% and aspect ratio of 0.25.
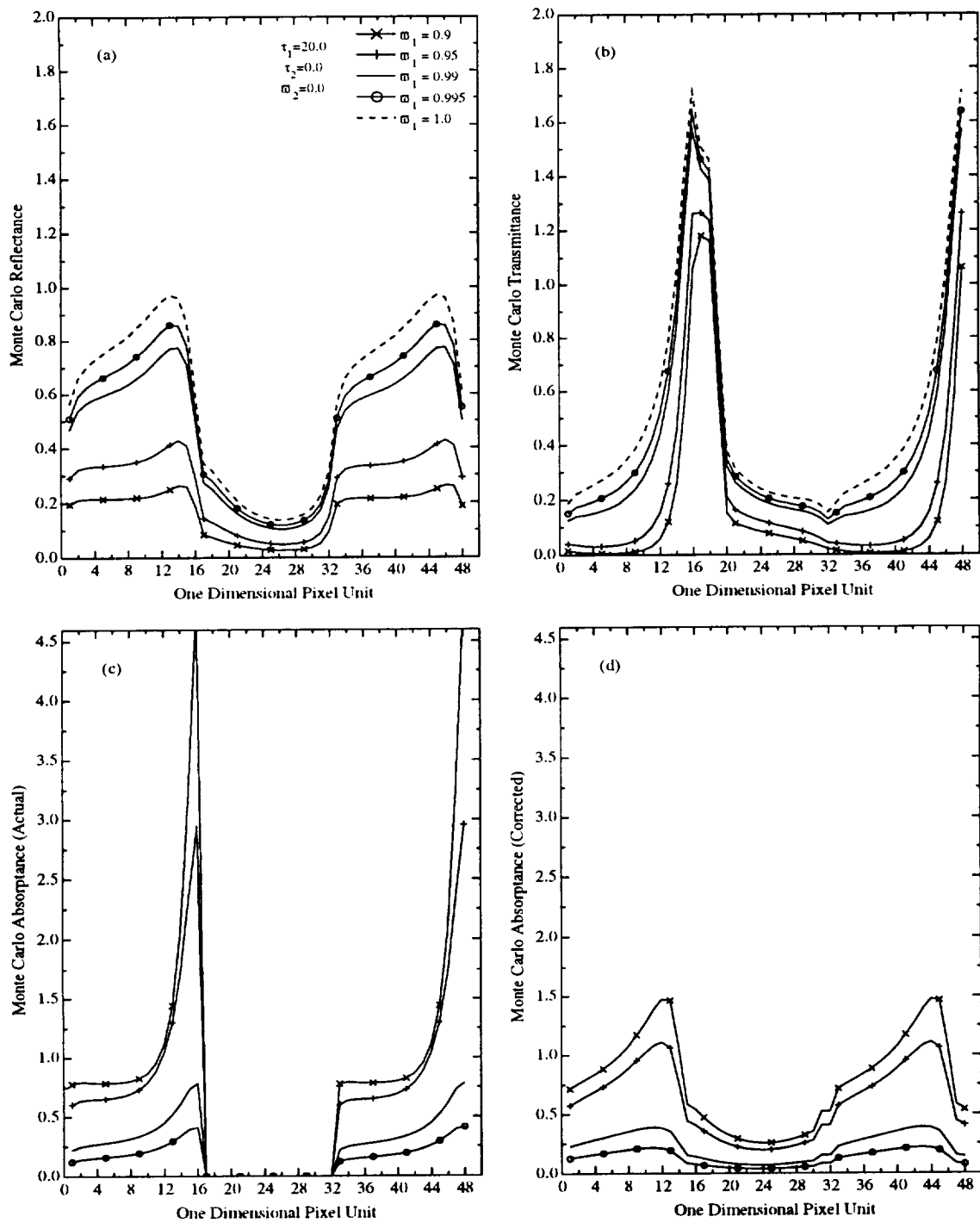
Figure 3.22 Same as Figure 3.17 except for a cloud fraction of 50% and aspect ratio of 0.5.
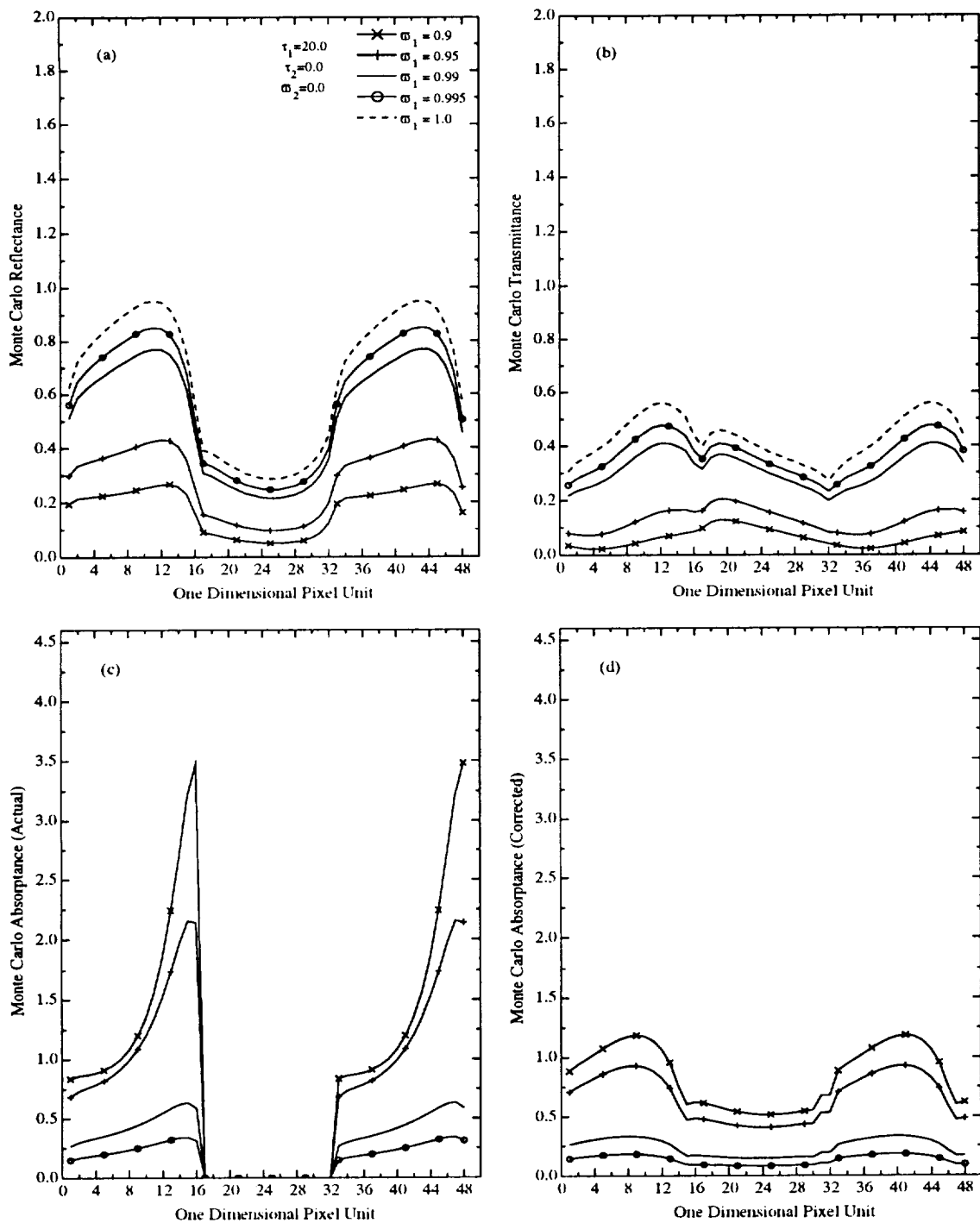
Figure 3.23 Same as Figure 3.17 except for a cloud fraction of 50% and aspect ratio of 1.0.
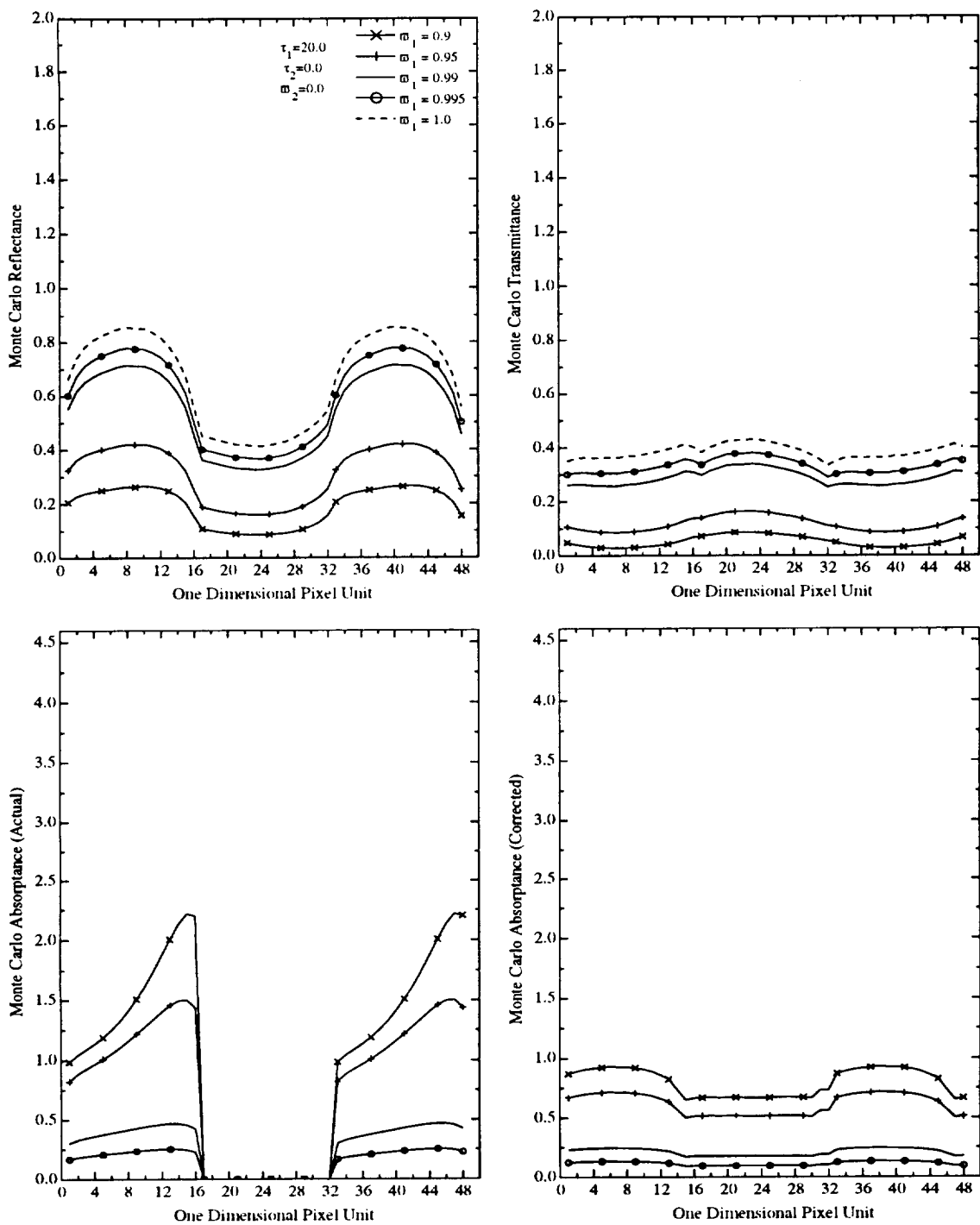
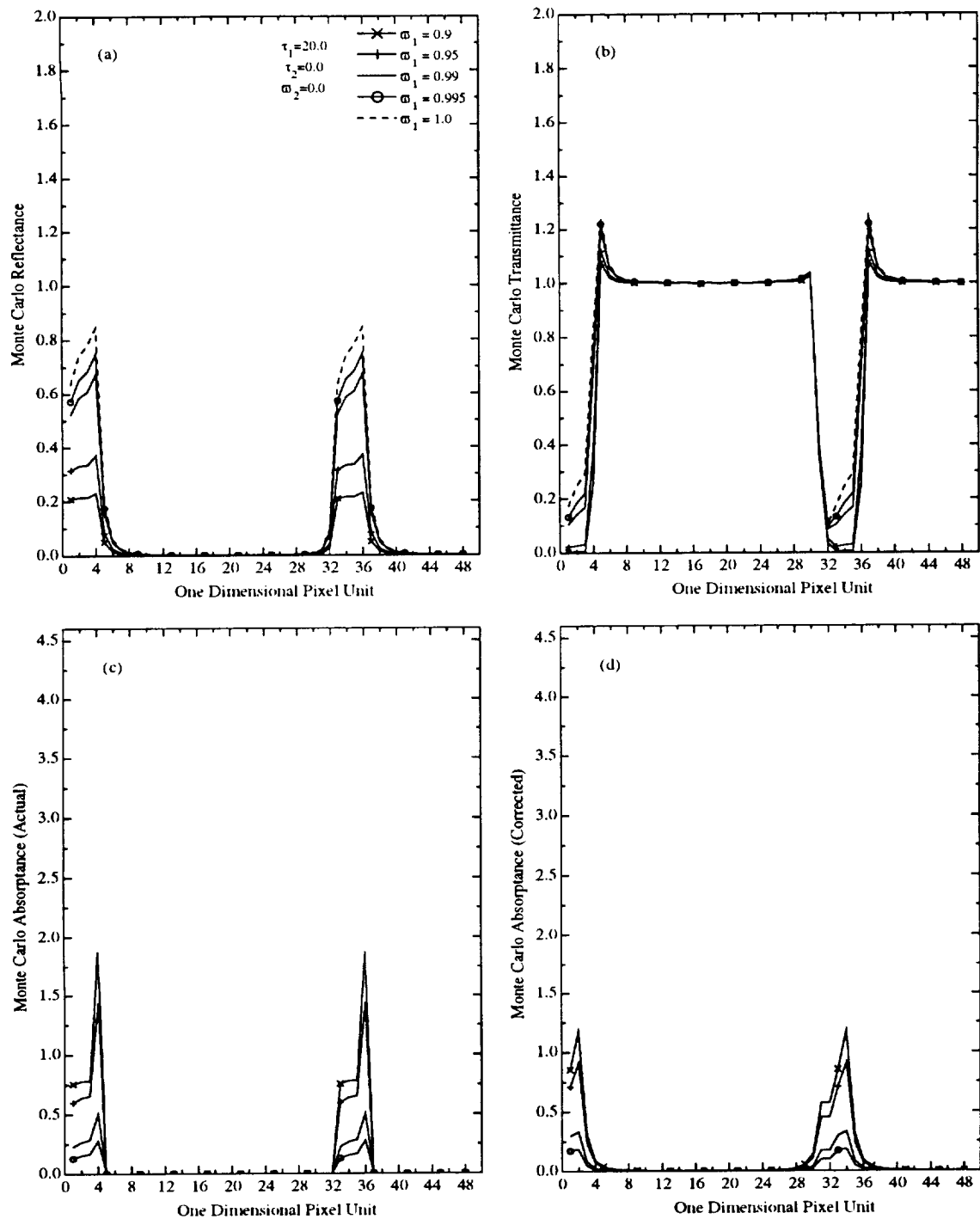Figure 3.24 Same as Figure 3.17 except for a cloud fraction of 50% and aspect ratio of 2.0.
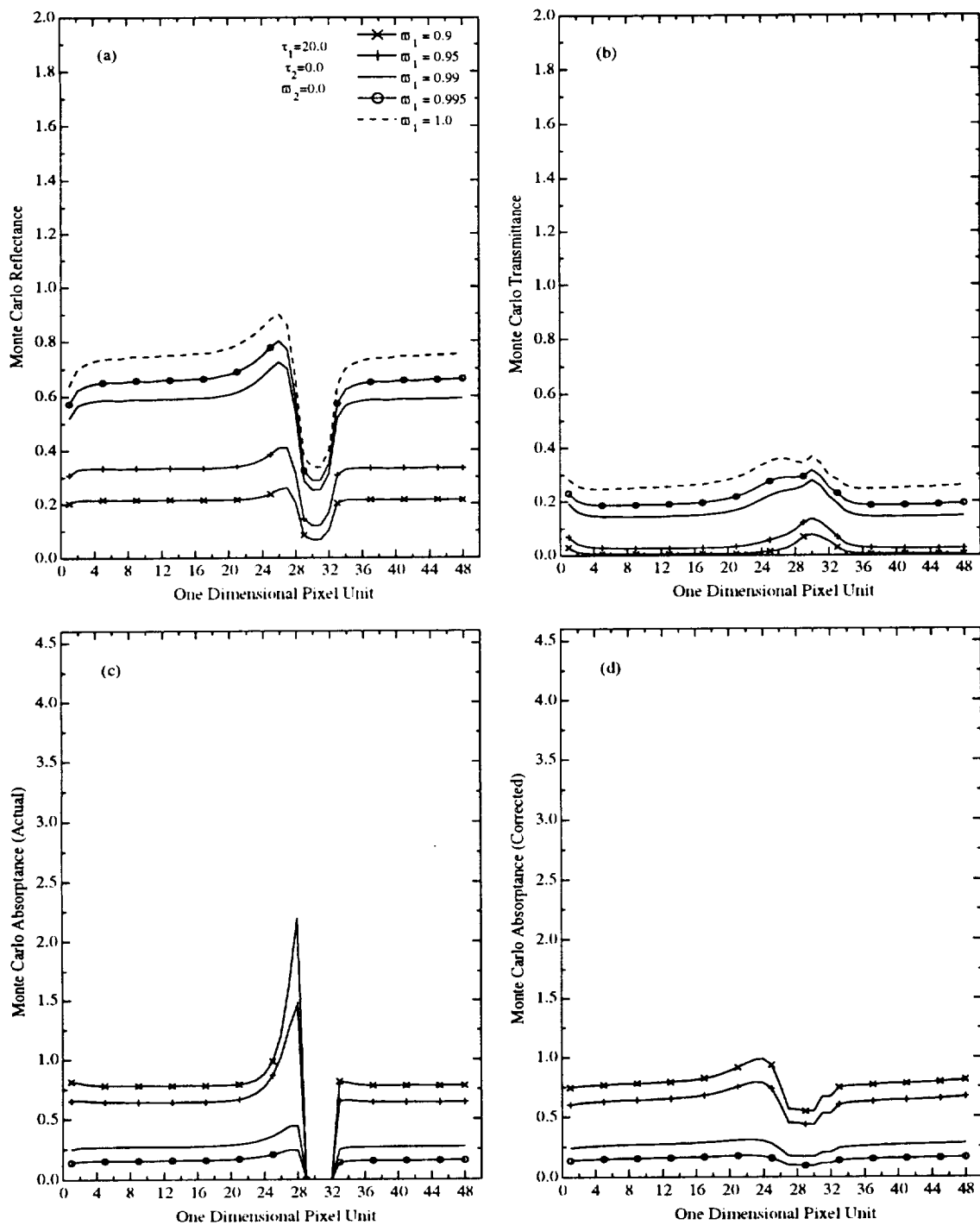
Figure 3.25 Same as Figure 3.17 except for a cloud fraction of 87.5% and aspect ratio of 0.25.
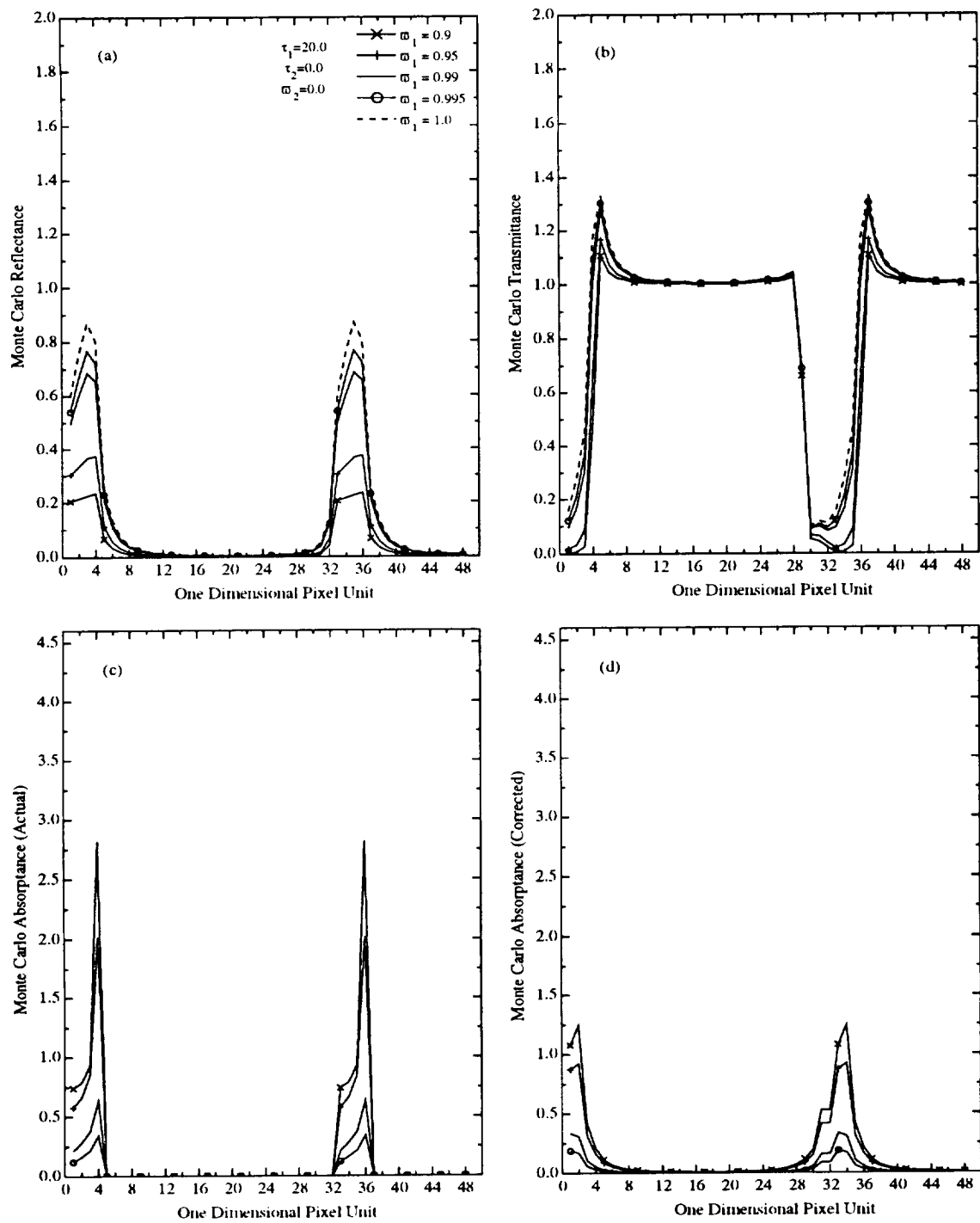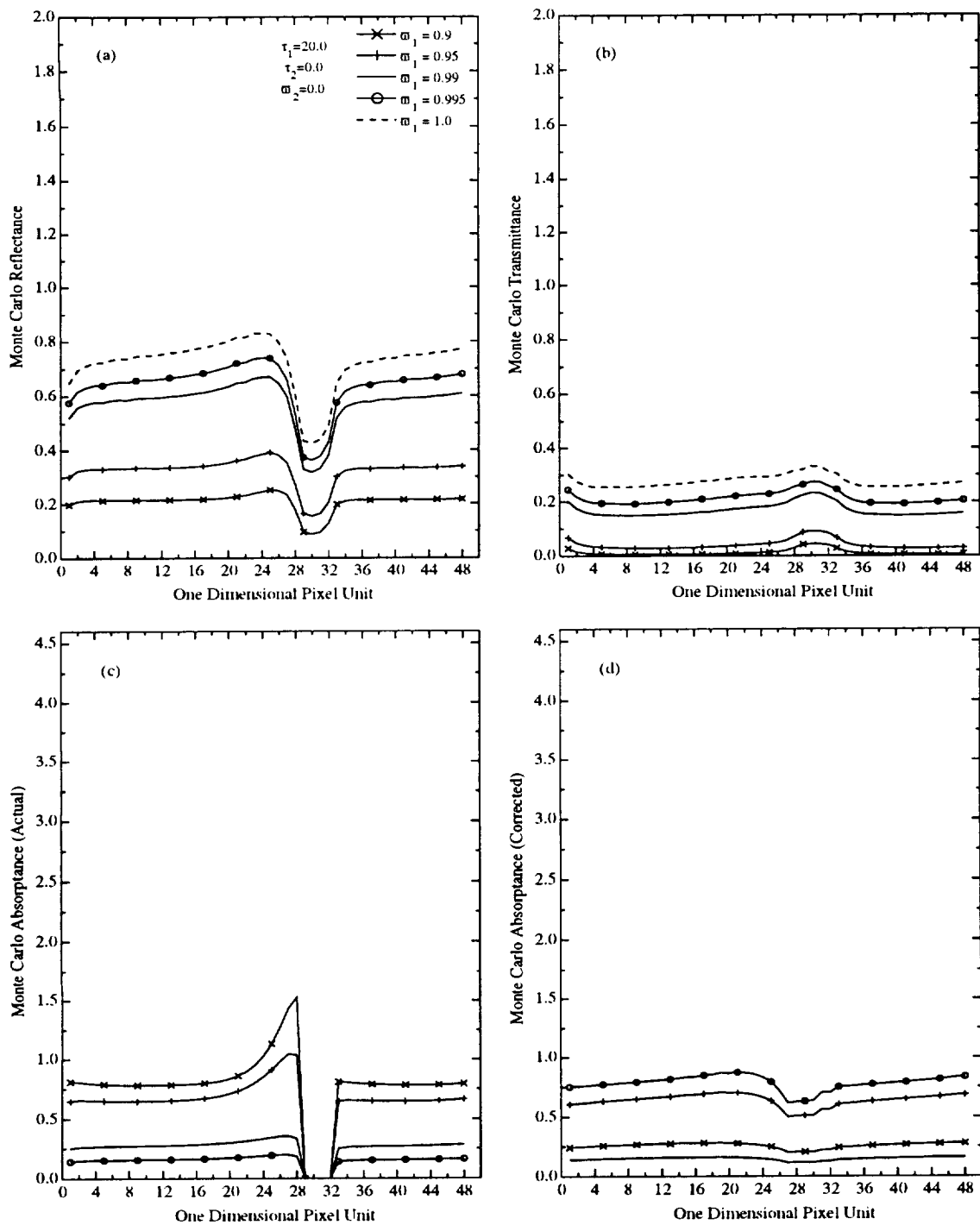
Figure 3.26 Same as Figure 3.17 except for a cloud fraction of 87.5% and aspect ratio of 0.5.
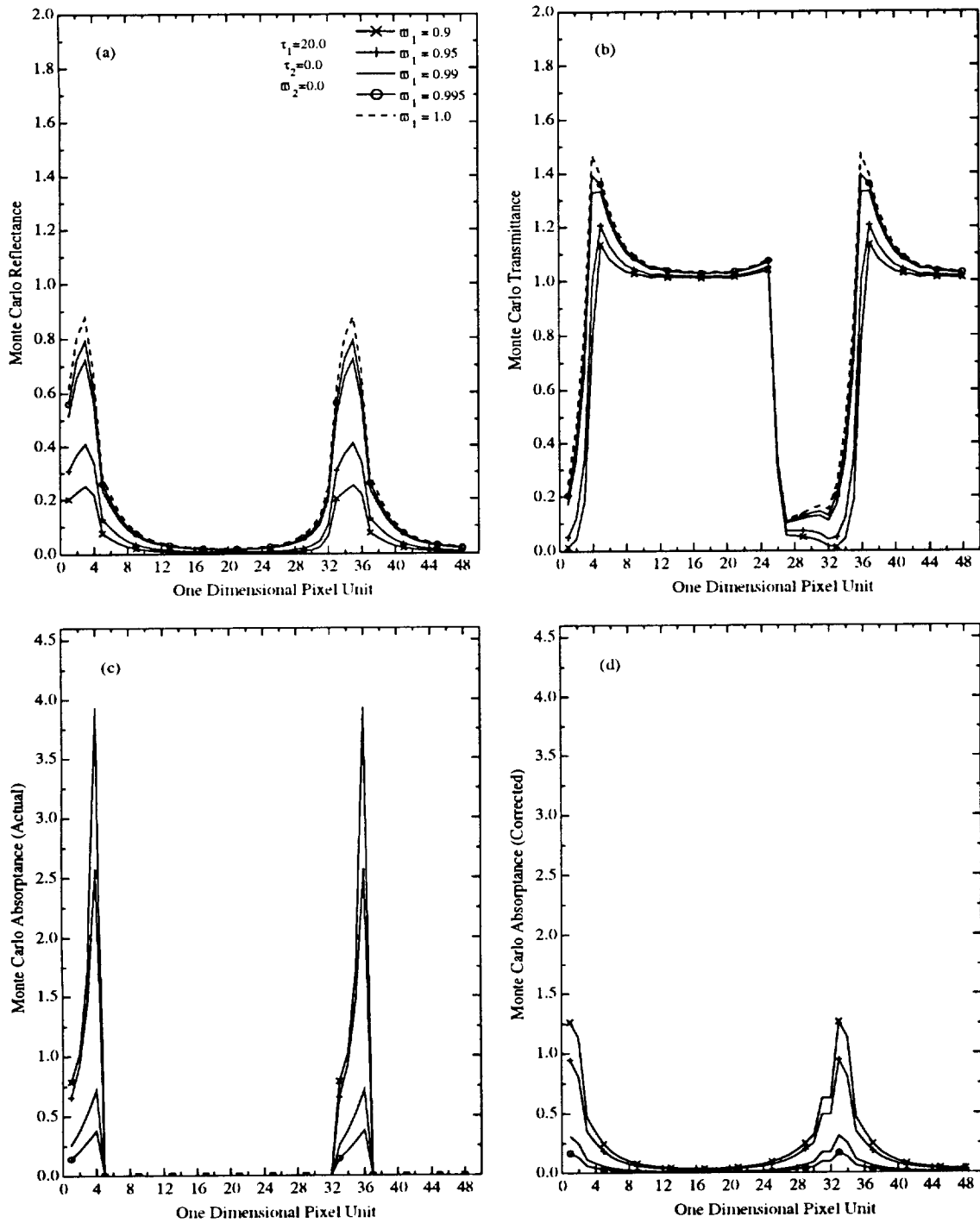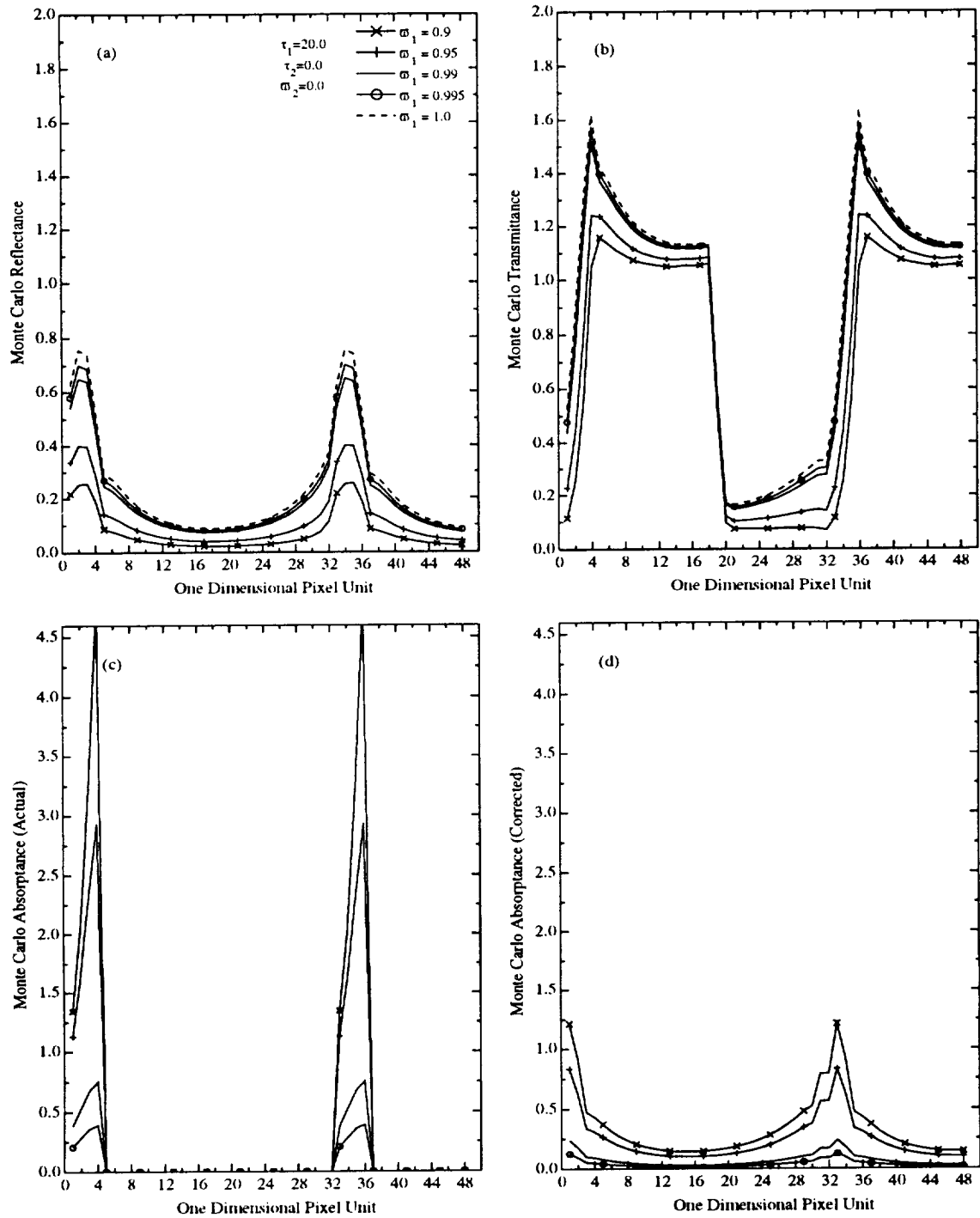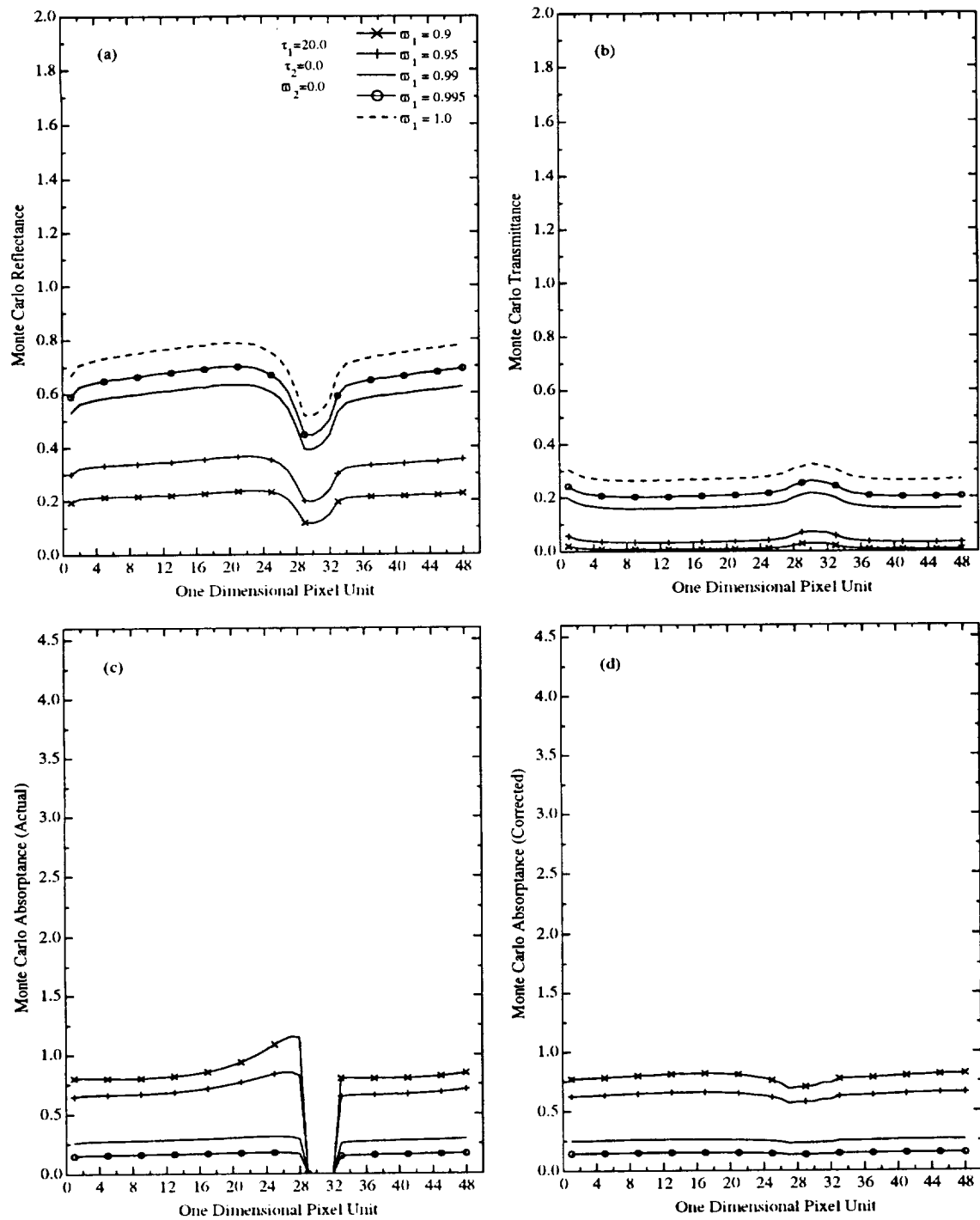
Figure 3.27 Same as Figure 3.17 except for a cloud fraction of 87.5% and aspect ratio of 1.0.

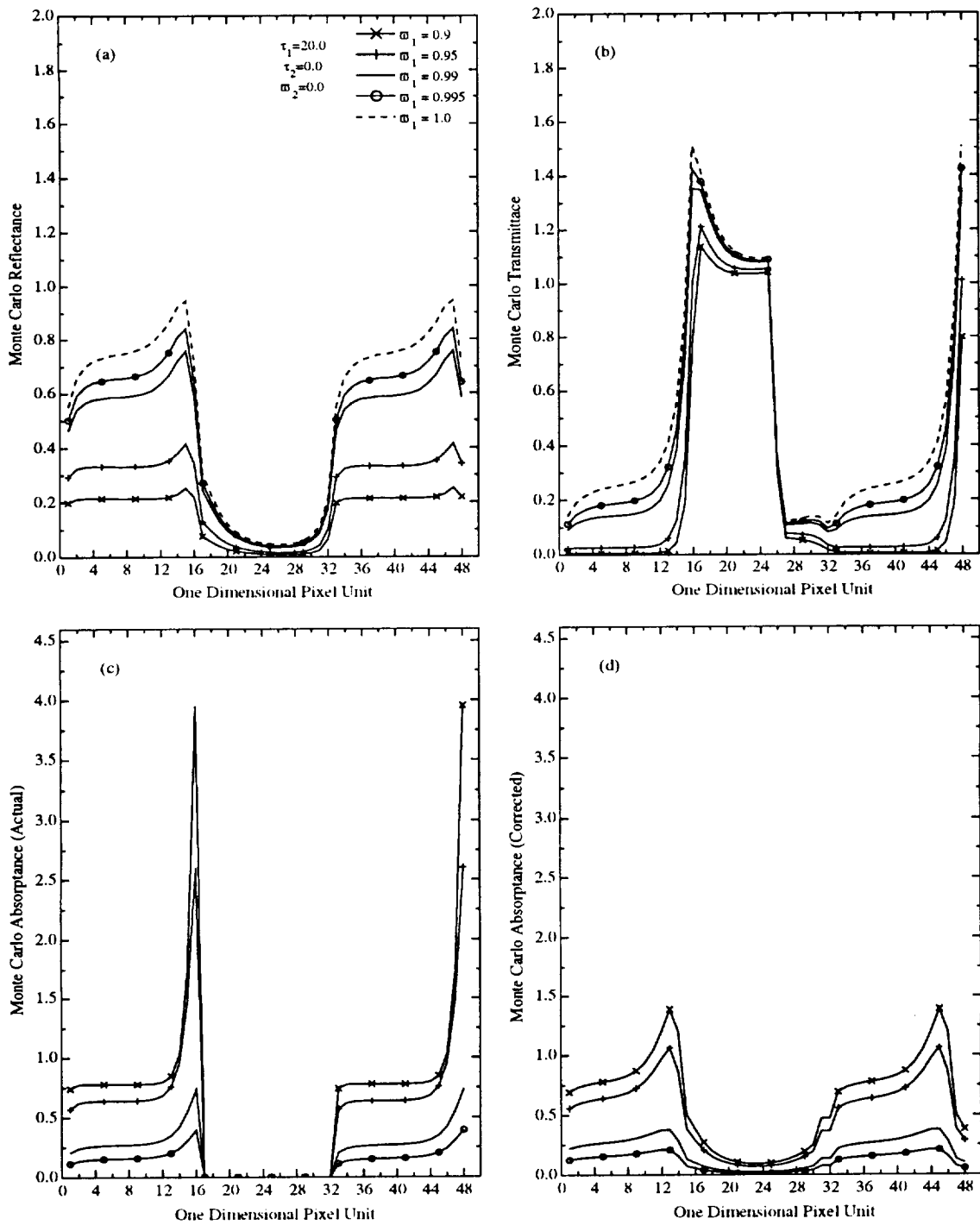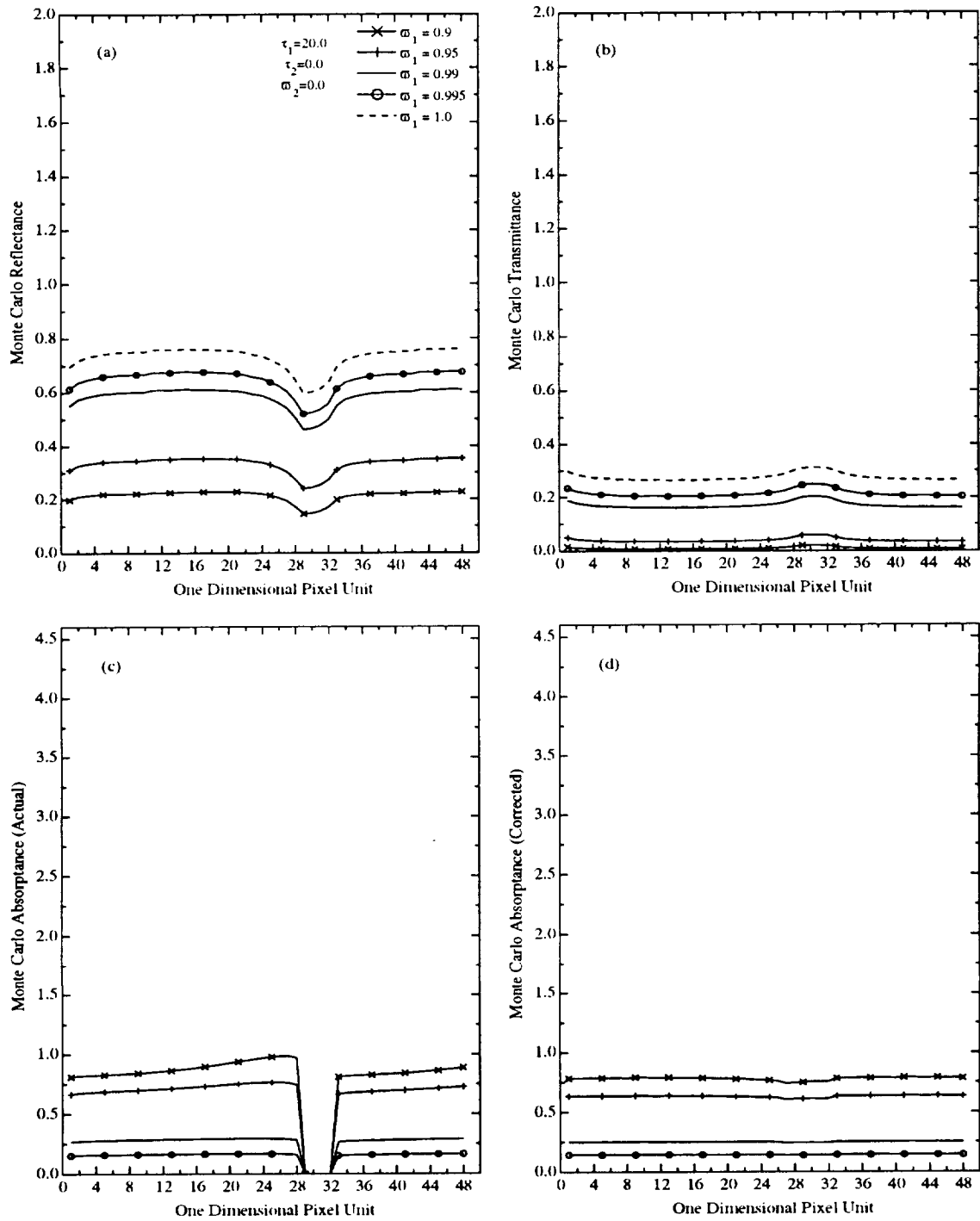Figure 3.28 Same as Figure 3.17 except for a cloud fraction of 87.5% and aspect ratio of 2.0.
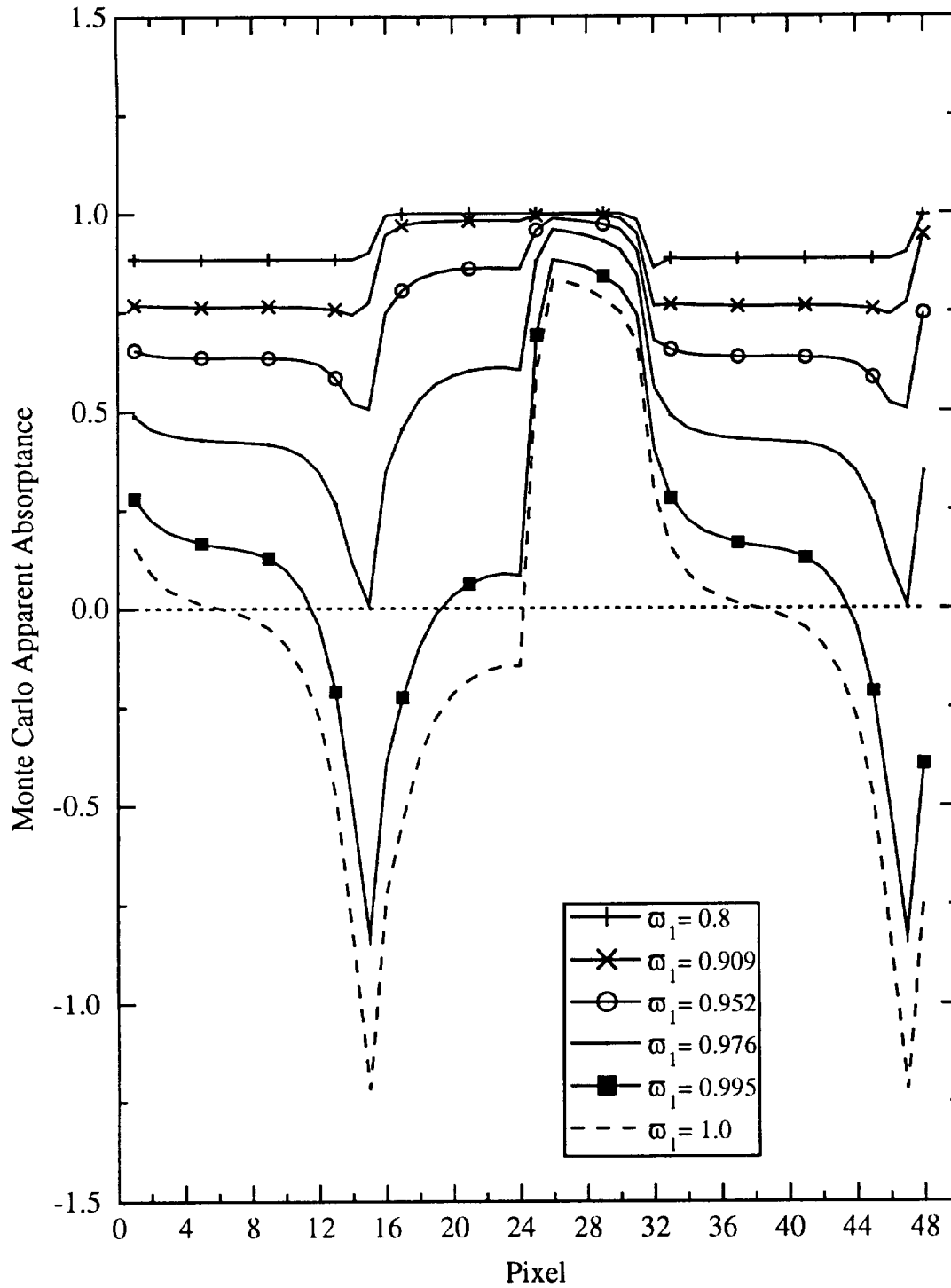
Figure 3.29 Apparent absorptance for $N_C = 50\%$ and a = 0.25 geometric values, and conservative droplet scattering for different vapor absorptance values.
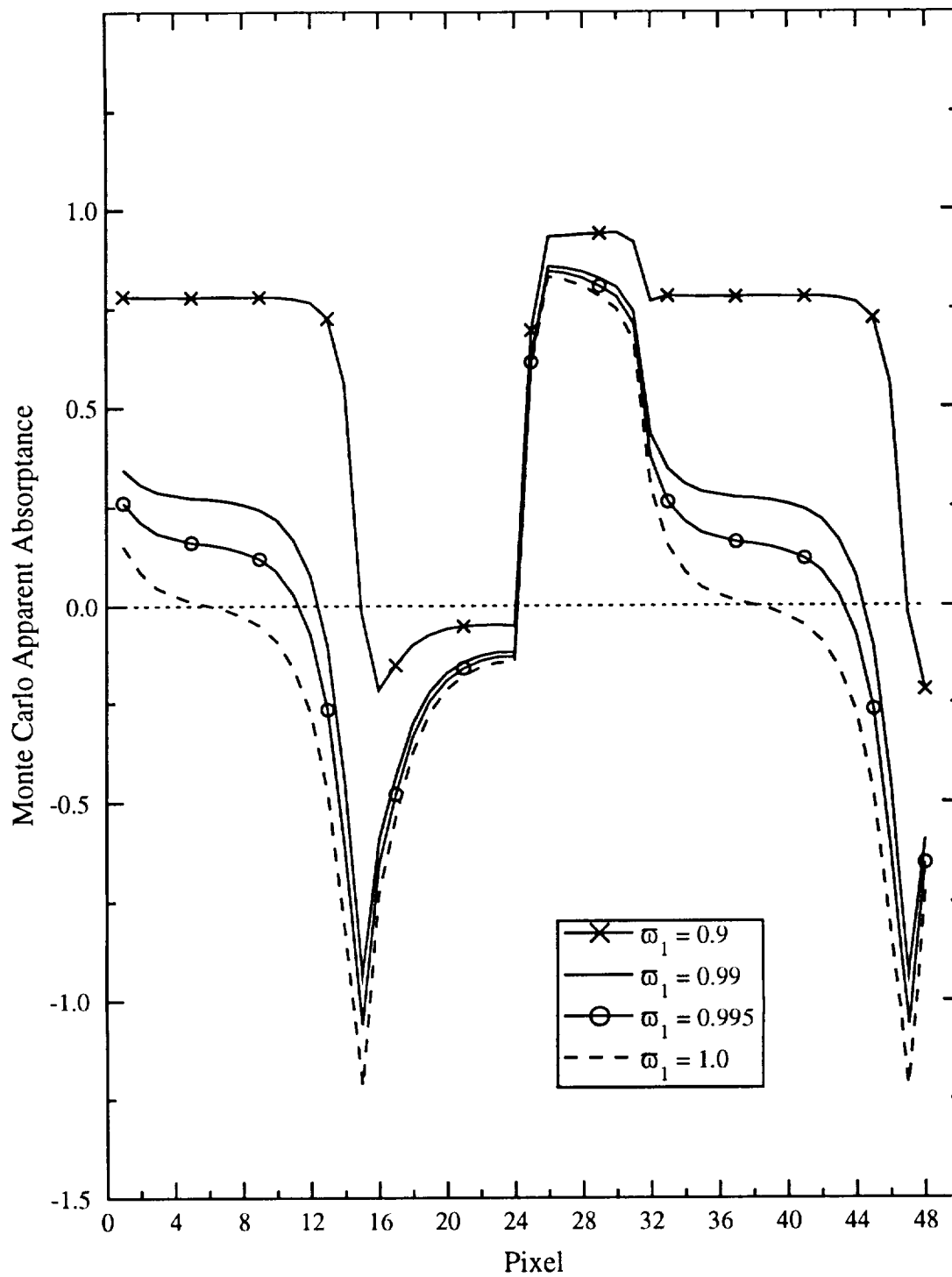
Figure 3.30 Apparent absorptance for $N_C = 50\%$ and $a = 0.25$ geometric values, and zero vapor absorption values.
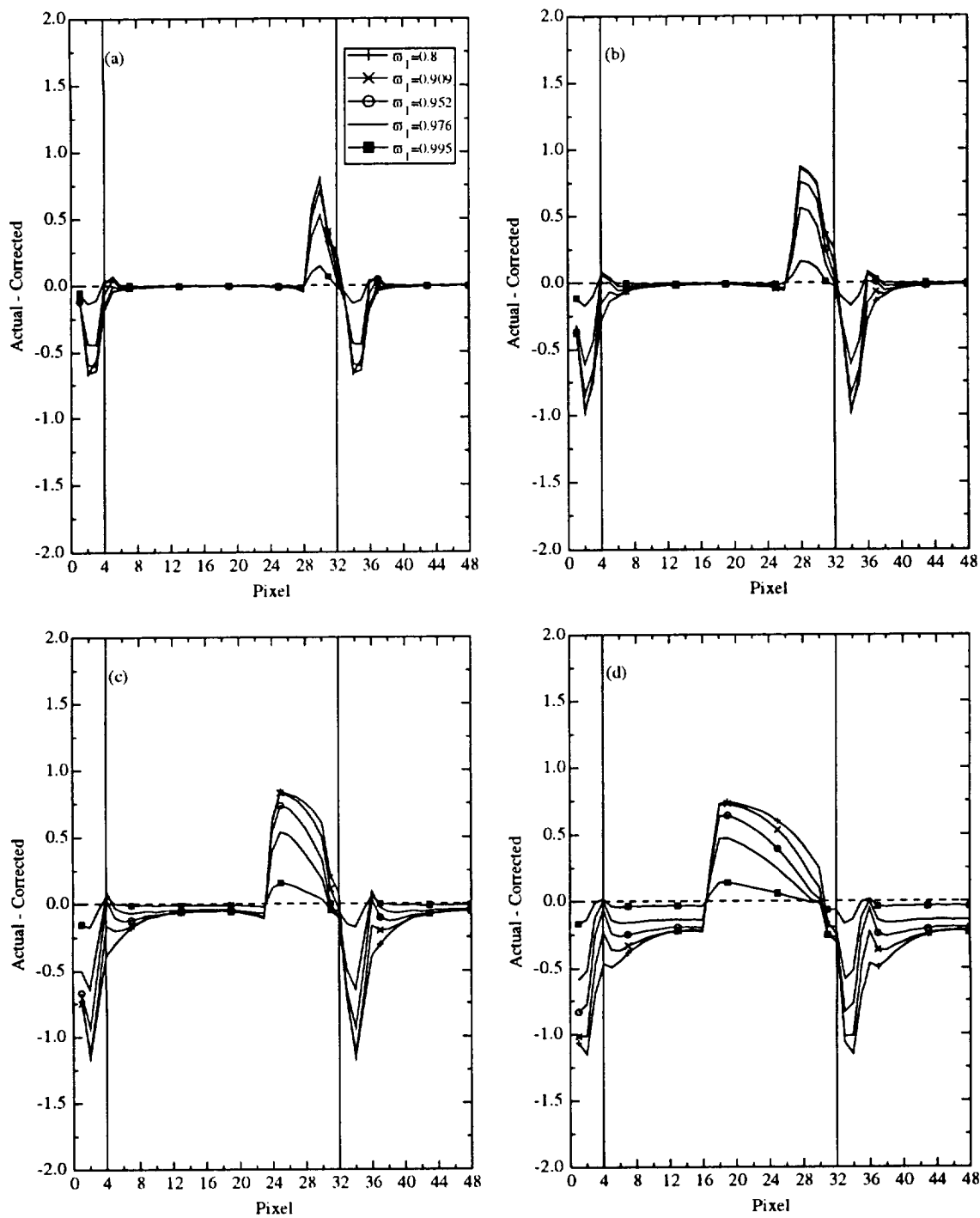
Figure 3.31 Difference between the Monte Carlo Absorptance (actual) and the Corrected Absorption by the Ackerman and Cox method for the first study. For a 12.5% cloud fraction and aspect ratio of (a) 0.25, (b) 0.5, (c) 1.0, and (d) 2.0.
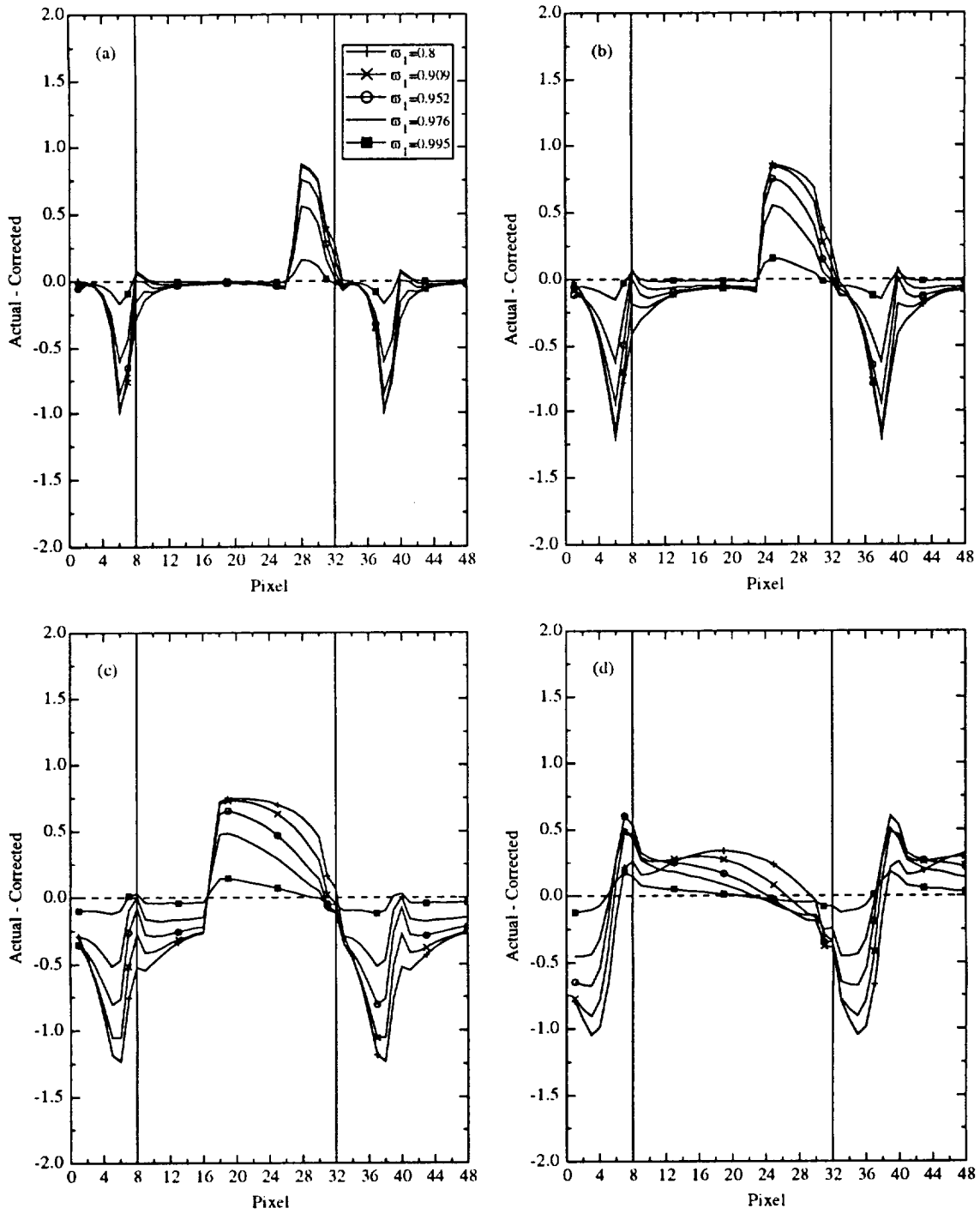
Figure 3.32 Same as Figure 3.31 except for a 25% cloud fraction.
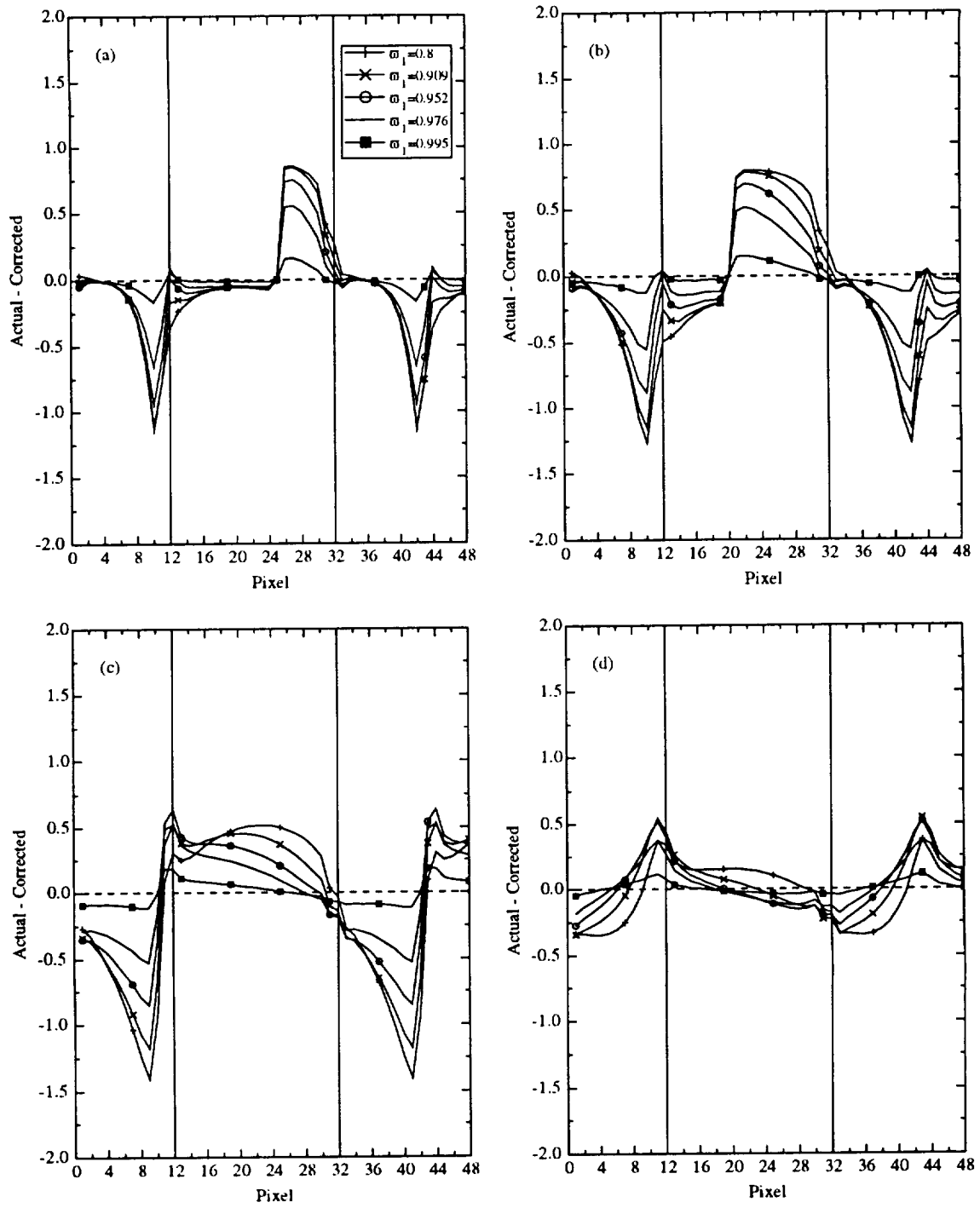
Figure 3.33 Same as Figure 3.31 except for a 37.5% cloud fraction.
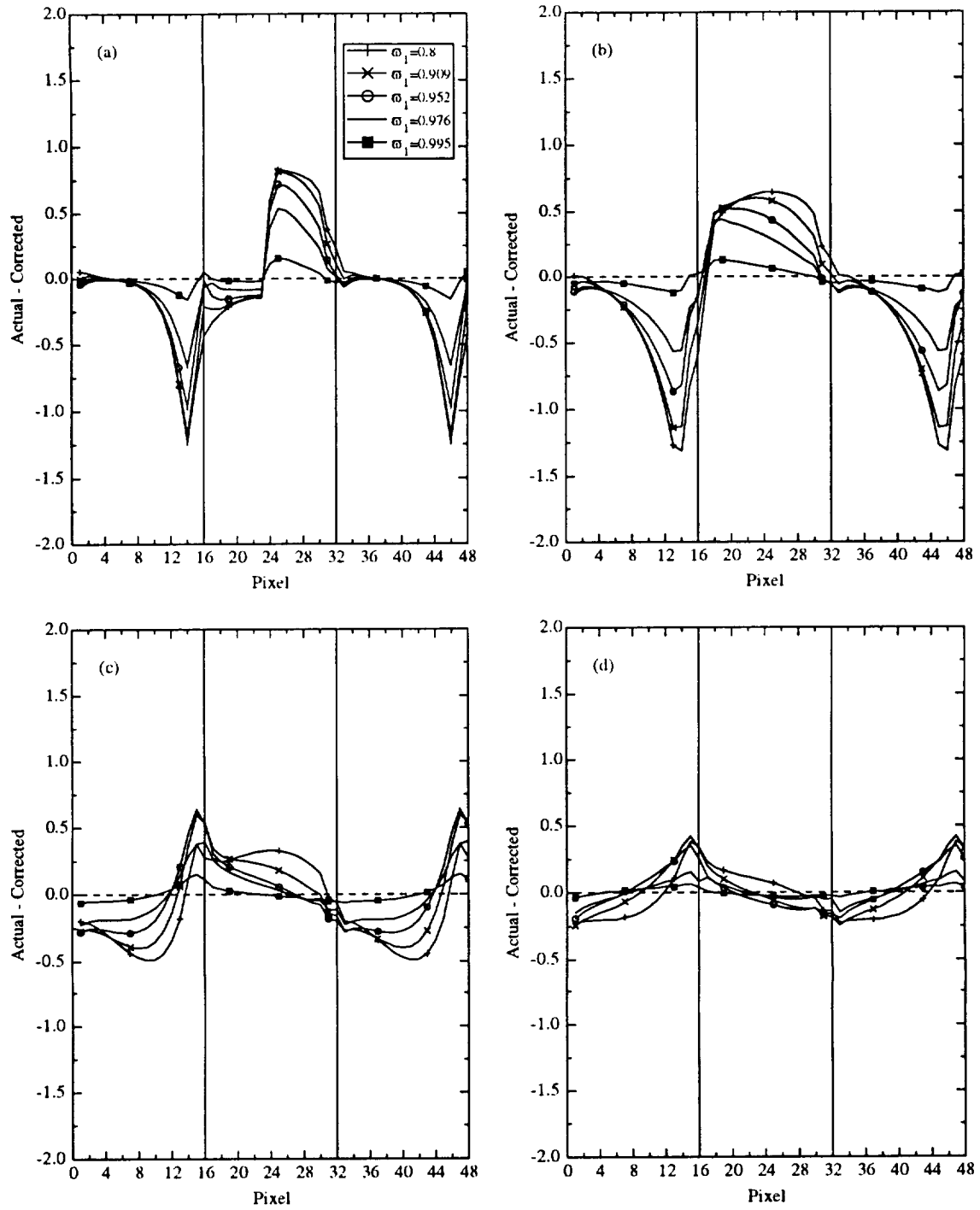
Figure 3.34 Same as Figure 3.31 except for a 50% cloud fraction.
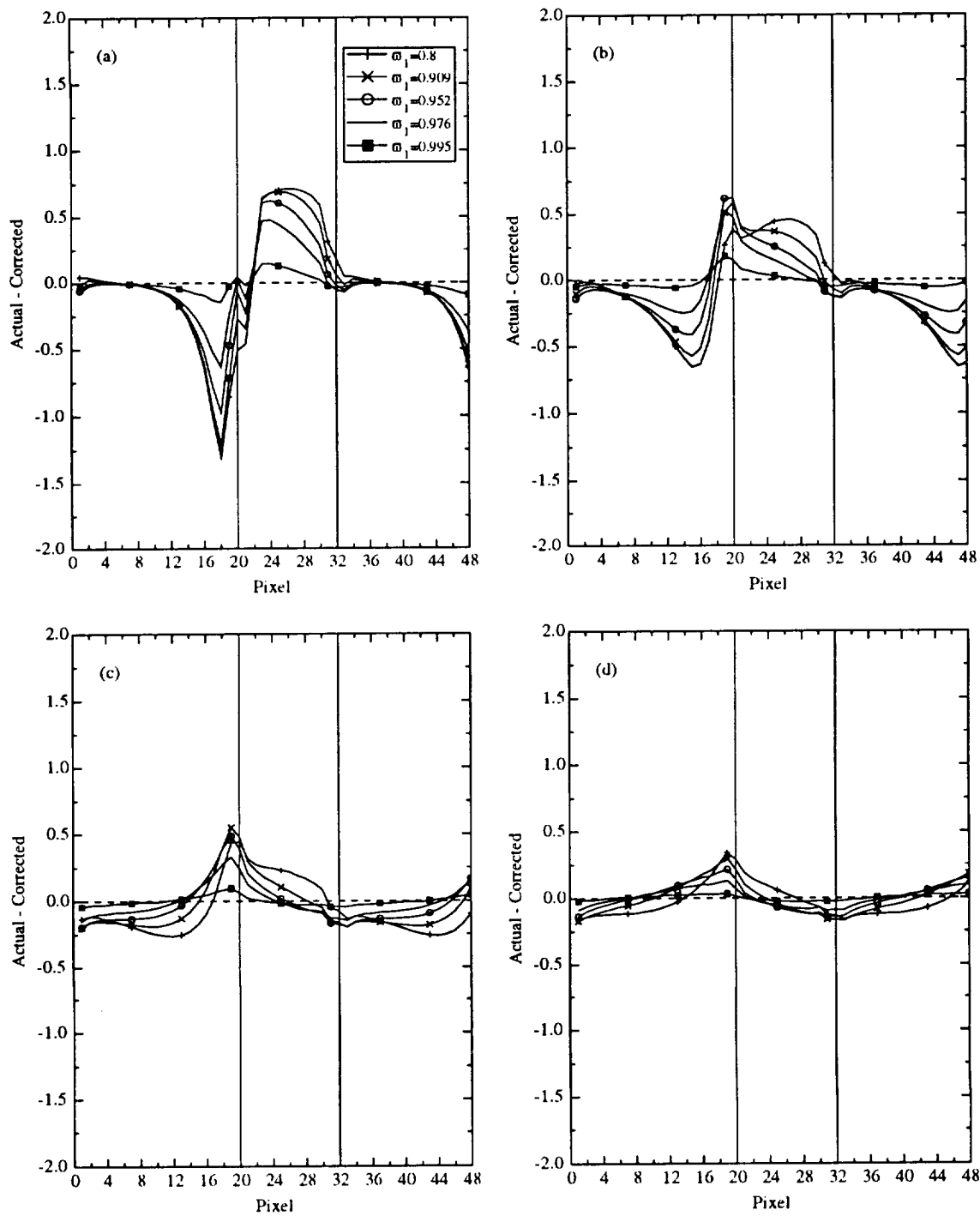
Figure 3.35 Same as Figure 3.31 except for a 62.5% cloud fraction.
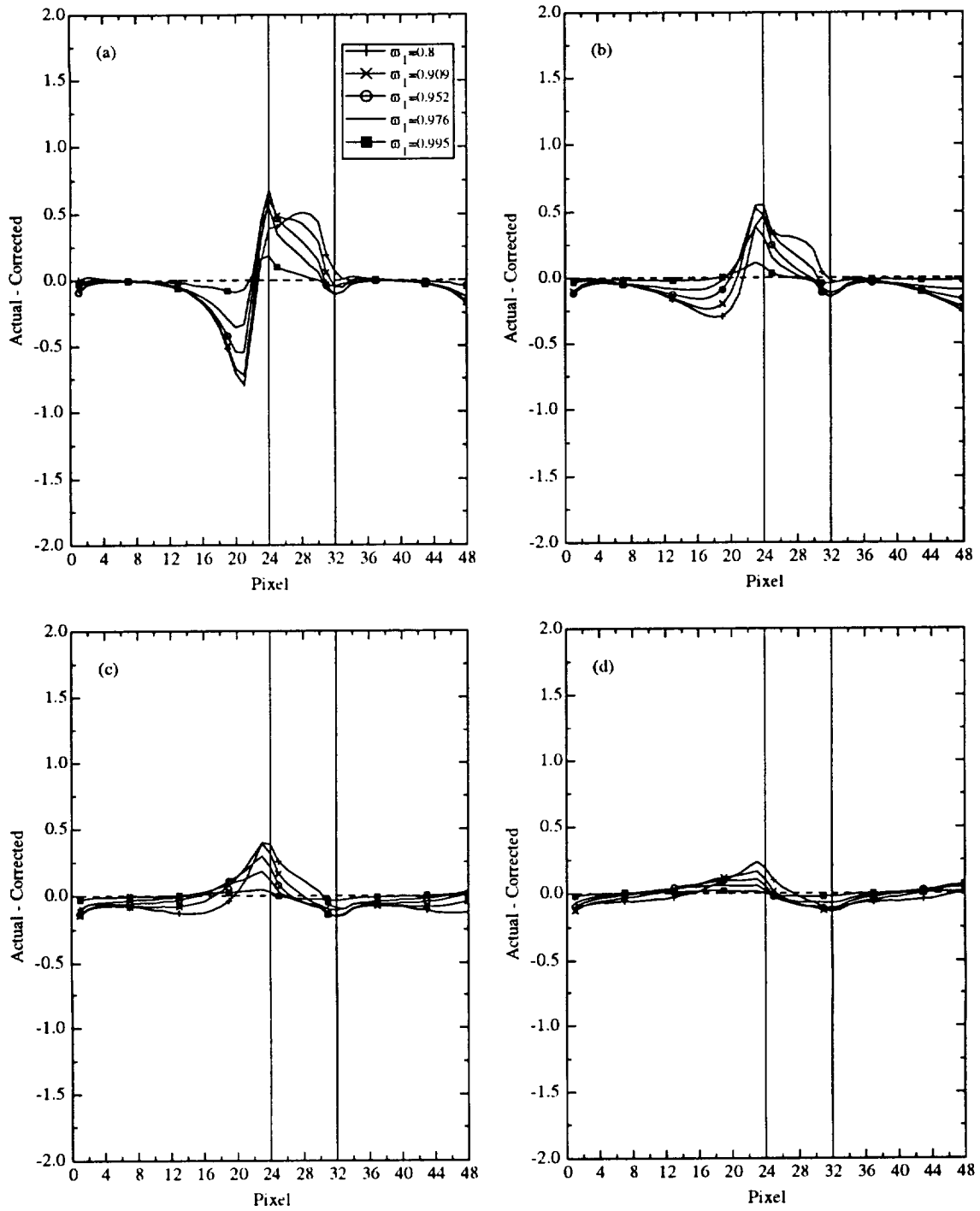
Figure 3.36 Same as Figure 3.31 except for a 75% cloud fraction.
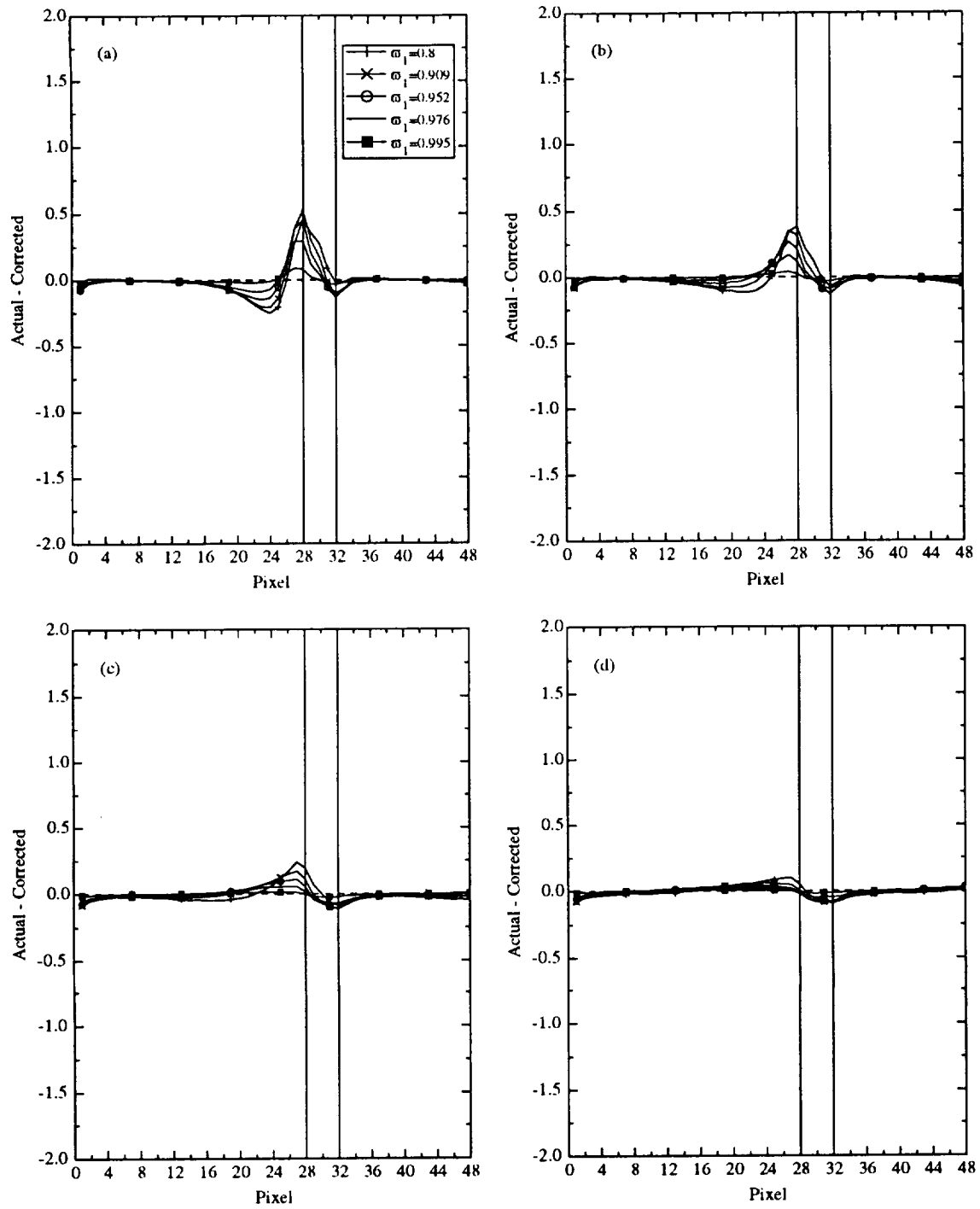
Figure 3.37 Same as Figure 3.31 except for a 87.5% cloud fraction.
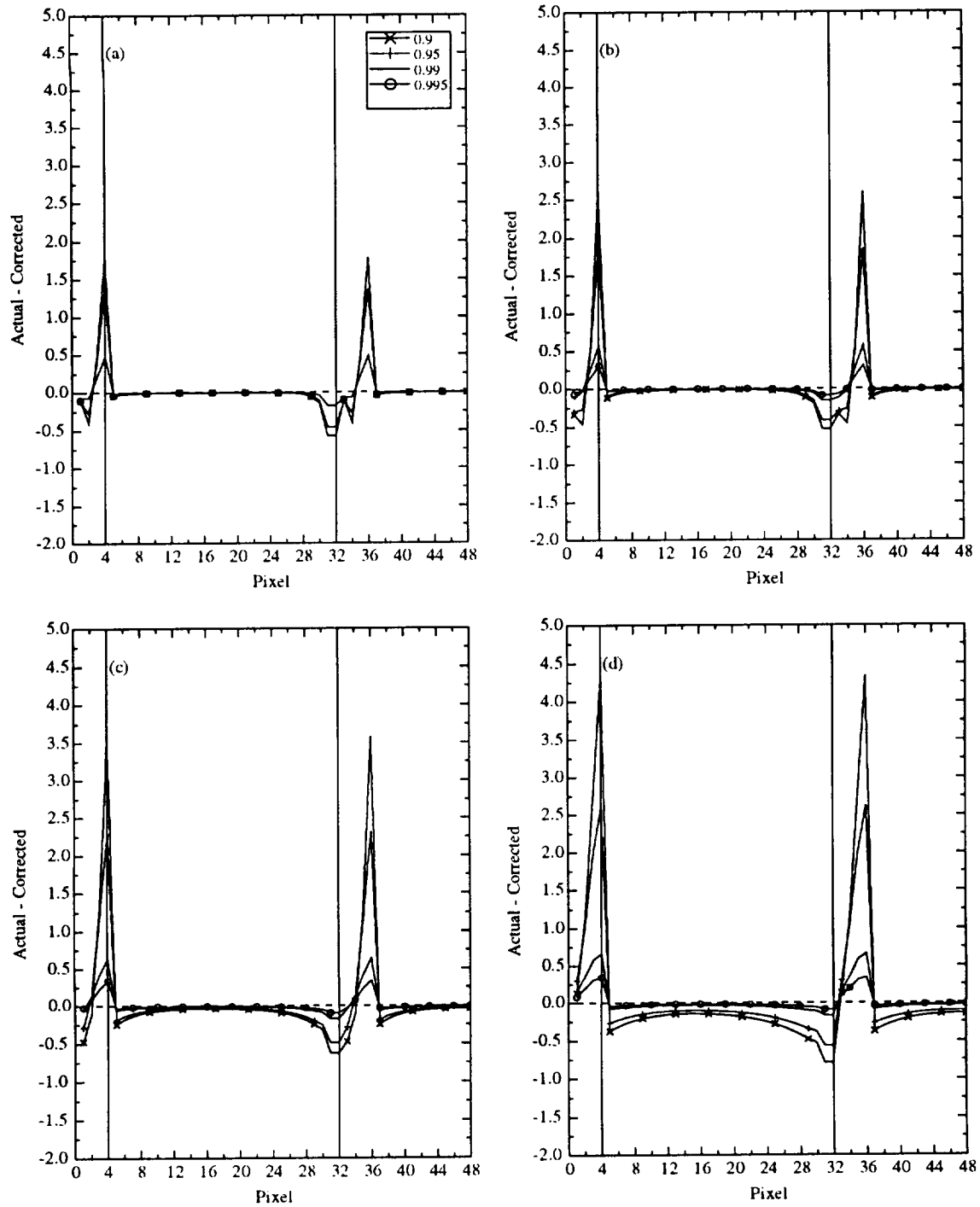
Figure 3.38 Difference between the Monte Carlo Absorptance (actual) and the Corrected Absorption by the Ackerman and Cox method for the second study. For a 12.5% cloud fraction and aspect ratio of (a) 0.25, (b) 0.5, (c) 1.0, and (d) 2.0.
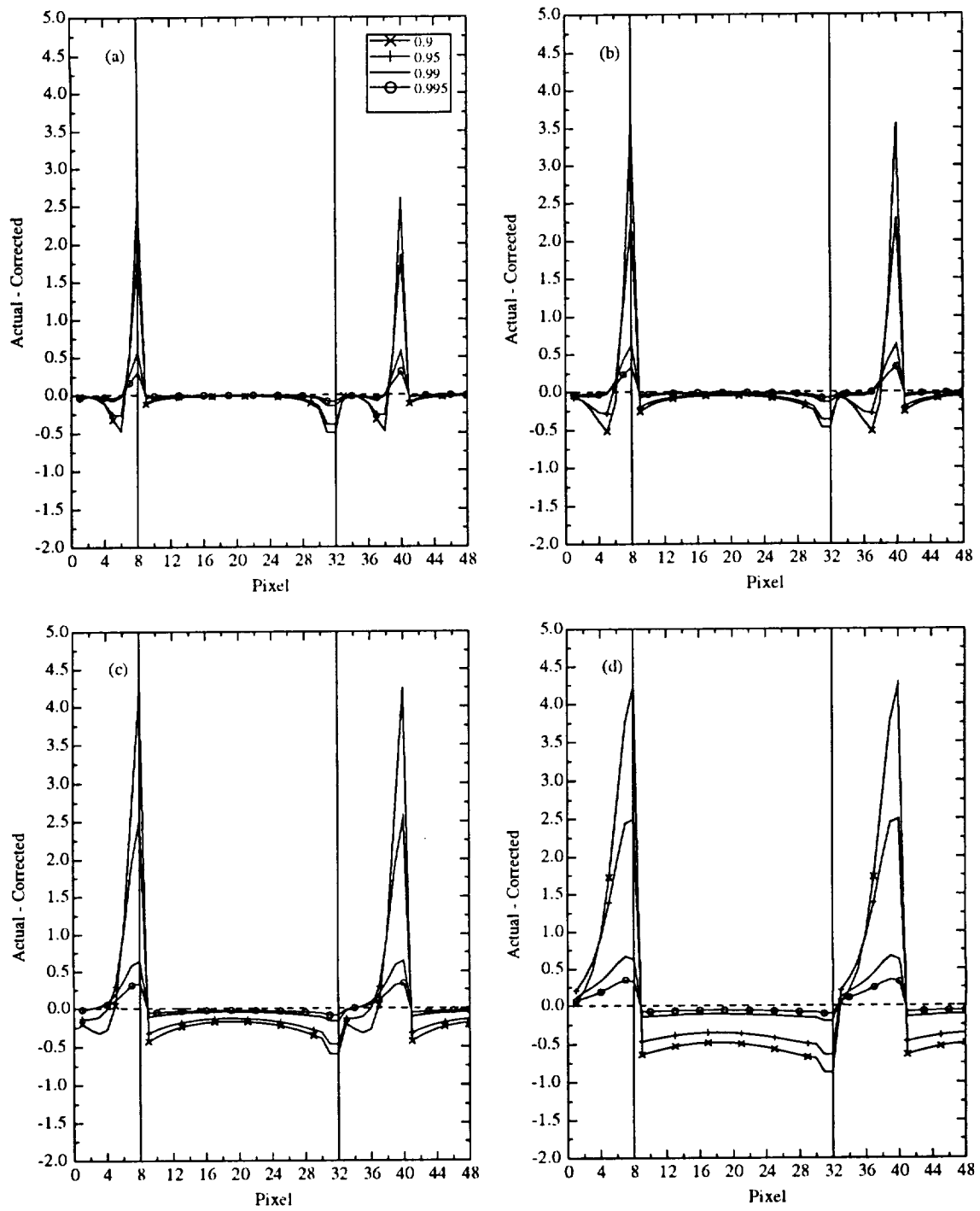
Figure 3.39 Same as Figure 3.38 except for a 25% cloud fraction.
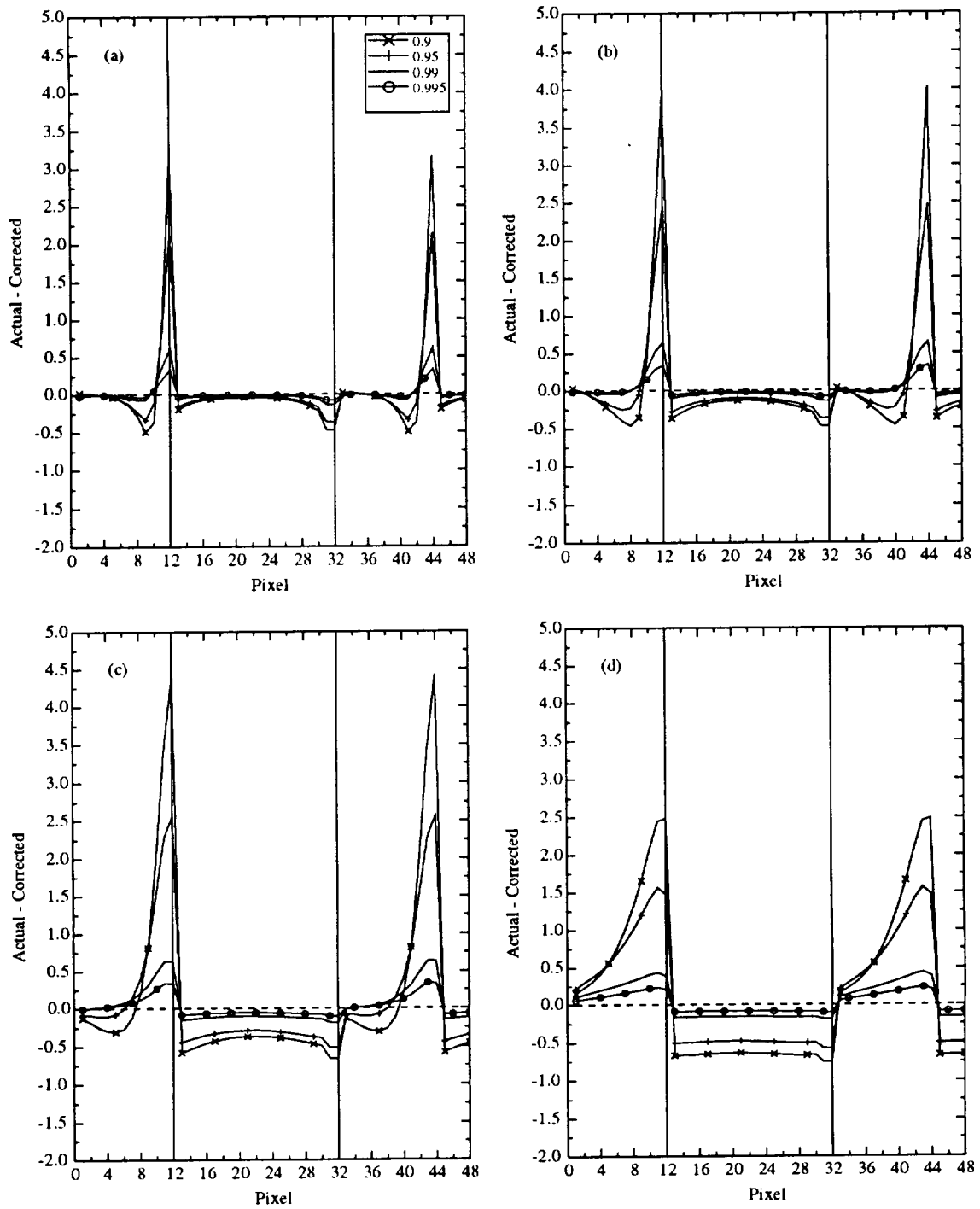
Figure 3.40 Same as Figure 3.38 except for a 37.5% cloud fraction.
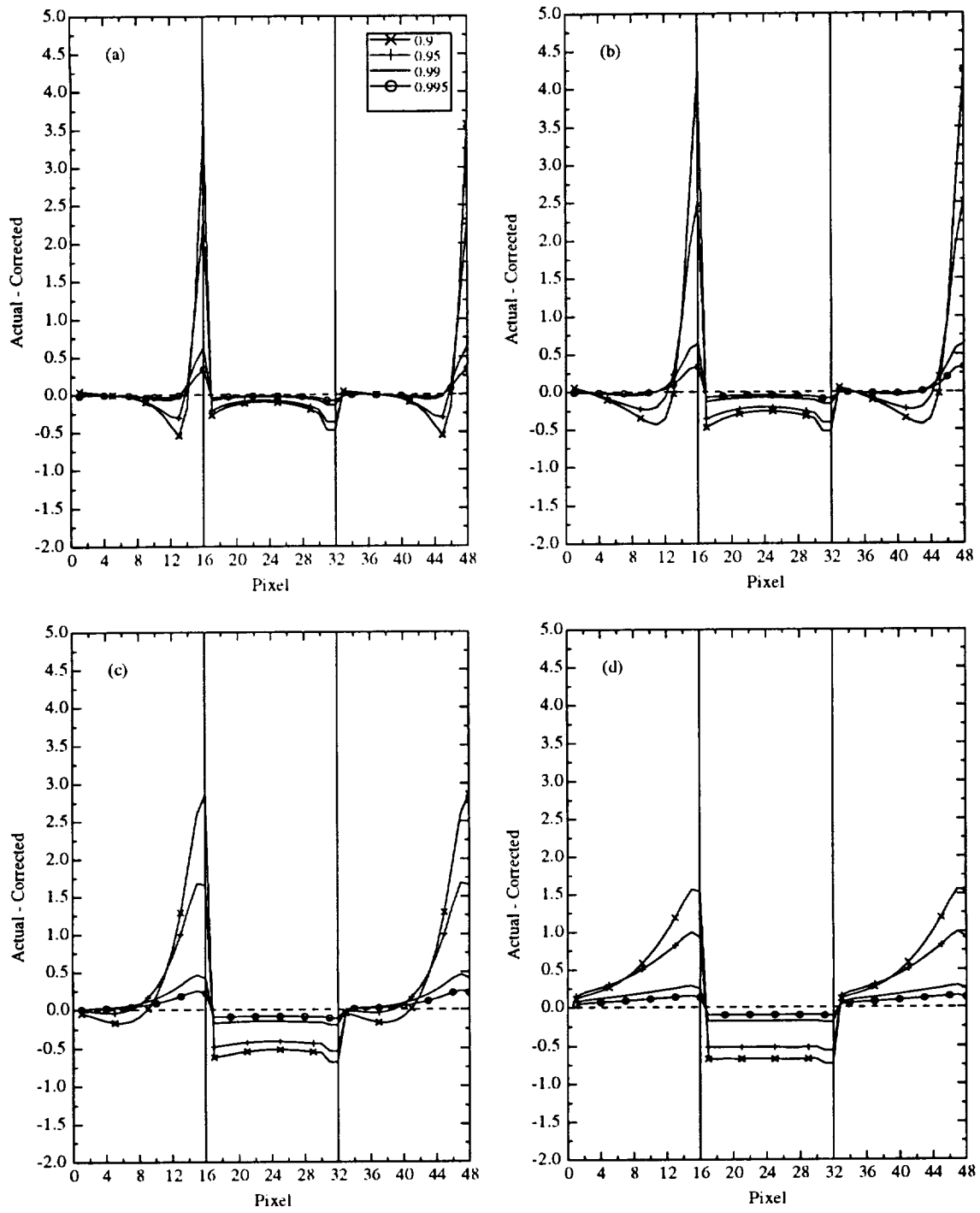
Figure 3.41 Same as Figure 3.38 except for a 50% cloud fraction.
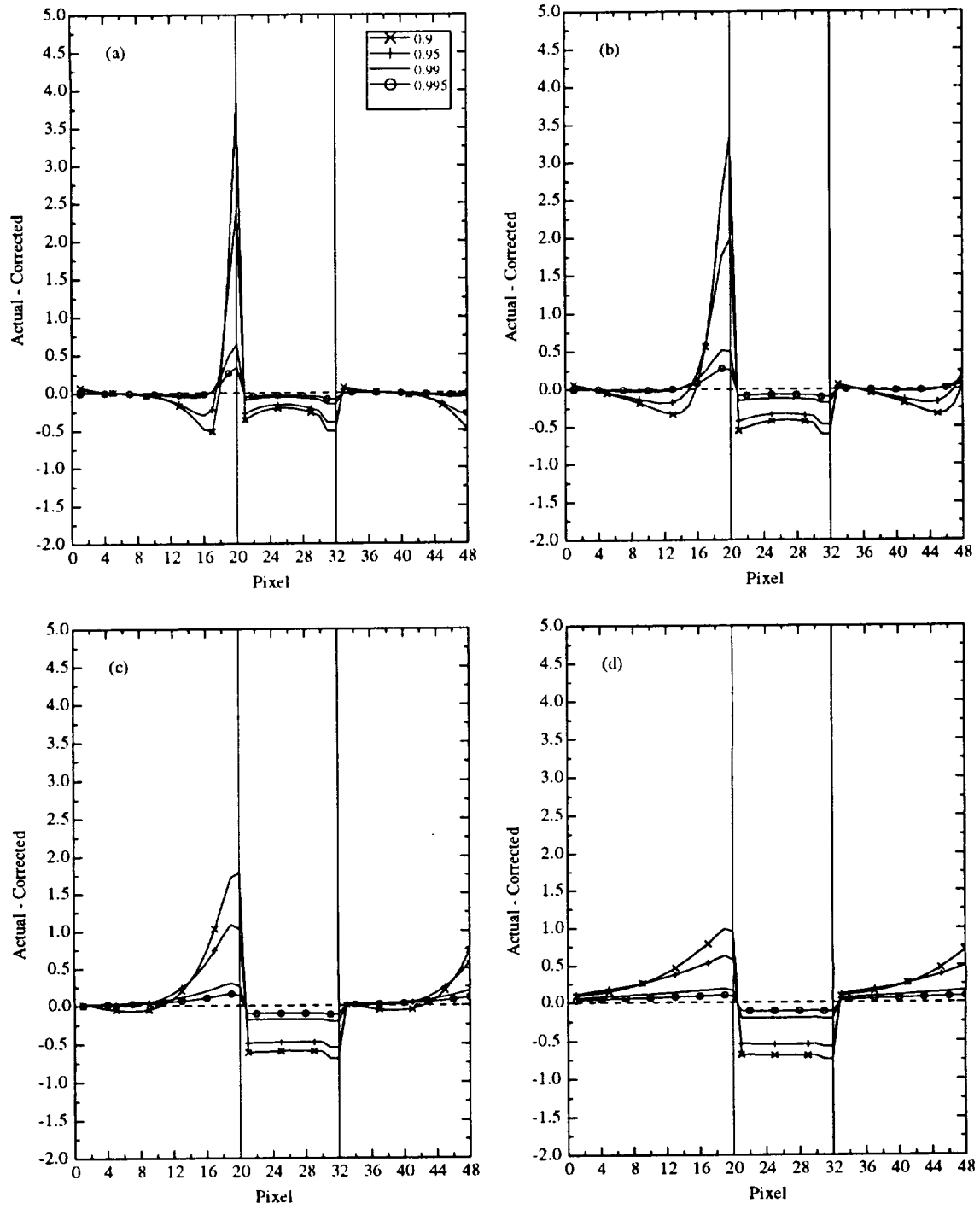
Figure 3.42 Same as Figure 3.38 except for a 62.5% cloud fraction.
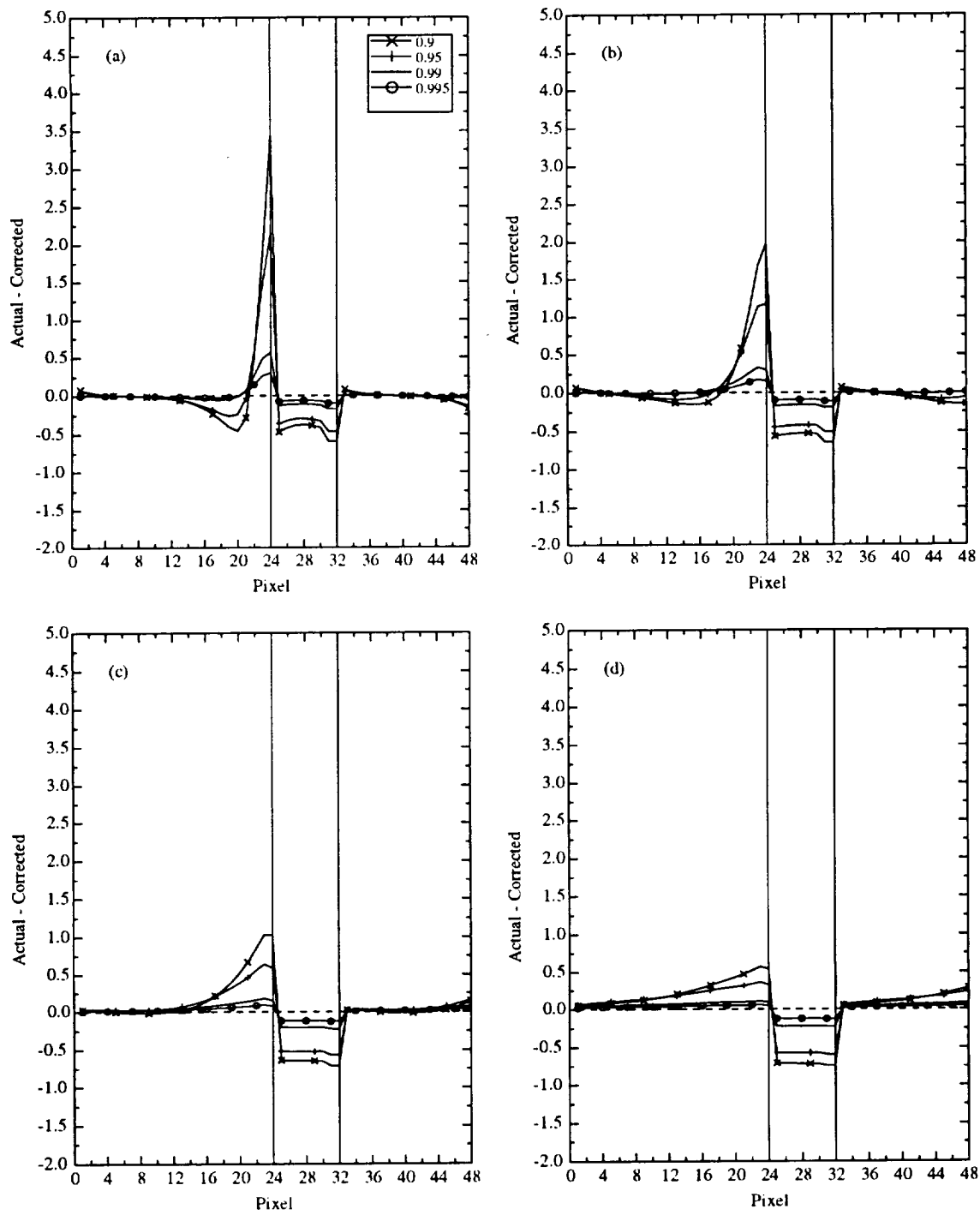
Figure 3.43 Same as Figure 3.38 except for a 75% cloud fraction.
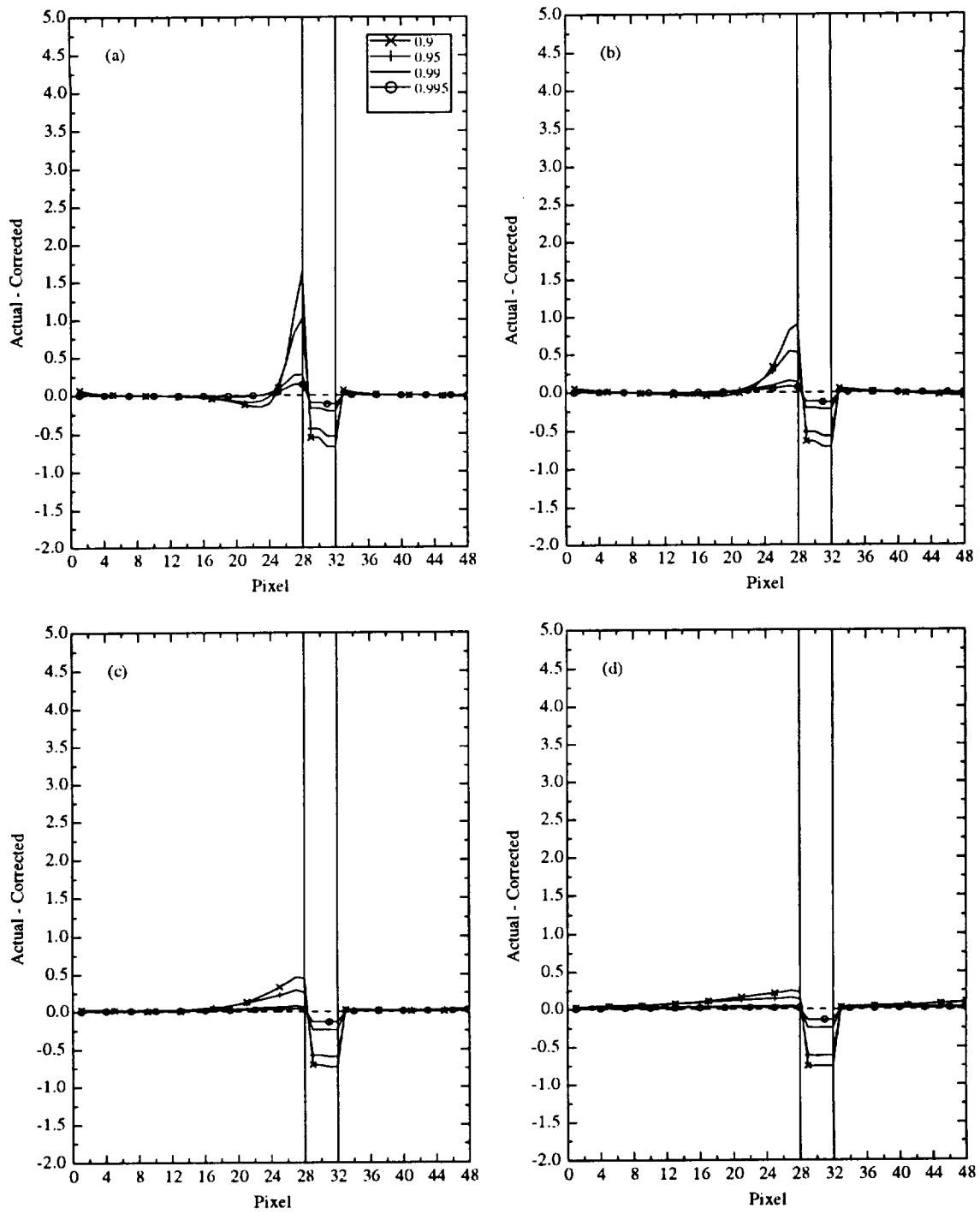
Figure 3.44 Same as Figure 3.38 except for a 87.5% cloud fraction.
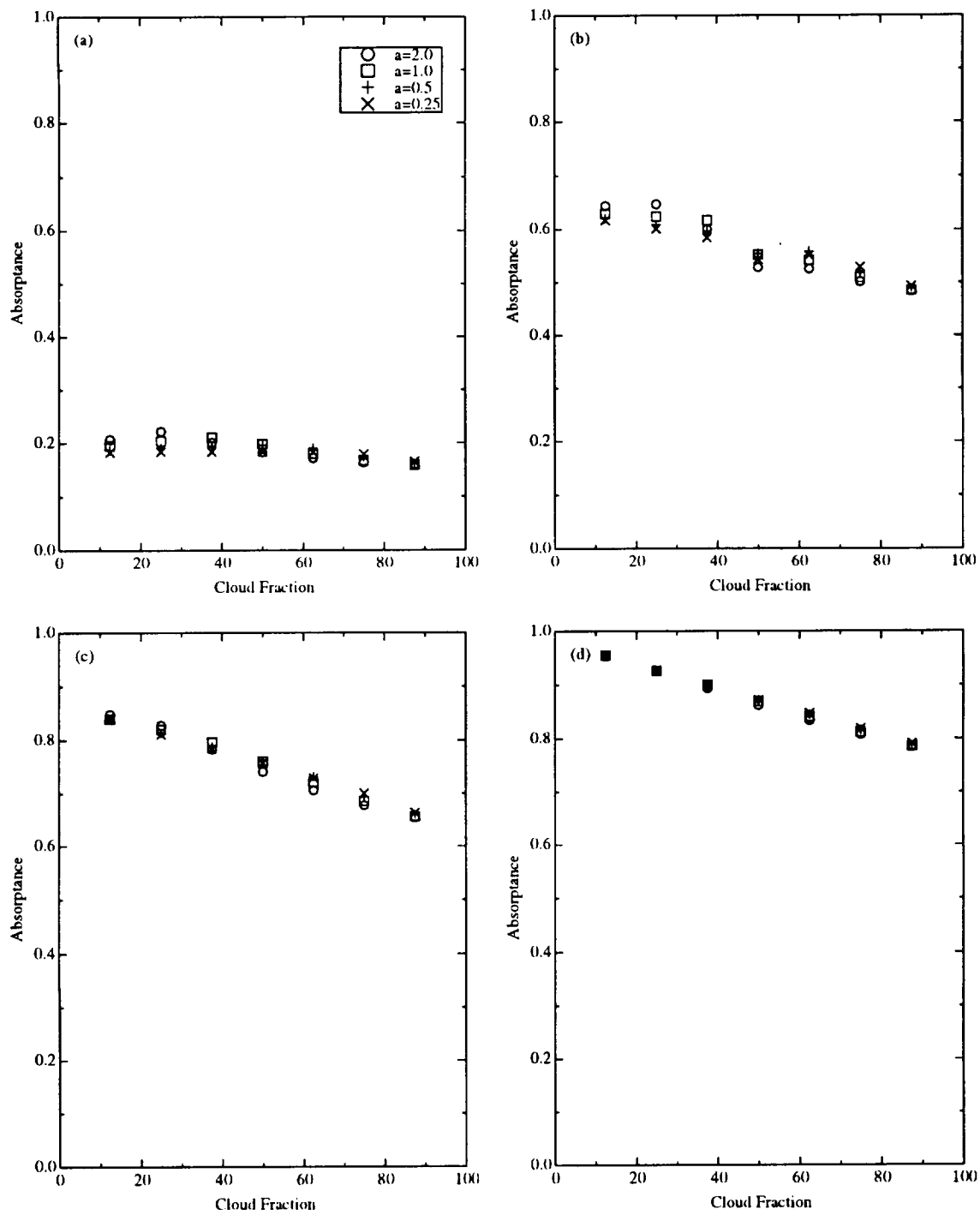
Figure 3.45 System absorptance for conservative droplet scattering for different vapor absorption, which yields ϖ of (a) 0.995, (b) 0.976, (c) 0.952, and (d) 0.909 in the cloudy portion.
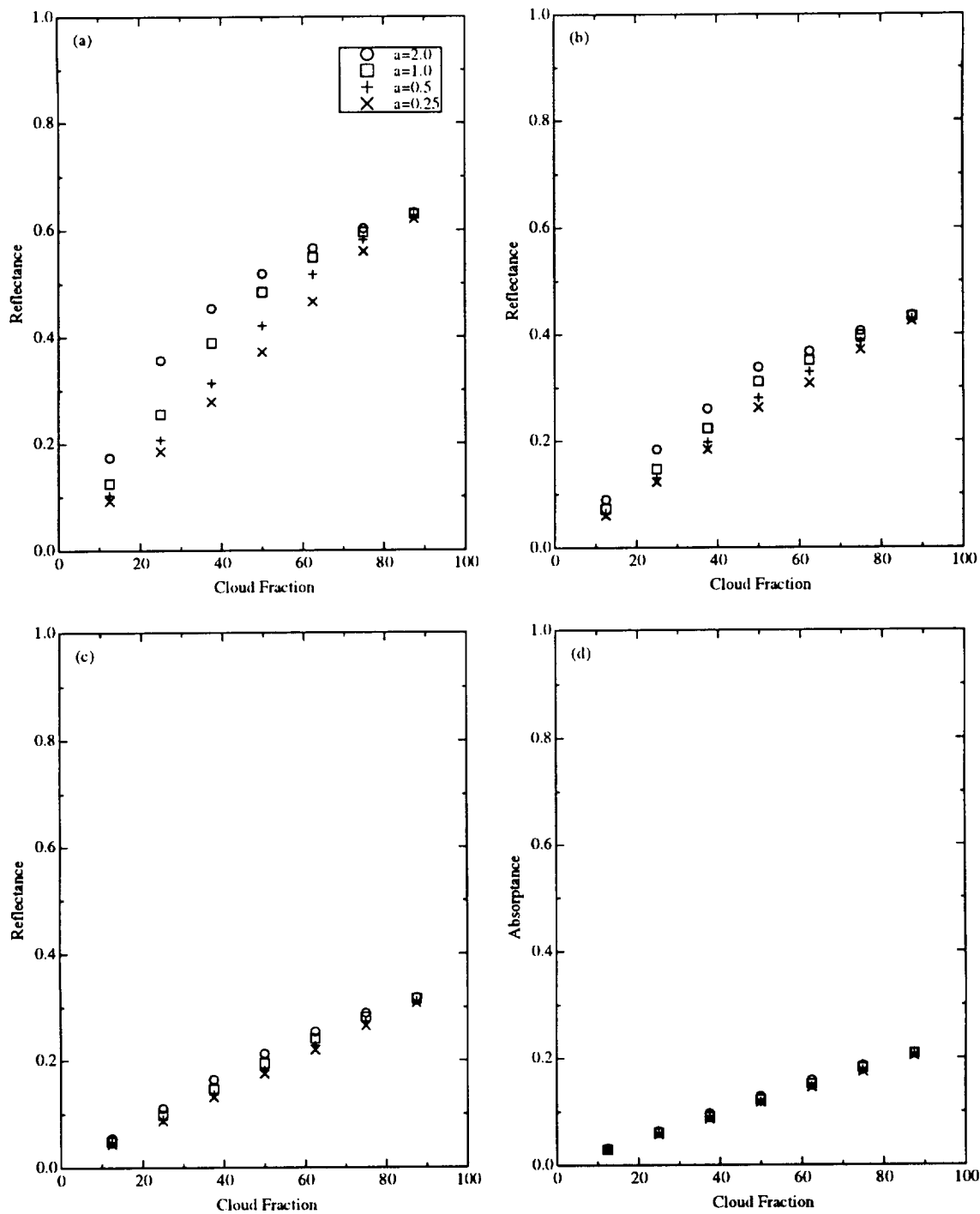
Figure 3.46 System reflectance for conservative droplet scattering for different vapor absorption, which yields ω of (a) 0.995, (b) 0.976, (c) 0.952, and (d) 0.909 in the cloudy portion.
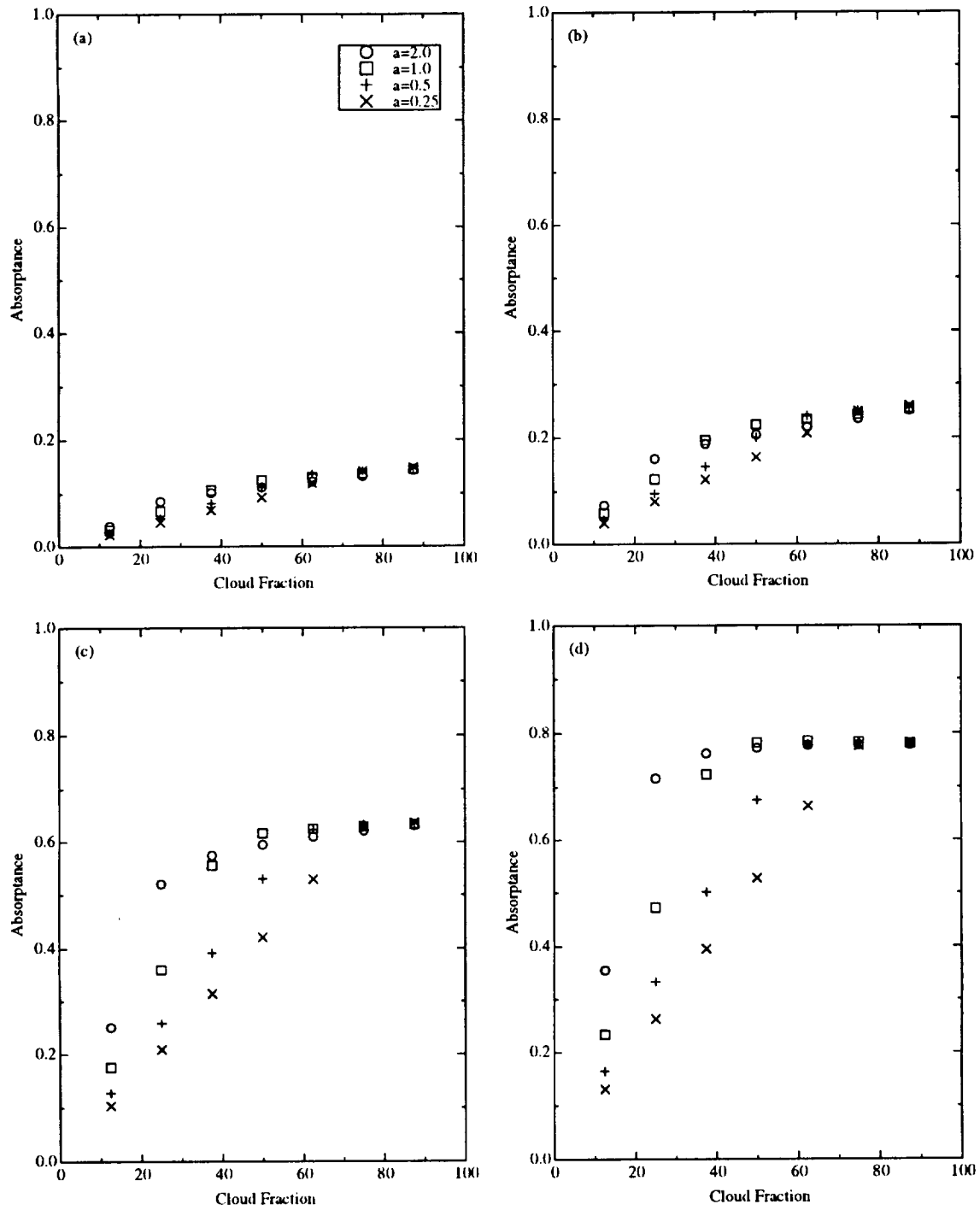
Figure 3.47 System absorptance for zero vapor absorption and ϖ of (a) 0.995, (b) 0.99, (c) 0.95, and (d) 0.9 in the cloudy portion.
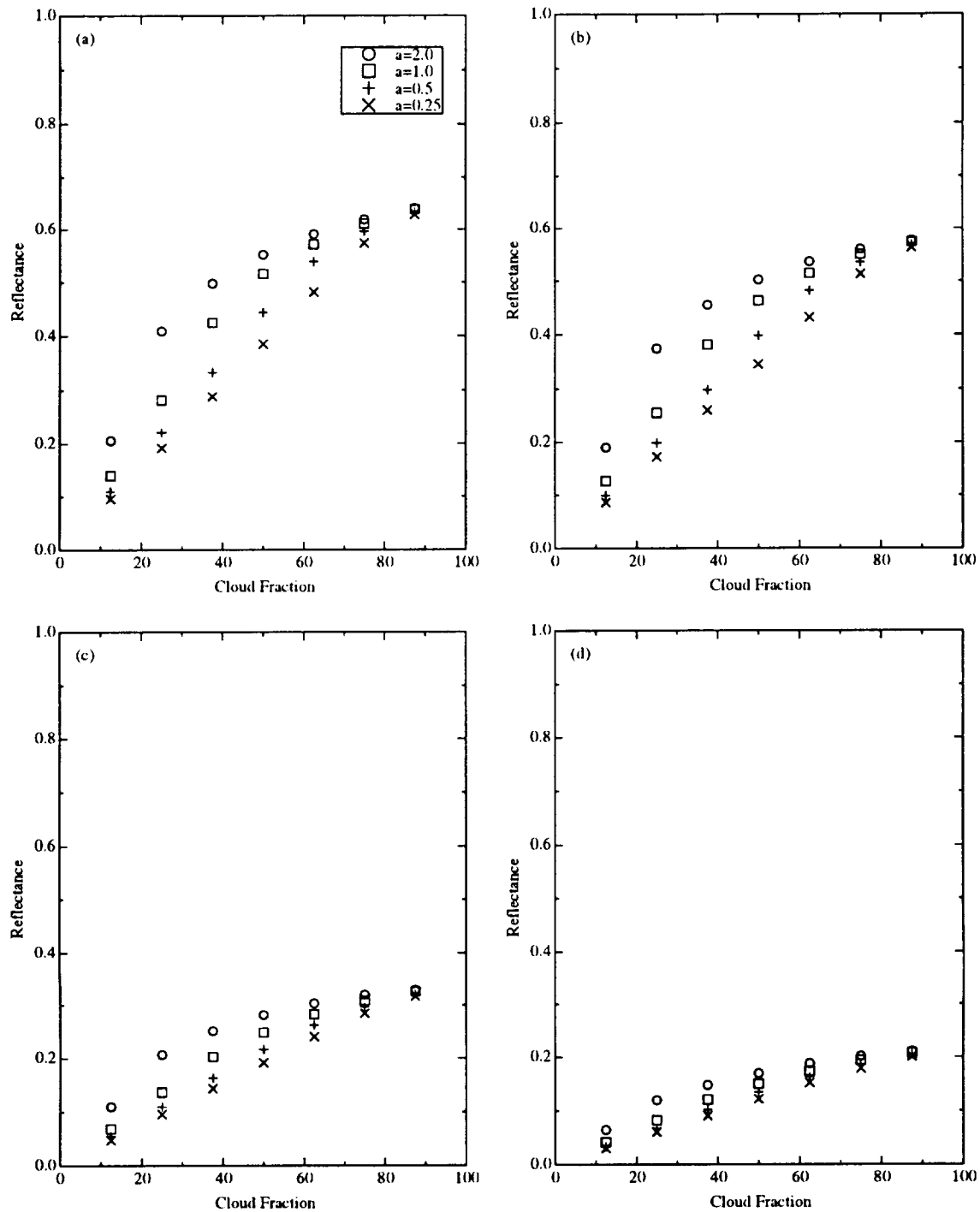
Figure 3.48 System reflectance for zero vapor absorption and ϖ of (a) 0.995, (b) 0.99, (c) 0.95, and (d) 0.9 in the cloudy portion.

CHAPTER 4. LIQUID WATER CONTENT DATA SET

One of the greatest problems with cloud models has been considering them as plane-parallel. Real data sets give the opportunity to study clouds as they really are, inhomogeneous. The data sets are an asset by lending a better understanding of a cloud's structure and how a cloud can interact with radiation. This can help in the long term by more realistic cloud models in the end result. The data set that was used in this study is a one dimensional liquid water content (LWC) data set of marine stratocumulus clouds taken by a PVM-100A probe on board a C-131A aircraft (Gerber et. al., 1994) during the Atlantic Stratocumulus Experiment (ASTEX) project.

1. Description of the ASTEX project

The Atlantic Stratocumulus Experiment (ASTEX) project was held in the north eastern part of the Atlantic Ocean from June 1 to the 28th of 1992. The project was conducted over a region that includes the Azores, Madeira and Canary Islands, these islands can be found off the coast of North Africa and Spain.

The goal of the ASTEX project was to study the physical and meteorological properties of marine stratocumulus and cumulus clouds. This study was created to look at clouds in many different ways, where one approach was to make improvements on dynamical, radiative, and microphysical models. Also the study hoped to improve the understanding of how aerosols, cloud microphysics and chemistry impact upon the properties of the whole cloud in order to develop better parameterizations for GCMs and climate models. ASTEX also provided information to develop and test algorithms used by satellites for retrieving cloud properties.

The ASTEX project was conducted by several different government agencies but was not limited to the United States; several countries were also involved in the project. The activities were run by the Office of Naval Research, and was strongly supported by NASA. Other agencies that were involved were the National Science Foundation, the Department of Energy, and the National Oceanic and Atmospheric Administration. The countries that were involved were the United Kingdom, France, Germany, Portugal, Netherlands, Russia, and Spain. Altogether there were over 200 people involved in the project.

The data collected during the project utilized many different platforms. The platforms ranged from such things as ground and ship based instruments as well as instruments on board aircraft, and satellite measurements. The satellites and aircraft that flew in the upper atmosphere collected data that would be used to study clouds on a large-scale. The aircraft that flew in the lower levels and the boundary layer collected information on the turbulence and the smaller-scale properties of the cloud. Ship based instruments made measurements at the surface as well as looking at the upper-air. Also the ships along with the instruments placed on the islands were able to provide the meteorological conditions and radiative fluxes at the surfaces, and data on the temperatures, moisture and winds of the upper-air. The ship and ground based platforms also were able to provide information of the cloud properties at high temporal resolutions.

This study, in particular, used the liquid water content data that was collected by the PVM-100A. The PVM-100A, along with many other instruments, were flown onboard a C-131A aircraft that was operated by the University of Washington. The University of Washington's goal was to collect data for study of cloud physics and aerosols.

2. PVM-100A

The PVM-100A is a relatively new microphysical sensor used to measure the liquid water content (LWC) and the total particle surface area (PSA) of cloud droplets, designed for the use on aircraft (Gerber, 1992). The technique used to make these

measurements is similar to a technique described by Wertheimer and Wilcock (1976). Also the PVM-100A can provide the effective droplet radius, r_e, from the relationship $r_e \propto LWC/PSA$ (Gerber et. al., 1994).

The description of the PVM-100A and how it works will follow Gerber et. al. (1994). A more detailed look at the instrument can be found in Gerber (1991, 1992) and Gerber et. al. (1994).

The PVM-100A is similar to the PVM-100, which is used to make ground-based measurements of LWC (Gerber, 1991). The two instruments are similar in how they make measurements, but are different in where they are used. The PVM-100A is designed to be mounted on the outside of an aircraft, and is able to make in situ measurements of cloud LWC and PSA. Unlike other instruments that are used to determine LWC the PVM-100A and PVM-100 are not dependent on how fast the droplets pass through the detector. The instruments, instead, look at many droplets at the same time in a cloud volume.

The PVM-100A's probe contains a hollow sampling tube in which the cloud droplets will pass through as the plane is flying. A laser beam passes through this sampling tube where it interacts with a volume of the cloud droplets. The sampling volume is 1.25 cm^3. The information from the probe is split into two different channels and is then sent inside the aircraft to a set of electronics. The electronics then separates the light scattered by the droplets from the background light where the signal is scaled and a voltage is produced for LWC, PSA and r_e.

The process by which the PVM-100A interacts with the cloud droplets starts with a laser beam scattering light off cloud droplets in a given volume. Since cloud droplets scatter light into mainly the near-forward direction a lens is placed on the other side of the laser beam, which redirects the scattered beam from the droplets into a beam splitter. The beam splitter divides the scattered light into two equal portions that are then redirected into two different channels, one to measure LWC the other to measure PSA. The scattered light is then directed onto a variable-transmission filter and sensor for each channel. Each channel then derives the LWC and the PSA for that volume of cloud droplets.

The LWC is derived by the following equation:

$$LWC = \frac{4\pi\rho}{3} \int r^3 n(r) dr$$

where r is the cloud droplet radius, n(r) is the droplet size spectrum, and $\rho = 1.0$ g cm^{-3} is the droplet density.

3. PVM-100A LWC Data from ASTEX

The PVM-100A took LWC measurements during the ASTEX project in June 1992 while aboard the University of Washington's C-131A aircraft. It was mounted behind the nose of the aircraft and near other instruments designed to measure LWC, in part for comparison (Gerber et. al., 1994).

The C-131A had an average flight speed close to 80 ms^{-1} and the sampling rate of the data was 10 Hz, this implies that the resolution of the data is 8 m. The aircraft flew a total of 16 trips during ASTEX, on three of those trips no marine stratocumulus clouds were seen, therefore, there is no LWC data reported for those days with the PVM-100A.

The LWC data sets taken during the ASTEX project are represented in Figures 4.1 to 4.15. Each of the flight trips that the C-131A took were on individual days, so June 2, 1992 (Figure 4.1) was the first of the flights and it is numbered Flight 1557. The only days that do not have figures are the three days that there were no marine stratocumulus clouds. Within each of the flights there were individual retrievals, made of the LWC data. These retrievals are numbered consecutively throughout the ASTEX project. For example in Figure 4.1 for June 2, 1992 data was collected three times, therefore, the data sets for June 2, 1992 start the numbering at #1, #2, #3 (Figures 4.1, (a), (b), (c)), and so on. The numbering system skips over #14 and #30, as these were not included in the original data set. The data set #39 for June 22, 1992 was not included in the study due to a corrupted data file.

LWC is the amount of liquid water, in mass, that is present in a unit volume. The retrieved LWC data sets from the PVM-100A, in Figures 4.1 to 4.15, are given in terms of

g m^{-3}. Each of the data set of g m^{-3} is plotted against the distance in which the C-131A aircraft flew during the retrieval. The starting point of each of the retrievals will be considered to be at 0 km and extend to the point at which the last data point was taken, at or before 300 km. To eliminate errors due to possible noise in data segments that contained a small amount of liquid water, a limit of 0.02 g m^{-3} was placed on the LWC data. Therefore, any data point less than or equal to 0.02 g m^{-3} was considered to be zero. Gaps in the data then are considered to be clear, cloudless, areas that the C-131A passed through during its retrieval.

Each of the LWC data sets is similar to what would be expected from marine stratocumulus clouds. A comparison of the ASTEX LWC data sets from the PVM-100A was made with other LWC devices that were on board the C-131A, and the PVM-100A data sets were considered to be comparable if not better (Gerber et. al., 1994).

Figure 4.1 Liquid Water Content for flight tracks on June 2, 1992 (a) #1, (b) #2, (c) #3.
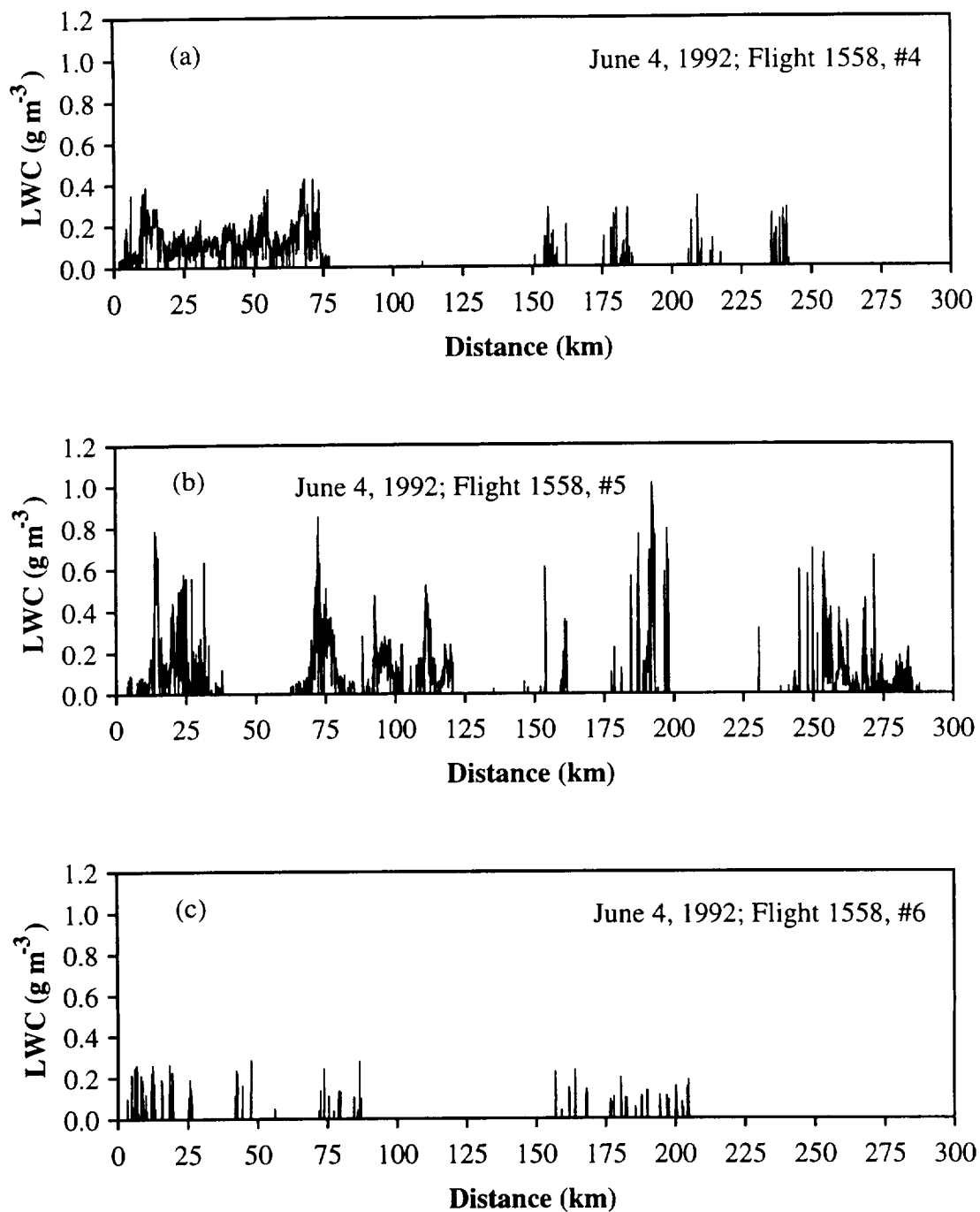
Figure 4.2 Liquid Water Content for flight tracks on June 4, 1992 (a) #4, (b) #5, (c) #6.
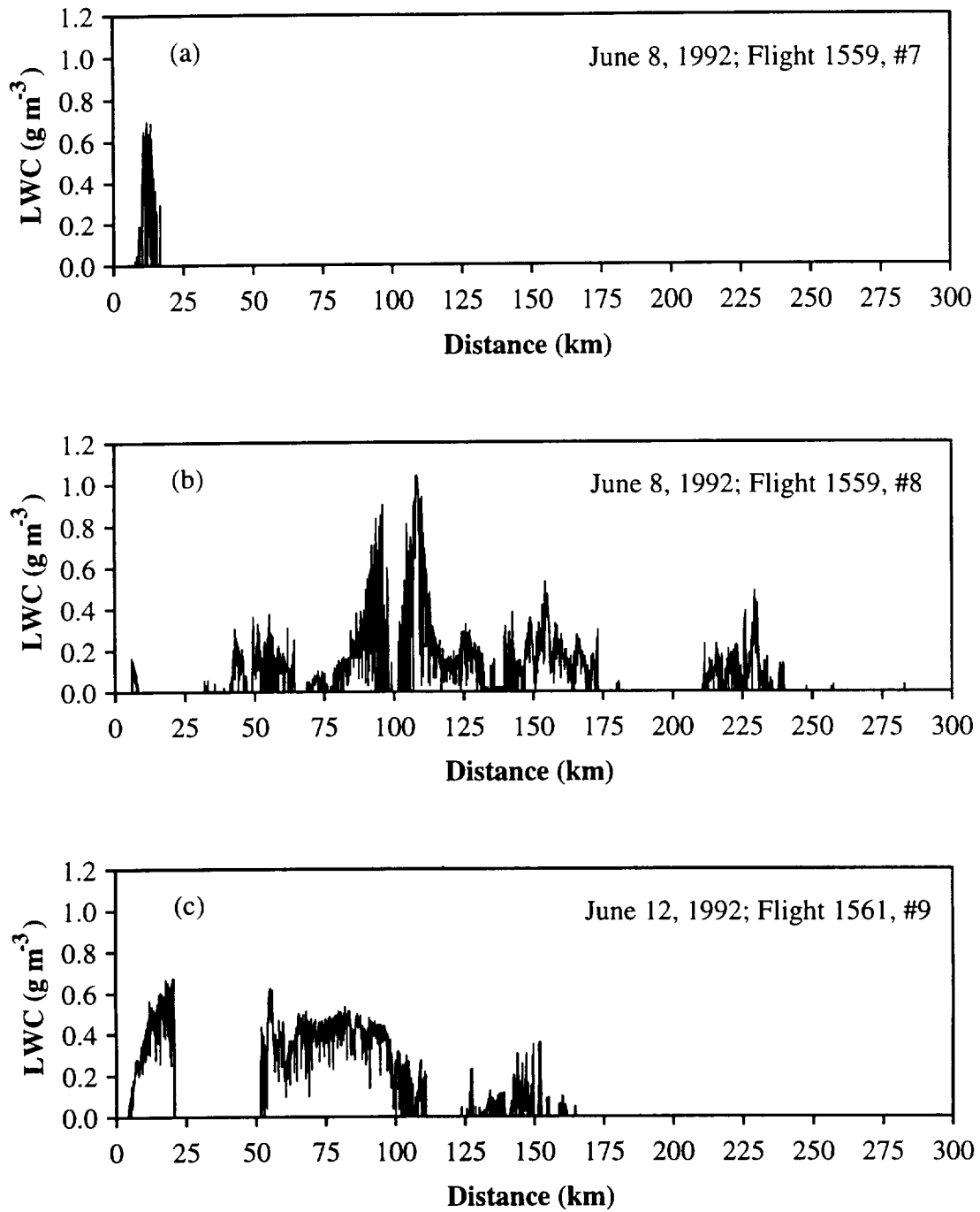
Figure 4.3 Liquid Water Content for flight tracks on June 8, 1992 (a) #7, (b) #8, and June 12, 1992 (c) #9.
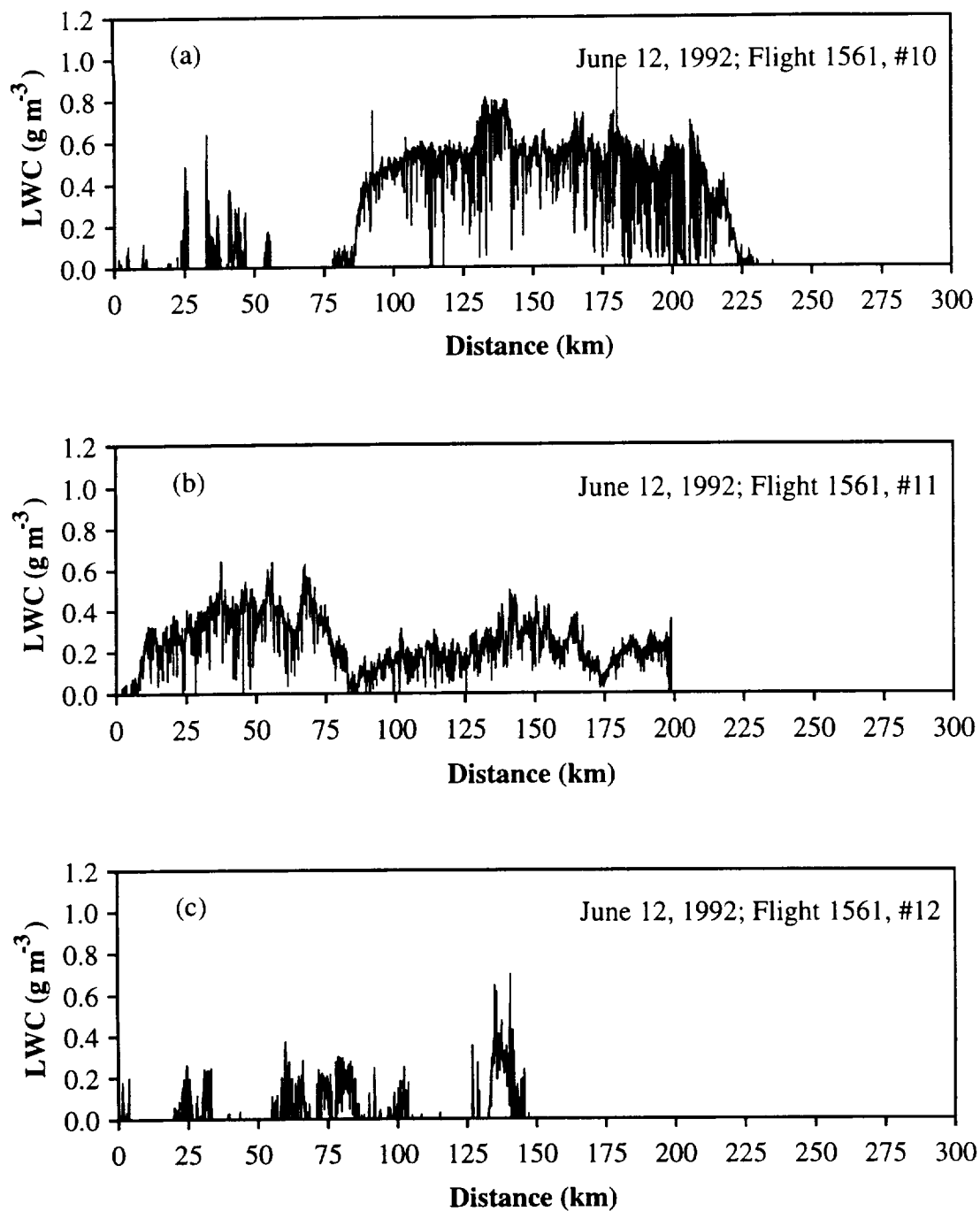
Figure 4.4 Liquid Water Content for flight tracks on June 12, 1992 (a) #10, (b) #11, (c) #12.
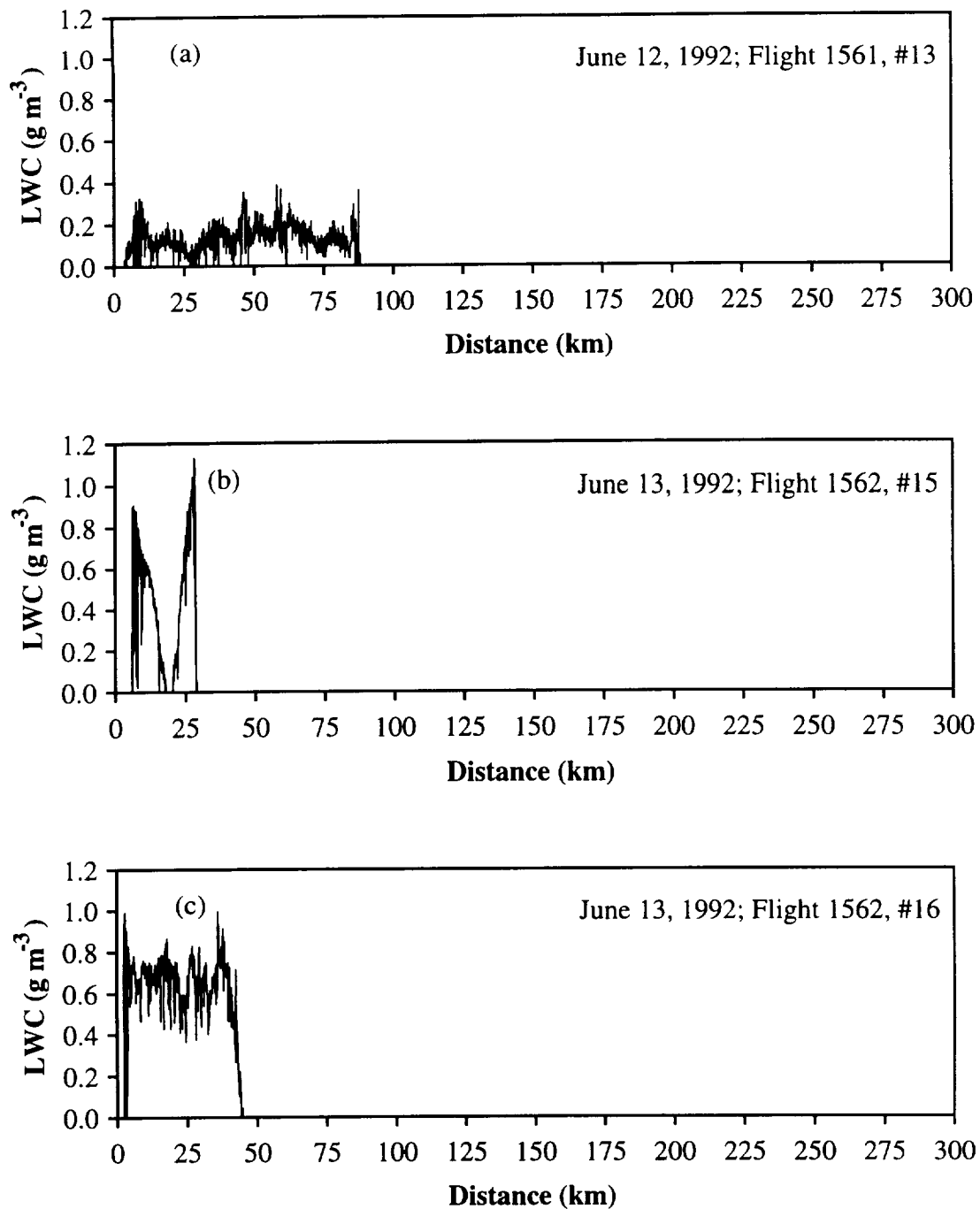
Figure 4.5 Liquid Water Content for flight tracks on June 12, 1992 (a) #13, and June 13, 1992 (b) #15 (c) #16.
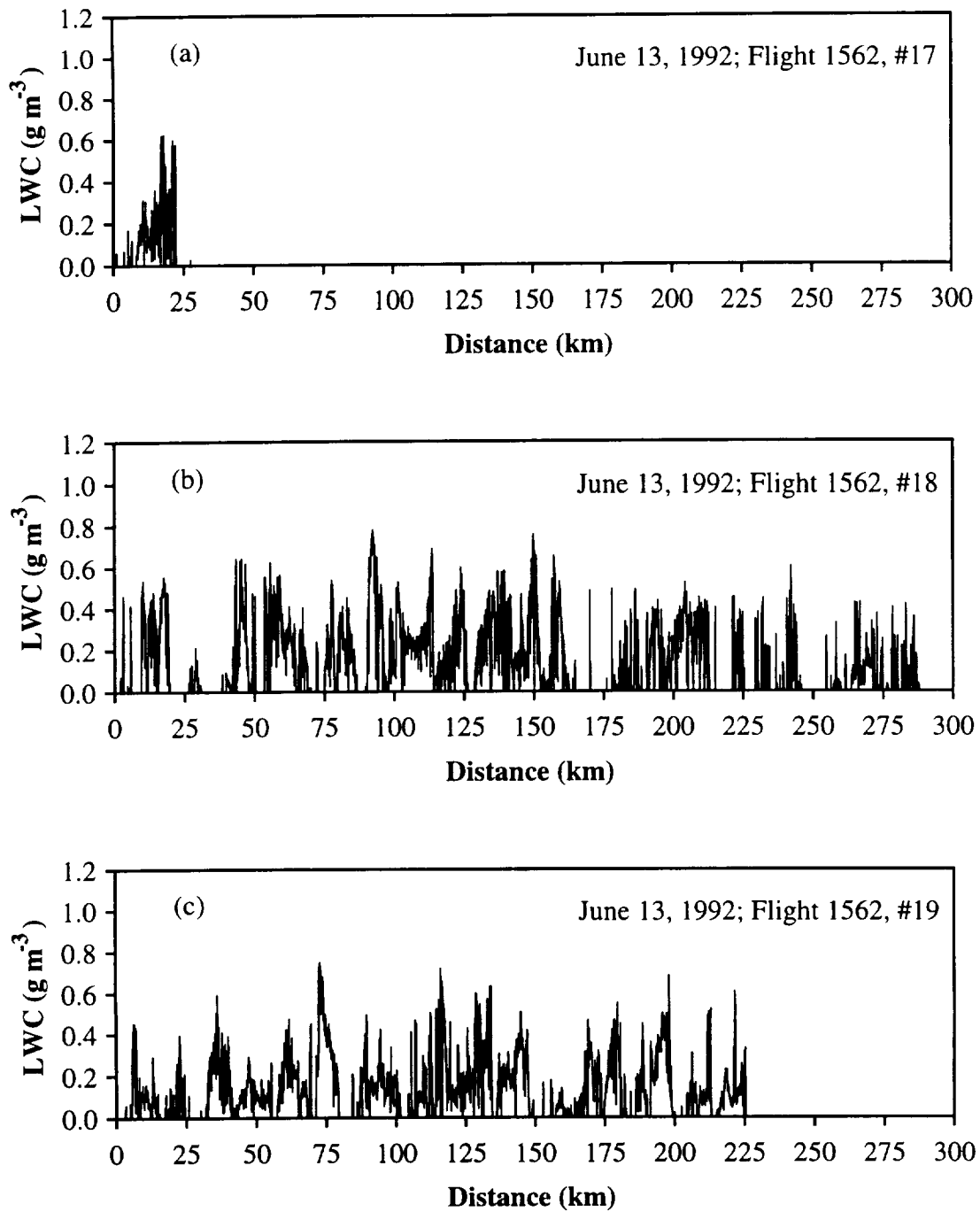
Figure 4.6 Liquid Water Content for flight tracks on June 13, 1992 (a) #17, (b) #18, (c) #19.
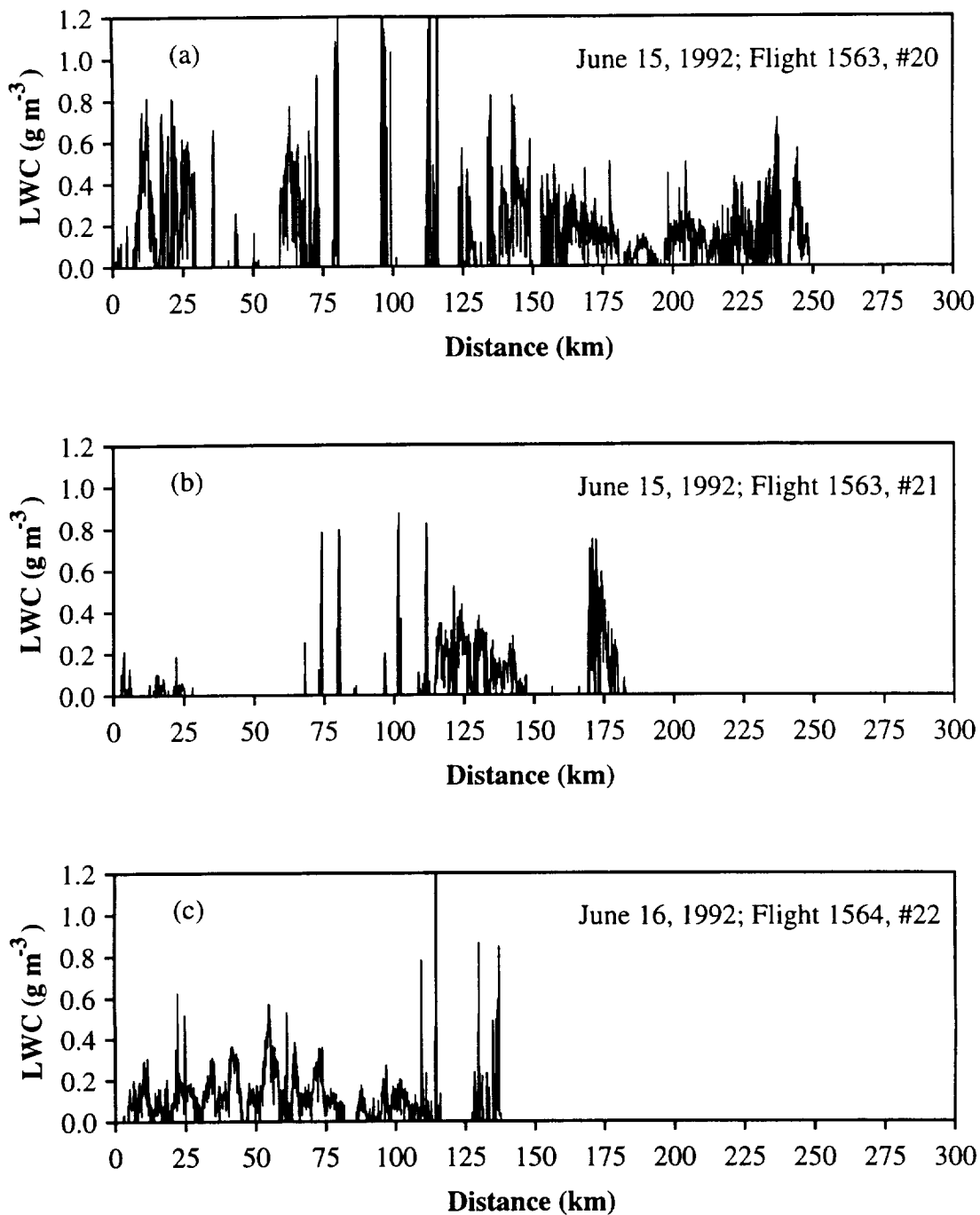
Figure 4.7 Liquid Water Content for flight tracks on June 15, 1992 (a) #20, (b) #21, and June 16, 1992 (c) #22.
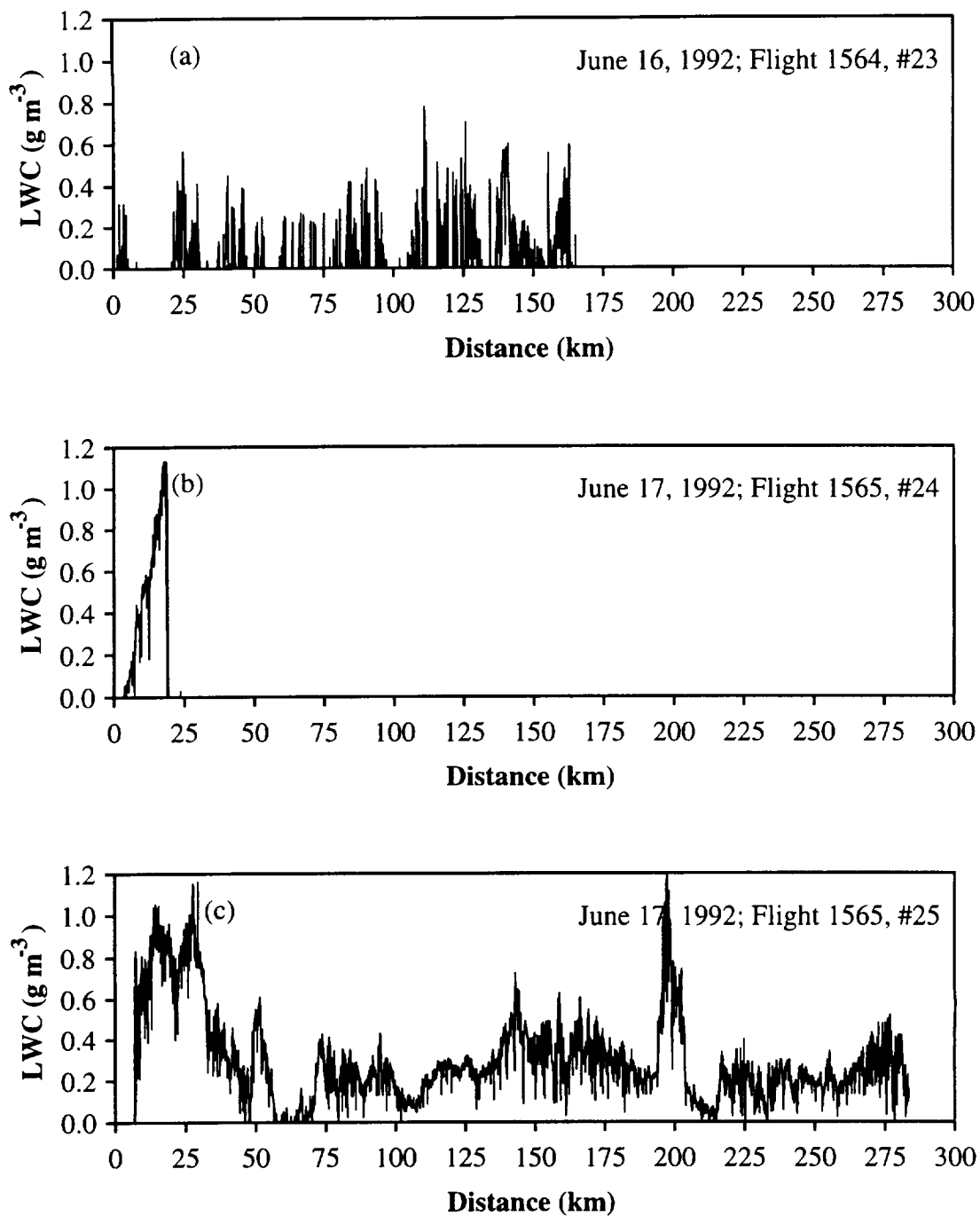
Figure 4.8 Liquid Water Content for flight tracks on June 16, 1992 (a) #23, and June 17, 1992 (b) #24, (c) #25
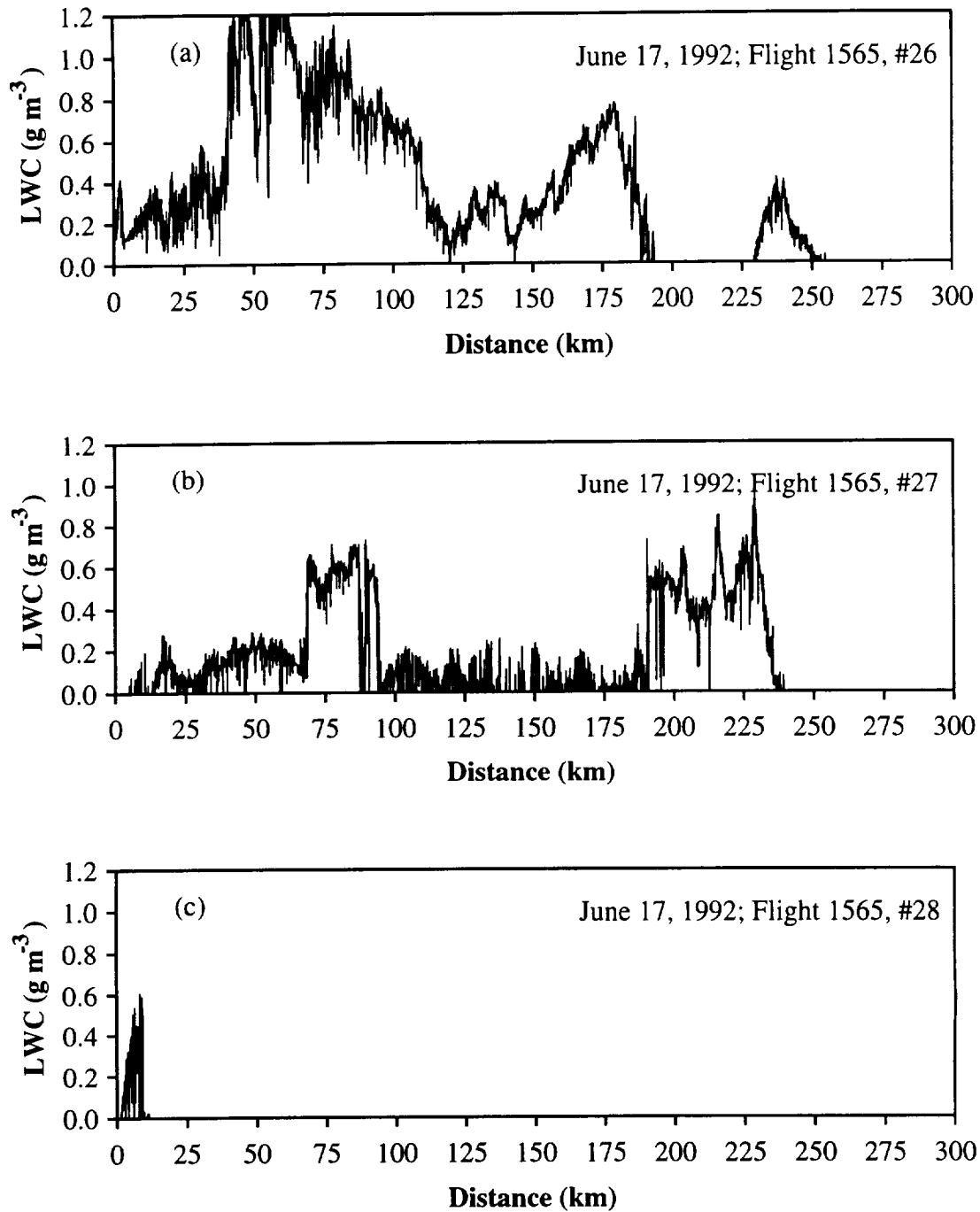
Figure 4.9 Liquid Water Content for flight tracks on June 17, 1992 (a) #26, (b) #27, (c) #28.
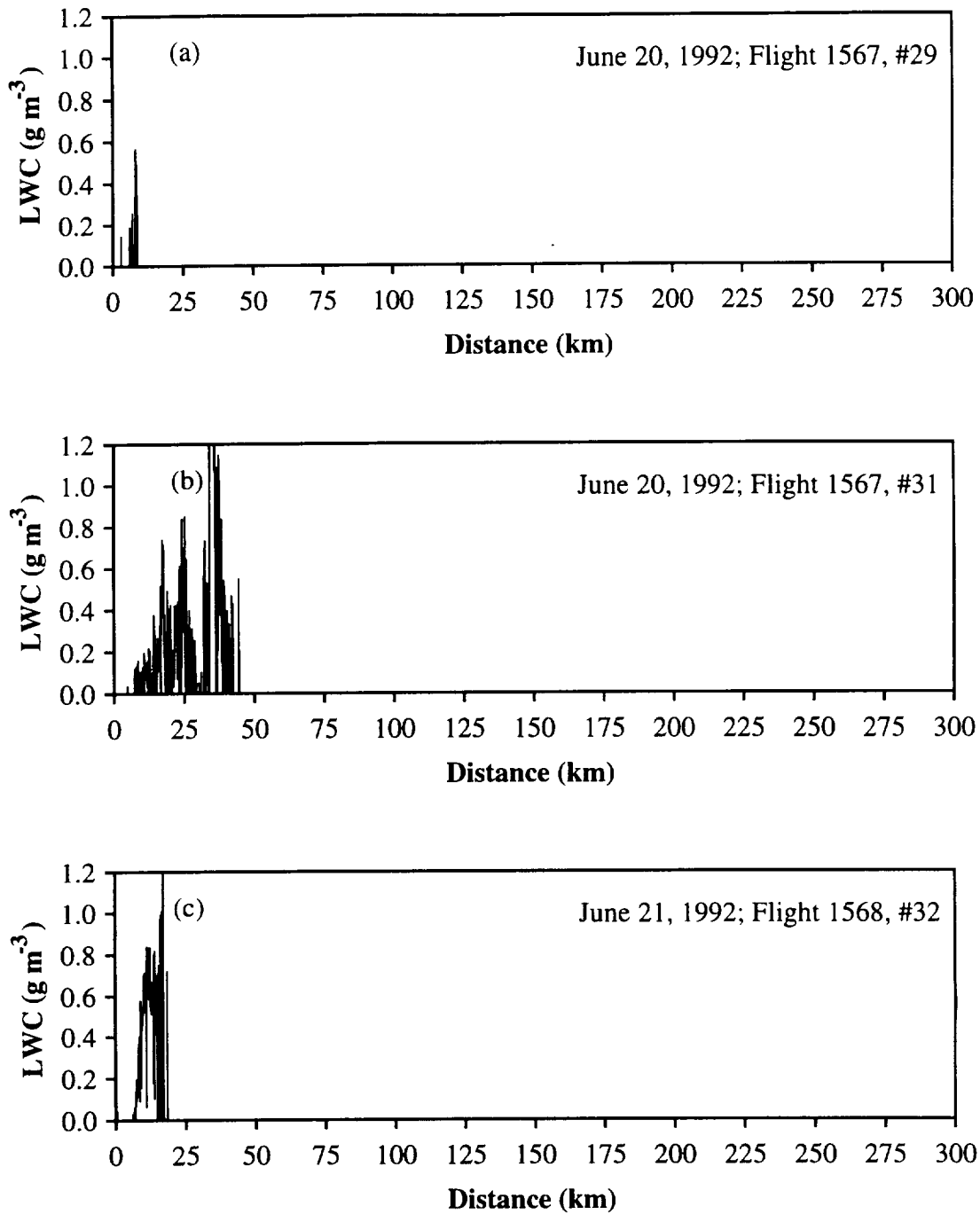
Figure 4.10 Liquid Water Content for flight tracks on June 20, 1992 (a) #29, (b) #31 and June 21, 1992 (c) #32.
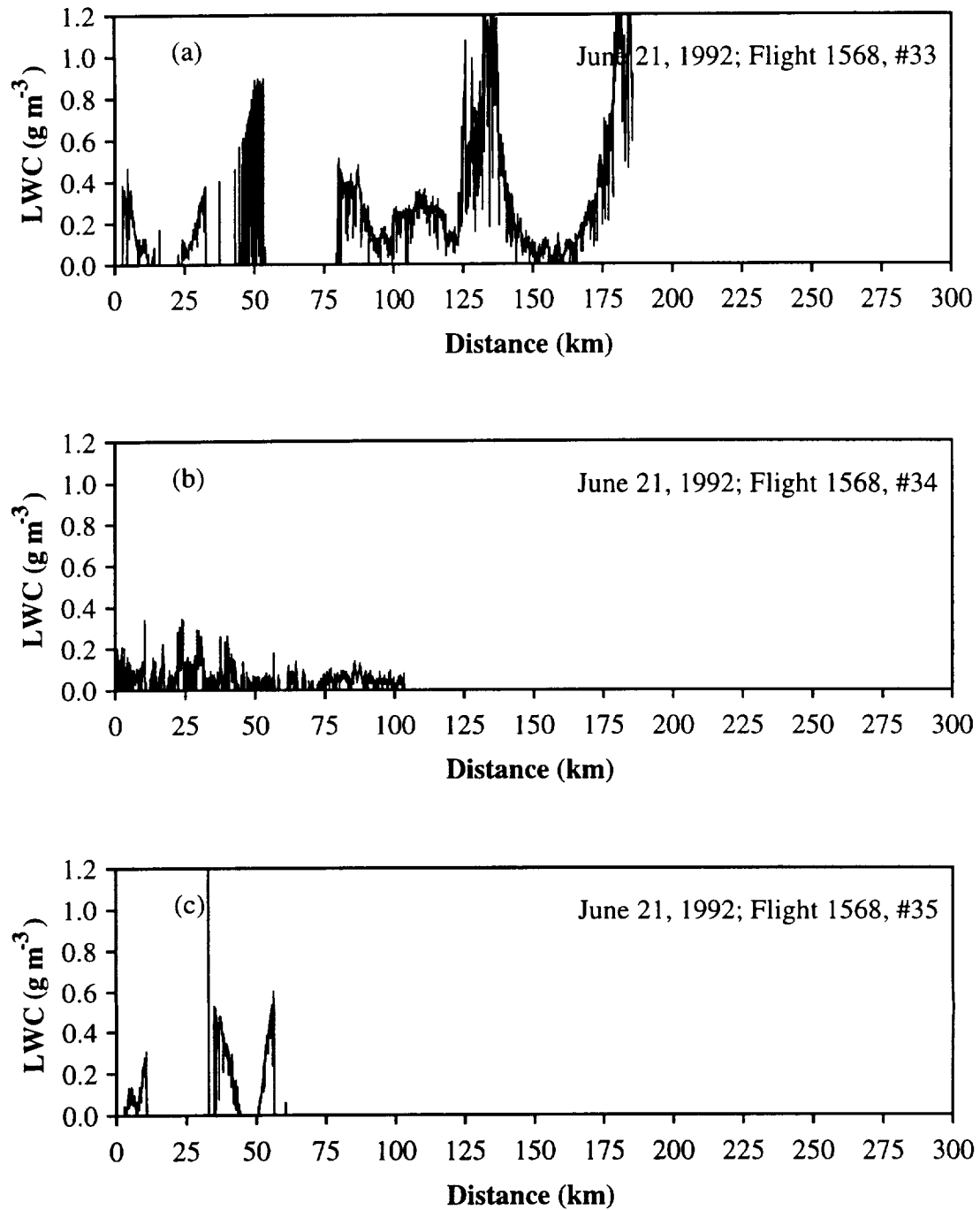
Figure 4.11 Liquid Water Content for flight tracks on June 21, 1992 (a) #33, (b) #34, (c) #35.
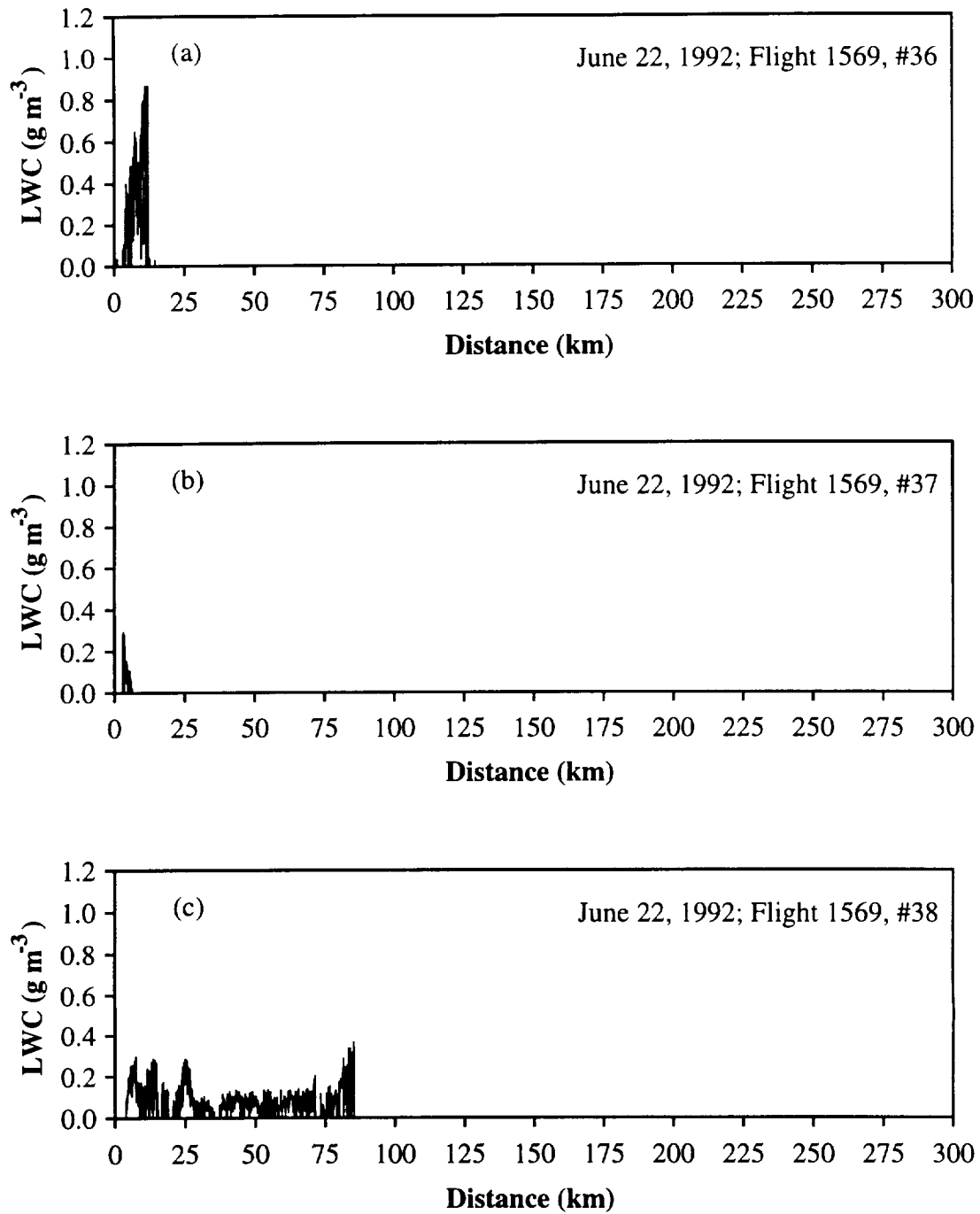
Figure 4.12 Liquid Water Content for flight tracks on June 22, 1992 (a) #36, (b) #37, (c) #38.
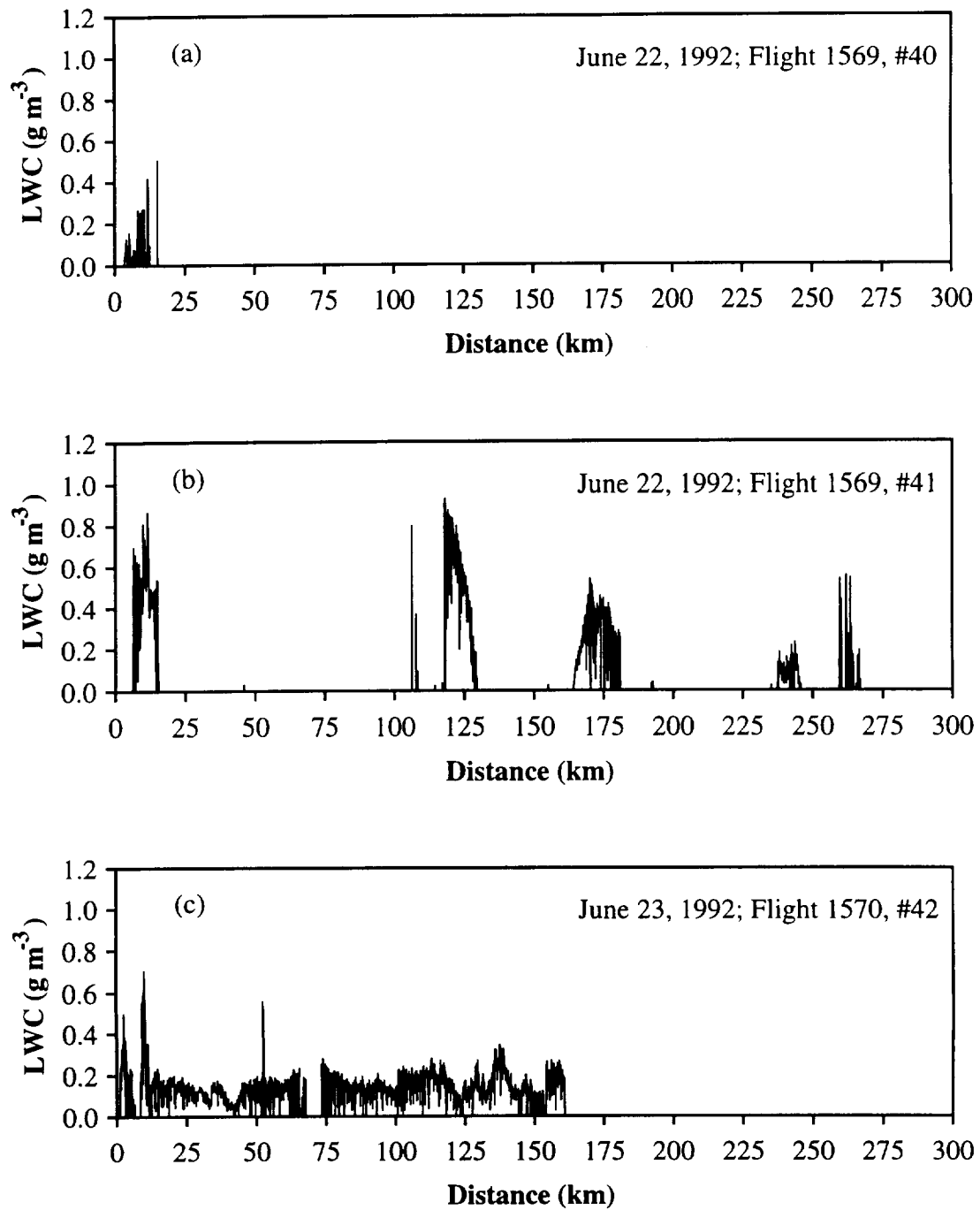
Figure 4.13 Liquid Water Content for flight tracks on June 22, 1992 (a) #40, (b) #41, and June 23, 1992 (c) #42.
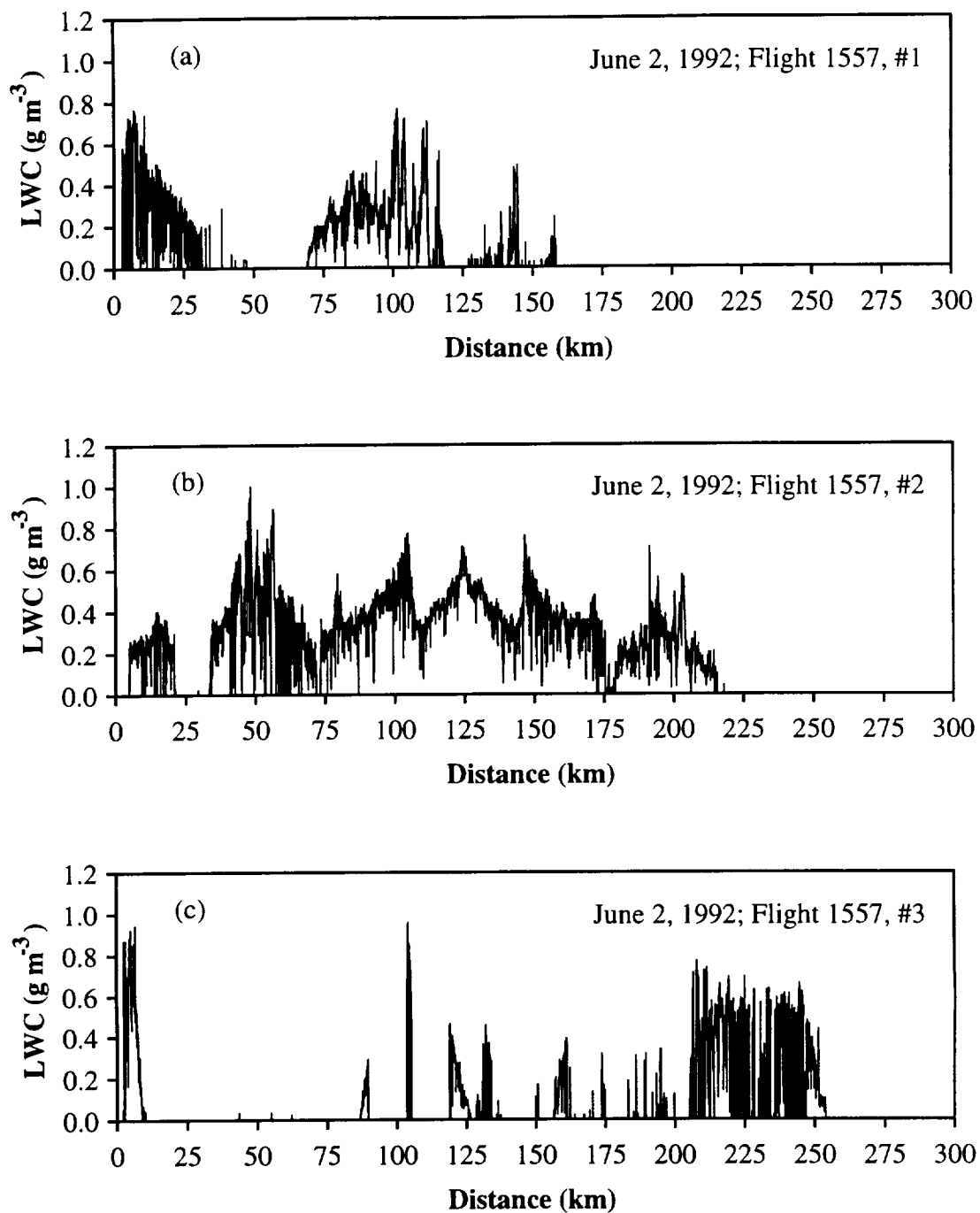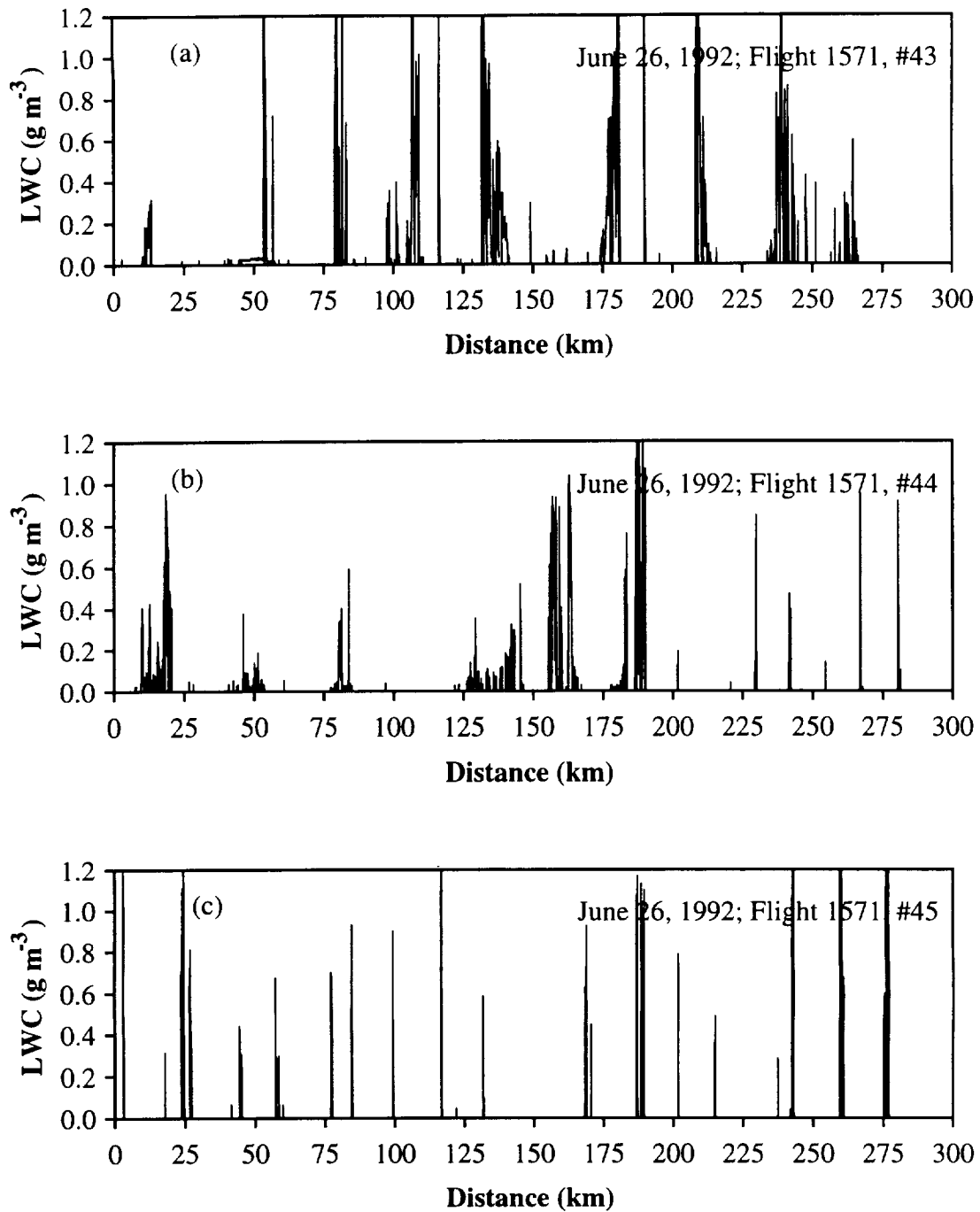
Figure 4.14 Liquid Water Content for flight tracks on June 26, 1992 (a) #43, (b) #44, (c) #45.
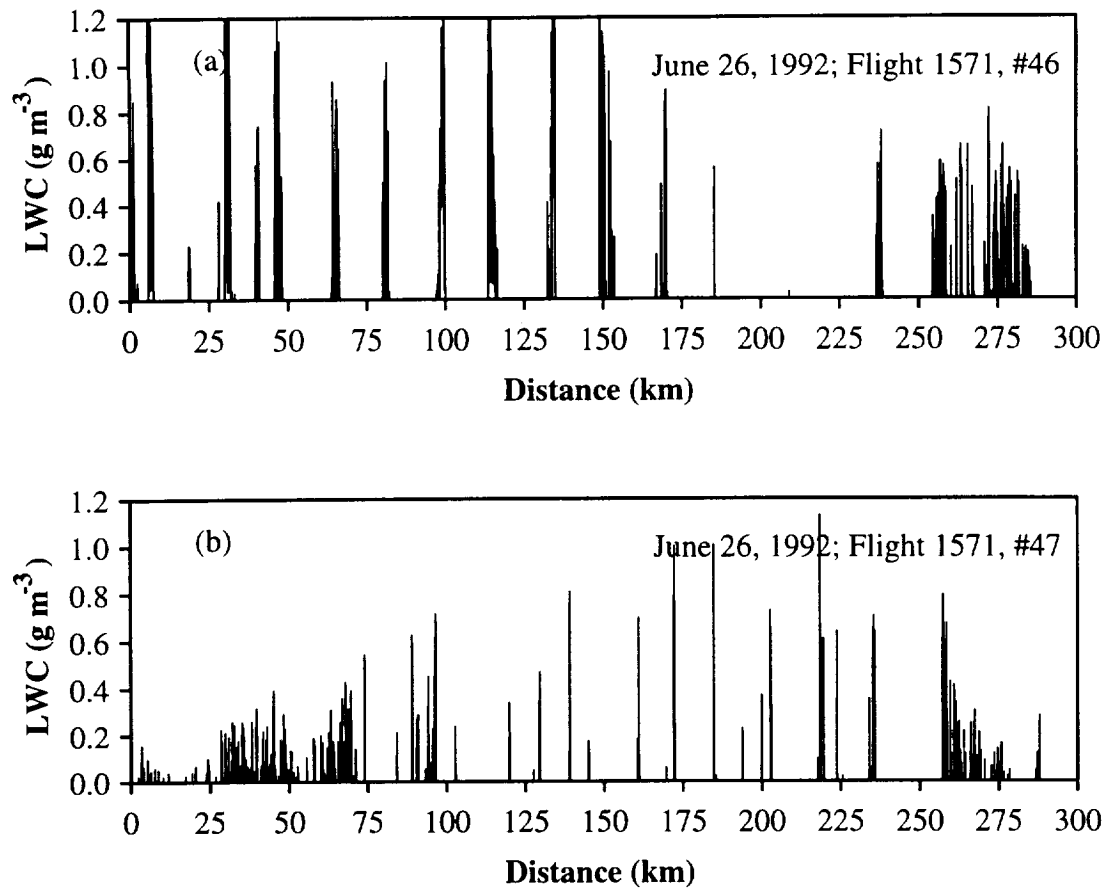
Figure 4.15 Liquid Water Content for flight tracks on June 26, 1992 (a) #46, (b) #47.

CHAPTER 5. DESCRIPTION OF WAVELET ANALYSIS

Data analysis is one of the most difficult and challenging parts of the process that comes with any data set. Choosing the right type of analysis can be difficult, but many times the kind of analysis desired will help in choosing the right technique. For many years the technique used for analyzing the frequency spectrum of a data set has been the Fourier transform. The Fourier transform is useful when looking at frequencies across the whole signal, but it can not provide a time localization in the data. To remedy the time localization a windowed Fourier transform can be used. The problem with this is that the window in a Fourier transform is defined over a fixed time period. This can cause an overrepresentation of the higher frequencies and an underrepresentation of the lower frequencies (Lau and Weng, 1995). A fairly new technique called wavelet analysis tries to solve this problem by using a window that can be stretched or compressed in time. In order to give an introduction into the wavelet transform a history and background of the wavelet transform will be given. A discussion of the mathematical theory along with some wavelet examples will follow.

1. History and Background

Wavelet analysis is a relatively new tool for analyzing the spectral nature of a signal at different resolutions. The theory of looking at a signal at different time scales, or frequencies, to analyze the spectrum at different resolutions has existed in different forms since the early 1900s (Rioul and Vetterli, 1991), but it never was combined into one technique. It was not until the early 1980s that wavelets were developed into a unified analysis tool by French geophysicists. They used strong mathematical foundations to support the subject and called it "Ondelettes", or Wavelets (Morlet et al., 1982a,b;

Grossmann and Morlet, 1984). Since the first introduction of wavelet theory there has been an increase in the interest and contribution toward its study and application. Some of the most influential contributors to the theory have been Mallat (1989) who played a key role in the use of multiresolution analysis with wavelet analysis, and Daubechies (1992) who developed some fundamental orthogonal wavelets.

The application of wavelet analysis has become very diverse among almost all fields of science. Many of these include image processing, image compression, optics, analysis of turbulence, chaos, fractals, time series analysis and even medical research to name a few.

-10   -5   0   5   10
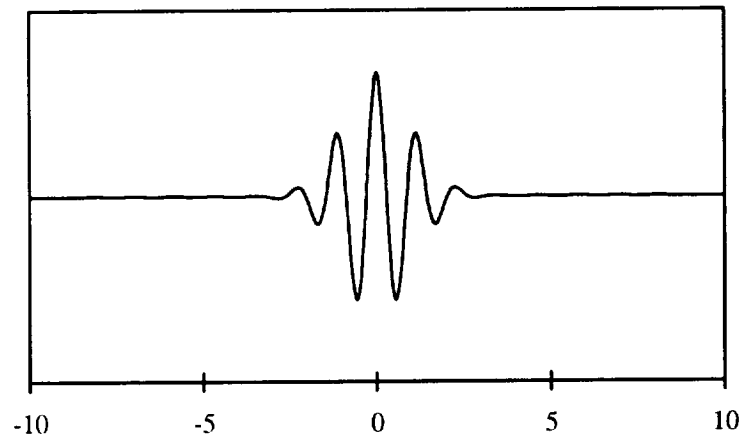
Figure 5.1 Example of a wavelet whose amplitude dampens off toward zero. Real part of the Morlet wavelet.

A wavelet is not like a sine or cosine wave, which has a constant amplitude, but instead is a wave that starts out with wave characteristics and whose amplitude dampens or dies off toward zero, as can be seen in Figure 5.1. This dampening of the amplitude of the wave gives the windowing effect that is seen in windowed Fourier transforms. The difference comes in how wavelets examine the different frequencies. Instead of defining a window that is constant in time where the analyzing wave's frequency changes inside the window, wavelet analysis changes the size of the window in order to keep resolution in both time and frequency. Due to the uncertainty principle (Chui, 1992) there is a trade off between the time and the frequency. The time resolution becomes arbitrarily good at high

frequencies at the expense of the frequency resolution, while the frequency resolution becomes arbitrarily good at the lower frequencies due to the expense of the time resolution (Figure 5.2). The resizing of the wavelet window, by stretching and compressing, is generalized from the basic wavelet function called the "mother" wavelet.
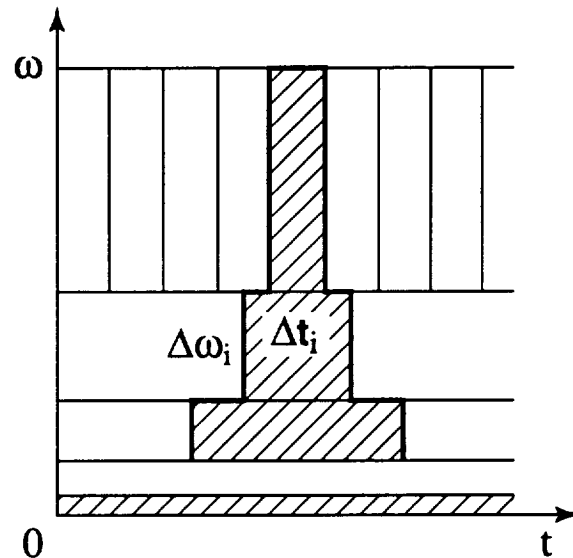
Figure 5.2 The time series representation in time and frequency space (Lau and Weng, 1995).

Wavelets are usually classified into two different categories, orthogonal and continuous wavelets. Orthogonal wavelets usually work in pairs, a wavelet function and a scaling function. These are used to decompose a signal into two parts, the low frequency components and the high frequency components. They are more suited for data compression and modeling. Continuous wavelet functions stand alone and are used primarily for signal processing. Although wavelets can be thought of as decomposing a signal into different frequencies, in wavelet space the signal is actually defined on different scales, or changes in dilation.

Due to the flexibility of wavelets for both time and frequency they are useful for analyzing a signal that may have information localized in time at different scales. Not only can the mother wavelet be stretched and compressed it can be translated in space to cover the whole signal. Therefore, a continuous wavelet can easily narrow in on the higher

frequencies and widen for the lower frequencies This allows wavelets to be useful in many different applications of science including atmospheric sciences. The use of wavelets in atmospheric science has been increasing due to its popularity. Some of those that have used wavelets in their analysis are Gollmer et al. (1995), Weng and Lau (1994), and Kumar and Foufoula-Georgiou (1994) along with many others.

2. Wavelets

Wavelets can be used beyond one-dimensional data sets, but for a description of the basic concepts and for the use in this study one-dimensional theory will be used.

Wavelets itself refers to a set of small waves that are changed by dilation, $\Psi(t) \rightarrow \Psi(at)$, and translation, $\Psi(t) \rightarrow \Psi(t + b)$. The set of waves that result from changes to the mother wavelet, $\Psi(t)$, are usually called a family of wavelets, or daughter wavelets. Each of the members of the family will have the same shape as the mother wavelet, but will be distorted by how it is dilated and translated. Mathematically the members of a wavelet family are defined as

$$\Psi_{b,a}(t) = \frac{1}{(a)^{1/2}} \Psi\left(\frac{t - b}{a}\right) \qquad (5.1)$$

where b is the translation, a the scale or dilation of the wavelet, and $\Psi_{b,a}(t)$ are the wavelets or family members, Figure 5.3 demonstrates the dilation and translation. The term $(a)^{-1/2}$ is an energy normalization factor which keeps the energy of each wavelet the same as the mother wavelet (Lau and Weng, 1995). The wavelet transform mathematically is not much unlike the Fourier transform and is expressed as

$$W(b,a) = \int_{-\infty}^{\infty} f(t)\Psi_{b,a}(t)dt = \frac{1}{(a)^{1/2}} \int_{-\infty}^{\infty} f(t)\Psi\left(\frac{t - b}{a}\right)dt \qquad (5.2)$$

where the f(t) is the data. As with Fourier transforms the data can be reconstructed by an inversion formula

$$f(t) = \frac{1}{C_\Psi} \int\limits_{-\infty}^{\infty} \int\limits_{0}^{\infty} \Psi_{b,a}(t) W(b,a) \frac{dadb}{a^2}$$ (5.3)

where

$$C_\Psi = \int\limits_{0}^{\infty} \frac{|\hat{\Psi}(\omega)|^2}{\omega} d\omega < \infty$$ (5.4)

and $\hat{\Psi}$ is the Fourier transform of Ψ.

The function that describes a wavelet can be about any function as long as it meets two conditions. The first condition was already discussed and is that the function has to be able to be translated and dilated. The other condition is in two parts (i) the wave amplitude must have a fast decay, and (ii) the function must meet the admissibility condition. The admissibility condition basically means that the function must have finite length and a bounded magnitude (Gollmer, 1994). Equation (5.4) is the more abstract way of expressing it, but it can be expressed as having a zero mean giving

$$\int\limits_{-\infty}^{\infty} \Psi(t)dt = 0$$ (5.5)

The first ensures that it is not a sustained wave and the second is that it is wave like. Figure 5.1 shows an example of the decaying amplitude. The admissibility condition along with the requirement that it decays in amplitude is why the function $\Psi(t)$ is called a wavelet.
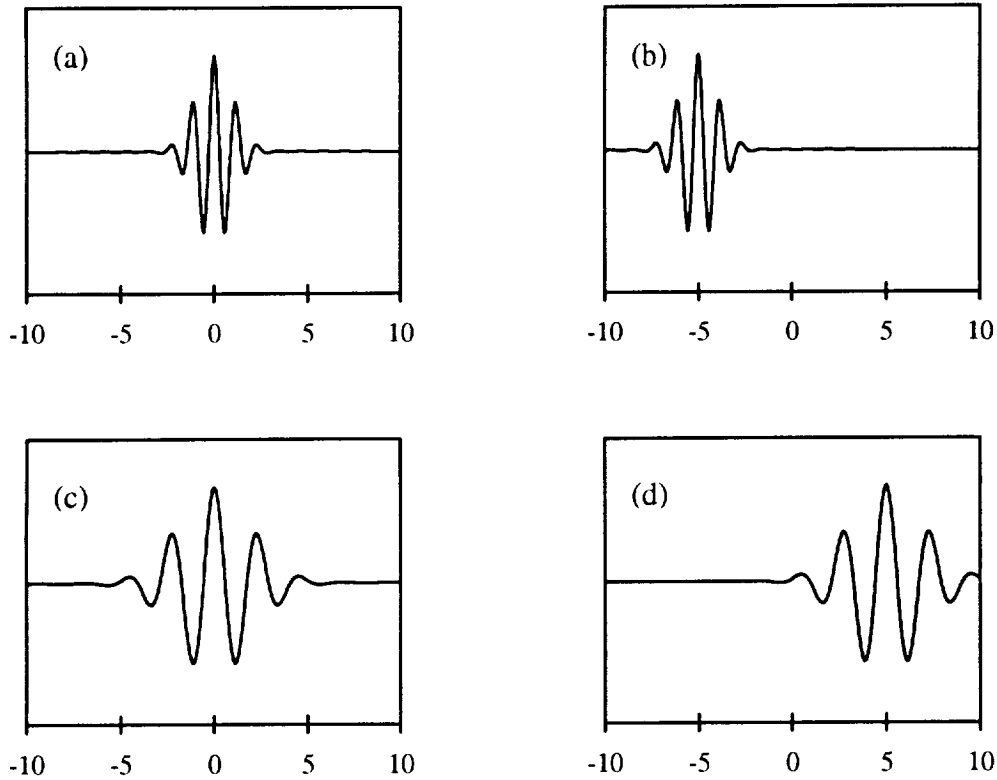
Figure 5.3 The Morlet wavelet translated and dilated (a) a=1, b=0 (mother wavelet), (b) a=1, b=-5, (c) a=2, b=0, and (d) a=2, b=5.

a. Continuous Wavelets

Continuous wavelet functions are usually the most flexible transforms to be used in time series analysis. The type of function used will usually depend on the type of information needed. There are two categories of continuous wavelet functions, real-valued wavelets and complex-valued wavelets. Both types of wavelets will provide information through the real coefficients and the modulus, which is the energy density of the signal. The complex-valued wavelets can also provide information on the phase of the signal, which detects singularities and measures instantaneous frequencies (Weng and Lau, 1994).

An example of a real-valued continuous wavelet is the Mexican Hat, shown in Figure 5.4. This wavelet is a second derivative of the Gaussian function where the

constants are chosen such that $\|\Psi\|^2 = 1$ (Kumar and Foufoula-Georgiou, 1994). The wavelet function is

$$\Psi(t) = \frac{2}{\sqrt{3}} \pi^{-1/4} (1 - t^2) e^{-t^2/2}$$
(5.6)
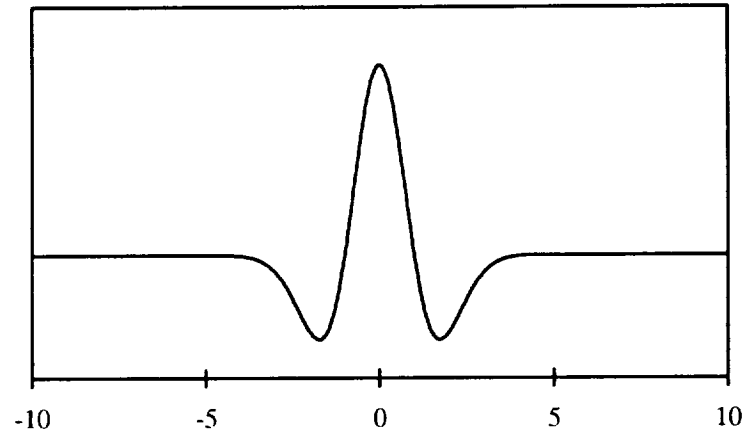
Figure 5.4 Mexican hat wavelet.

The Mexican hat and other second derivatives of smoothing functions have been used in edge detection applications (Kumar and Foufoula-Georgiou, 1994).

Within the complex-valued wavelets the most widely used continuous wavelet function is the Morlet, Figures 5.1 and 5.3 are examples of the real part. The Morlet is another Gaussian type of function where the Gaussian function is the window, while the rest of the function is the wave part. The function for the Morlet is given by

$$\Psi(t) = e^{iCt} e^{-(|t|^2/2)}$$
(5.7)

For the Morlet to be considered a wavelet the constant C must be ≥ 5.

The Morlet wavelet's popularity is due to its flexibility in its applications. For examples of the use of the Morlet see Lau and Weng (1995), Weng and Lau (1994),

Meyers et al. (1993), and Spedding et al. (1993). The Morlet wavelet is the wavelet function of choice for this study.

The reason for terming these wavelets as continuous is because in theory the parameters for dilation, a, and translation, b, must be continuous. This is an advantage over other types of wavelets in that every scale of the spectrum can be analyzed for the signal. The dilation can start out infinitely small and can be stretched in any size increments. Unfortunately for practical applications in order for the parameters to maintain continuity, they have to be defined in discrete intervals. When the parameters a and b are considered to be discrete values, equation (5.1) can be written as

$$\Psi_{m,n}(t) = a_o^{-m/2}\Psi\left(\frac{t - nb_o a_o^m}{a_o^m}\right)$$

(5.8)

where a and b > 1 and m,n are integers. The scales of analysis must be chosen in incremental steps from largest to smallest to get as much information as needed. One special group of discrete wavelets are the orthogonal wavelets.

b. Orthogonal Wavelets

The discrete wavelets that form an orthogonal basis are considered orthogonal wavelets. This basis is constructed from the following relationship:

$$\int \Psi_{j,i}(t)\Psi_{j',i'}(t)dt = \delta_{jj'}\delta_{ii'}$$

(5.9)

where δ_{ij} is the Kronecker delta. This implies that the individual wavelets are orthogonal to their dilates, a, and their translates, b. This changes equation (5.8) to the form

$$\Psi_{j,i}(t) = 2^{j/2}\Psi(2^j t - i) \tag{5.10}$$

where $a = 2^{-j}$ and $b = 2^{-j}i$.

Orthogonal wavelets as was mentioned earlier come in pairs, the wavelet function and the scaling function. The scaling function $\Phi_{j,i}$ acts as a low pass filter which can be used to smooth the signal. Whatever is lost by the scaling function in analyzing the data can be compensated by the wavelet function (Gollmer, 1994). Between both functions a signal can be decomposed into wavelet space and then completely reconstructed.

The simplest orthogonal wavelet and the first of all wavelets is the Haar wavelet. The function for the Haar wavelet is

$$\Psi(t) = \begin{cases} 1, & 0 \le t < 1/2 \\ -1, & 1/2 \le t < 1 \\ 0, & otherwise \end{cases} \tag{5.11}$$

and the scaling function is the box function given by

$$\Phi(t) = \begin{cases} 1, & 0 \le t < 1/2 \\ 1, & 1/2 \le t < 1 \\ 0, & otherwise \end{cases} \tag{5.12}$$

The Haar wavelet itself is not well suited for use in analyzing data, but is useful for explaining how wavelet analysis is done.

There are many other orthogonal wavelet functions, some of the most fundamental and widely used were developed by Daubechies (1992). The Daubechies wavelets are used in almost every situation which involves the use of orthogonal wavelets. Within the atmospheric sciences Gollmer (1994) used one of the Daubechies wavelets to analyze liquid water path data to develop a one dimensional cloud model.

3. Scalograms

One of the most common ways of illustrating the coefficients of a continuous wavelet analysis is through the use of a scalogram. The scalogram takes the analysis of a signal at each of the dilations, scales, and represents it in a 2-D image. Each row of the scalogram is a representation of the analysis determined at a particular scale. The rows are a logarithmic scale of the frequency, highest frequency at the top and lowest frequency at the bottom. As was mentioned before the term scale can be proportional to the frequency. The rows are a linear representation in time, this is usually the horizontal axis. Figure 5.5 is an example of a wavelet analysis using the Morlet wavelet on a sine function, Figure 5.5a, that changes frequency midway through the signal.

Figure 5.5b is the scalogram that represents the real parts of the wavelet coefficients, they represent both the intensity and the phase combined. The real scalogram can be used to find periodic trends in the data. The example in Figure 5.5b illustrates the oscillation in the sine wave by the oscillation of the positive and negative real coefficients between scale 6.0 and 7.0 for the lower frequency, and between scale 5.0 and 6.0 for the higher frequency.

Figure 5.5c is the modulus scalogram of the wavelet coefficients, the modulus represents the energy of the signal in both time and scale, or frequency. The modulus is useful in determining the strength of the signal in the wavelet domain, it can also pinpoint changes in the scale of the signal. From Figure 5.5c the dominant energies at the particular scales, or frequencies, of both waves are easily found. Also the point where the frequency changes can be determined.

Figure 5.5d is the phase scalogram of the wavelet coefficients, this representation can only be used when the wavelet function is complex. The phase scalogram can detect singularities or sudden changes by the convergence of the phase lines (Weng and Lau, 1994). At each scale there is a decrease in the phase, from π to $-\pi$. After it reaches $-\pi$ it starts back over again at π. From Figure 5.5d the location at which the frequency changes is easily located between the 500.0 and 625.0 time markers.
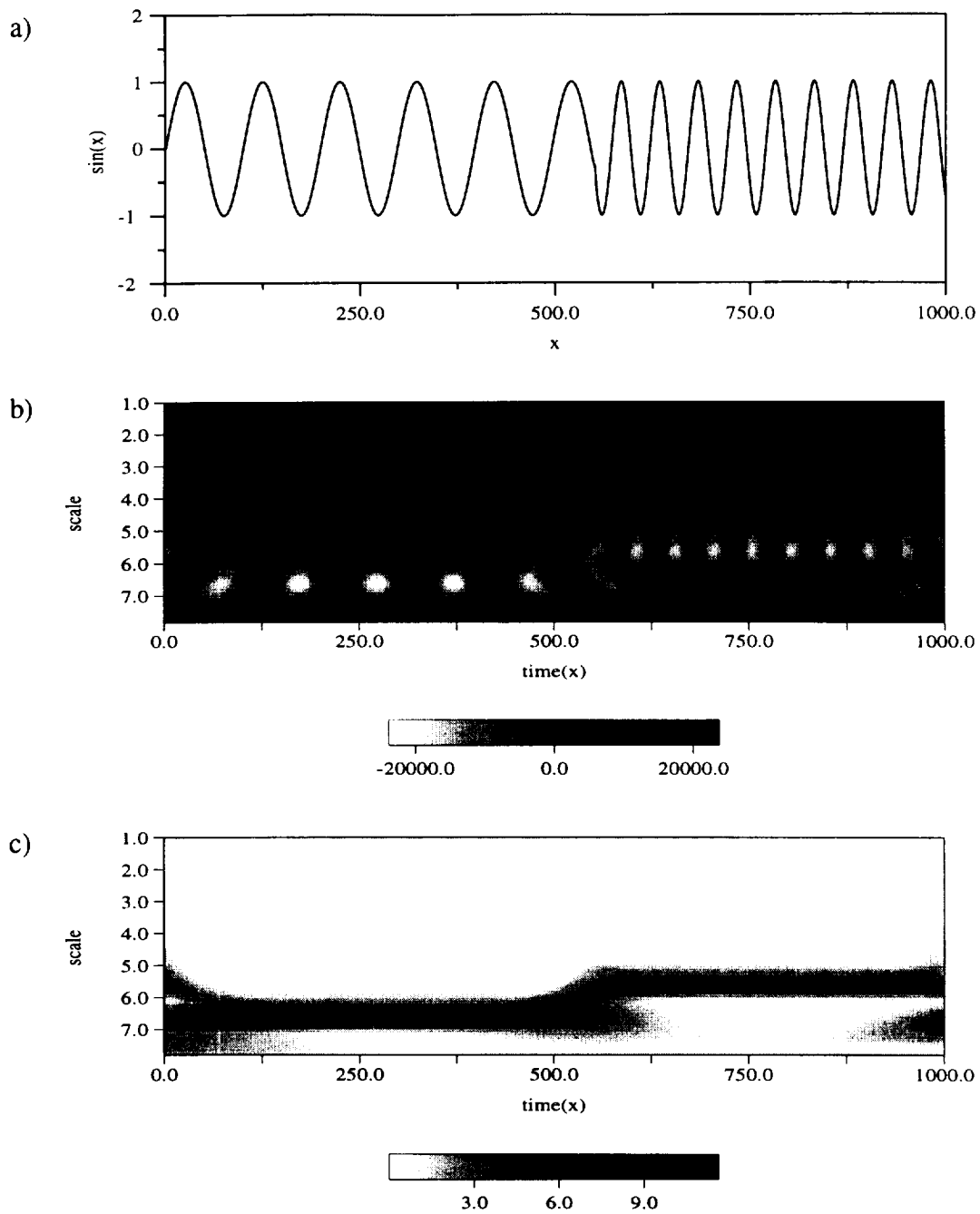
Figure 5.5 Wavelet transform using the Morlet wavelet function of a sine wave, (a), that changes frequency midway through the signal. 5.5b is the scalogram of the real coefficients, 5.5c is the scalogram of the modulus and 5.5d is the scalogram of the phase.

d)
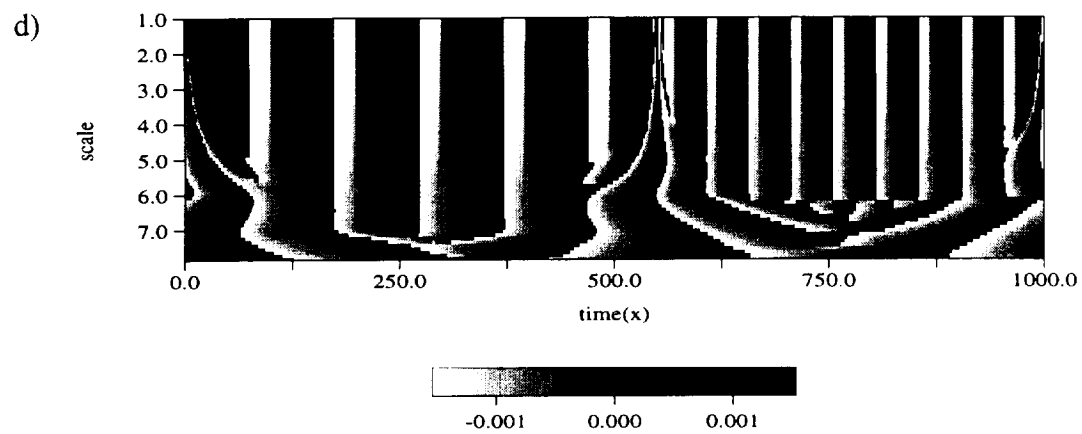
Figure 5.5 continued

CHAPTER 6. LIQUID WATER CONTENT ANALYSIS

The scales of the Liquid Water Content (LWC) data sets from ASTEX are analyzed in this chapter. The two techniques used to analyze the scales are the power spectrum from the Fourier Transform, and the scalograms from the Wavelet Transform. The purpose of this part of the study is to look at the relationship between higher and lower scales in a turbulent marine stratocumulus cloud structure.

1. Method of Analysis

To analyze the scales of the LWC data both wavelet analysis and Fourier transforms were used. Even though wavelets have a definite advantage over Fourier analysis for dealing with localizing scales in time and space, the power spectrum from the Fourier transform is still very useful. The power spectrum can be used to look at the trends in the frequency of the data to indicate relationships between different wavelengths, or scales, of the data.

a. Fourier Analysis

A Fourier transform was applied to each of the LWC data sets from the PVM-100A probe during ASTEX. The power spectrum of each of the fouriered data sets was calculated. Eighteen of the power spectrums were averaged together in order to eliminate most of the noise. The slope of the averaged power spectrum was analyzed for relationships between scales; this will be discussed later.

b. Wavelet Analysis

The mother wavelet chosen for this analysis is the Morlet wavelet. The Morlet wavelet was chosen mainly because it is a continuous and complex wavelet. It also has proven itself to be very flexible in many other areas of science. The complex Morlet is able to localize the signaling in both time and frequency continuously (Weng and Lau, 1994).

Since the wavelet analysis can represent its coefficients in a 2-D format, called a scalogram, the amount of computer time and space limits the amount of data that can be analyzed. Therefore, only marine stratocumulus cloud segments of the data were chosen to keep the analysis strictly to that of the clouds and to be more efficient with computer space and time. Due to marine stratocumulus clouds having large cloud fractions and very small aspect ratios, 1000 to 4000 data points were considered sufficient as a data sample to represent a cloud. Since the resolution gathered by the PVM-100A is 8 m for each data point the analyzed cloud segment becomes 8 to 32 km. Another important requirement for the data sample is that it must have stationarity with little or no breaks in the cloud. This was done to represent marine stratocumulus clouds and to avoid errors in the analysis. The PVM-100A data files where a data sample could be taken meeting the above conditions are June 2 #1, #2, #3; June 4 #4; June 8 #8, #9; June 12 #10, #11, #12, #13; June 13 #15, #16, #18, #19; June 15 #20; June 16 #22; June 17 #24, #25, #26, #27, #28; June 20 #31; June 21 #35; June 22 #36, #38; and June 23 #42, where each number is a separate flight track represented in Figures 4.1 to 4.15.

Before the data sample was analyzed with the wavelet transform it was detrended, and each end was padded to make it appear periodic. Detrending the data sample is simply calculating the slope of the data, subtracting the line fitting the slope from the data, and then adding back in the original mean of the data sample. An example of a data sample before and after detrending is shown in Figure 6.1. The detrending of the data left the over all structure of the data but eliminated the trend so that when each end is padded the data sample would still remain stationary. The Morlet wavelet transforms, as well as many others, have edge effects at the beginning and end of the scalogram. This edge
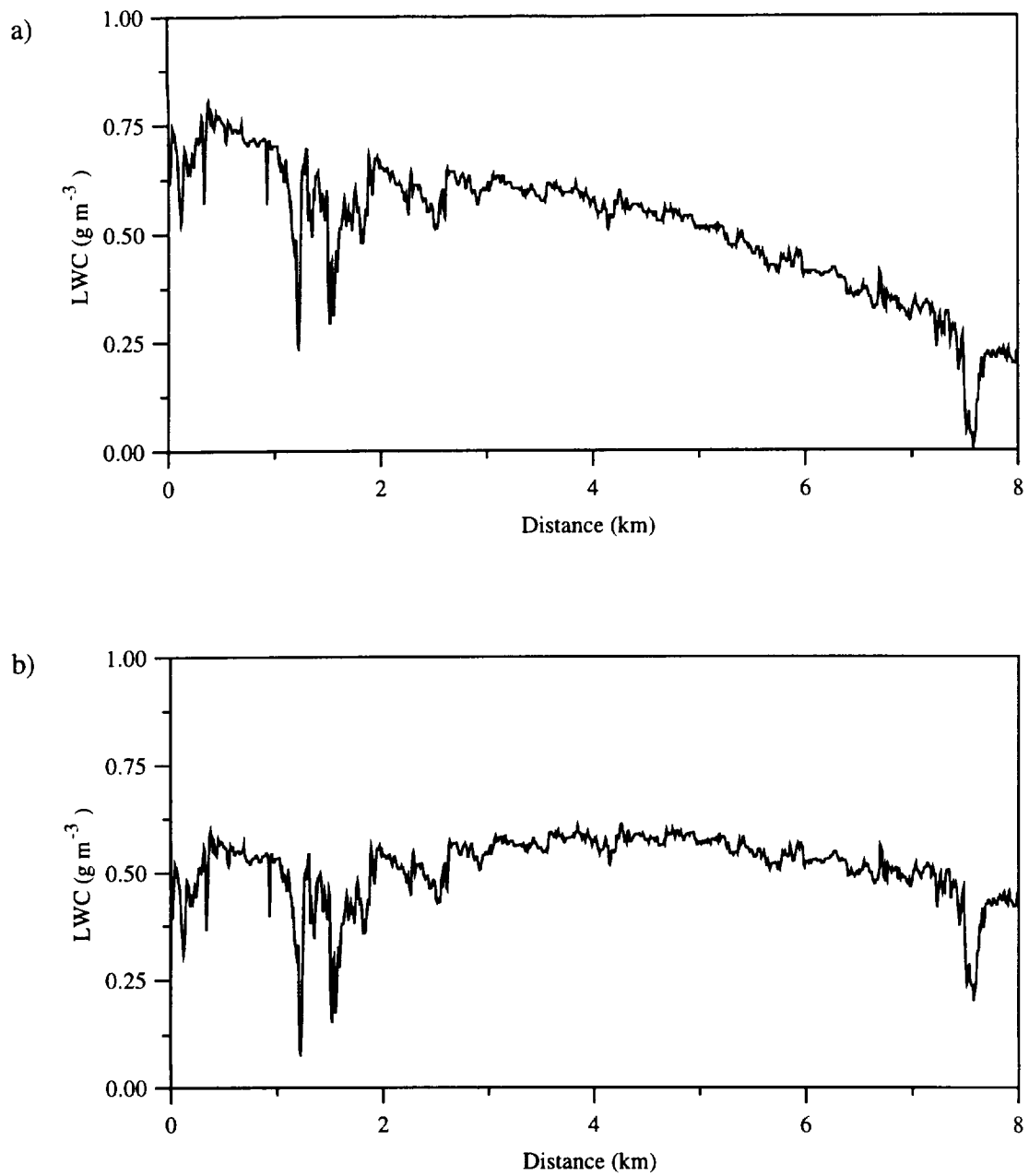
Figure 6.1 LWC data sample from flight track #15 on June 13, 1992, where (a) is the data containing the trend and (b) is the data without the trend.

effect shows up at the edges of the larger scales of the modulus scalogram and causes the analysis to be unreliable. To minimize this, approximately 200 data points were padded on either end of the data sample to assuming periodicity. After the wavelet analysis is performed the 200 or so coefficients on either end are discarded.

Although the number of scales from the smallest to the largest can be infinite due to the continuity of the wavelet function, realistic limitations require that the steps between scales must be specified discretely. How small the step will be depends upon the resolution allowed by the technology used and how much accuracy is needed. The study used an octave/voice concept for stepping one scale to the next. Just like in music where each step in a musical scale can be considered a voice, or note, and every eighth voice is considered an octave, the same can be applied to the stepping of the scales in wavelets. An octave can loosely be considered as doubling the scale, or wavelength. The number of voices will depend upon the need for accuracy. For the scalograms in this study the number of octaves, m, and the voices, v, were each set to ten. To incorporate this octave/voice concept in the scale parameter of the wavelet transform, a, the following expression is used:

$$a(m,v) = 2^{(n-m)/v} \tag{6.1}$$

where $n = m*v$. As was noted in the previous chapter, due to the uncertainty principle with each increase in an octave, the wavelength or frequency accuracy doubles but the time accuracy reduces by half.

In this study the scales can be considered equivalent to wavelengths or wave numbers instead of frequency and time. The reason for this is that the data samples are taken over small time segments making analysis on a time scale unrealistic.

The resulting scalograms from this study do not contain all of the octaves and voices that are originally defined. The scales below the Nyquist frequency are discarded since there is no information that can be determined from them. Therefore, the smallest scale of the scalogram, top of the scalogram, will be the wave number, k, associated with

the Nyquist frequency. Since the frequency at which the data is retrieved is 10Hz the Nyquist frequency will be 5Hz. With a resolution of 8 meters the wave number that is associated with the Nyquist will be 392.7 km^{-1}. Each octave then will be a doubling of the wavelength or a halving of the wave number.

An example of how the scalogram is setup is shown in Figure 6.2. This is the same wavelet example of the sine function used in the previous chapter, without the phase scalogram. In the previous chapter each octave on the scalogram was sequentially labeled on the vertical axis starting from the Nyquist frequency, and the horizontal axis represented each point. In the current scalogram example the axes are relabeled to have the same characteristics of the LWC data from ASTEX. Instead of labeling the vertical axis for scale it is labeled for wave number, and the horizontal axis is distance instead of time where each point is 8 m long.

For most disciplines of science the scalogram is used for locating dominant scales or scale ranges in time, also locating trends and periodicity. Since this study is looking at the relationships between scales the analysis must go one step further. From Fourier analysis and Kolmogorov theory, the correlation of the energy from the modulus at two scales is similar to the correlation of the variability at two scales. Therefore, the variability of each scale in the modulus scalogram was computed by taking the standard deviation at each scale. Figure 6.3 is an example of the standard deviation for each scale of the modulus scalogram of the sine wave in Figure 6.2c. To compare the variability of two scales a ratio was taken of the smaller scale to the larger scale.

2. Analysis

From both of the analysis methods a strong correlation can be found between scales of a marine stratocumulus cloud. The Fourier power spectrum slope indicates this correlation by Kolmogorov (1941). The wavelet standard deviation ratios show the correlations between not only the octaves but at smaller steps in scale.
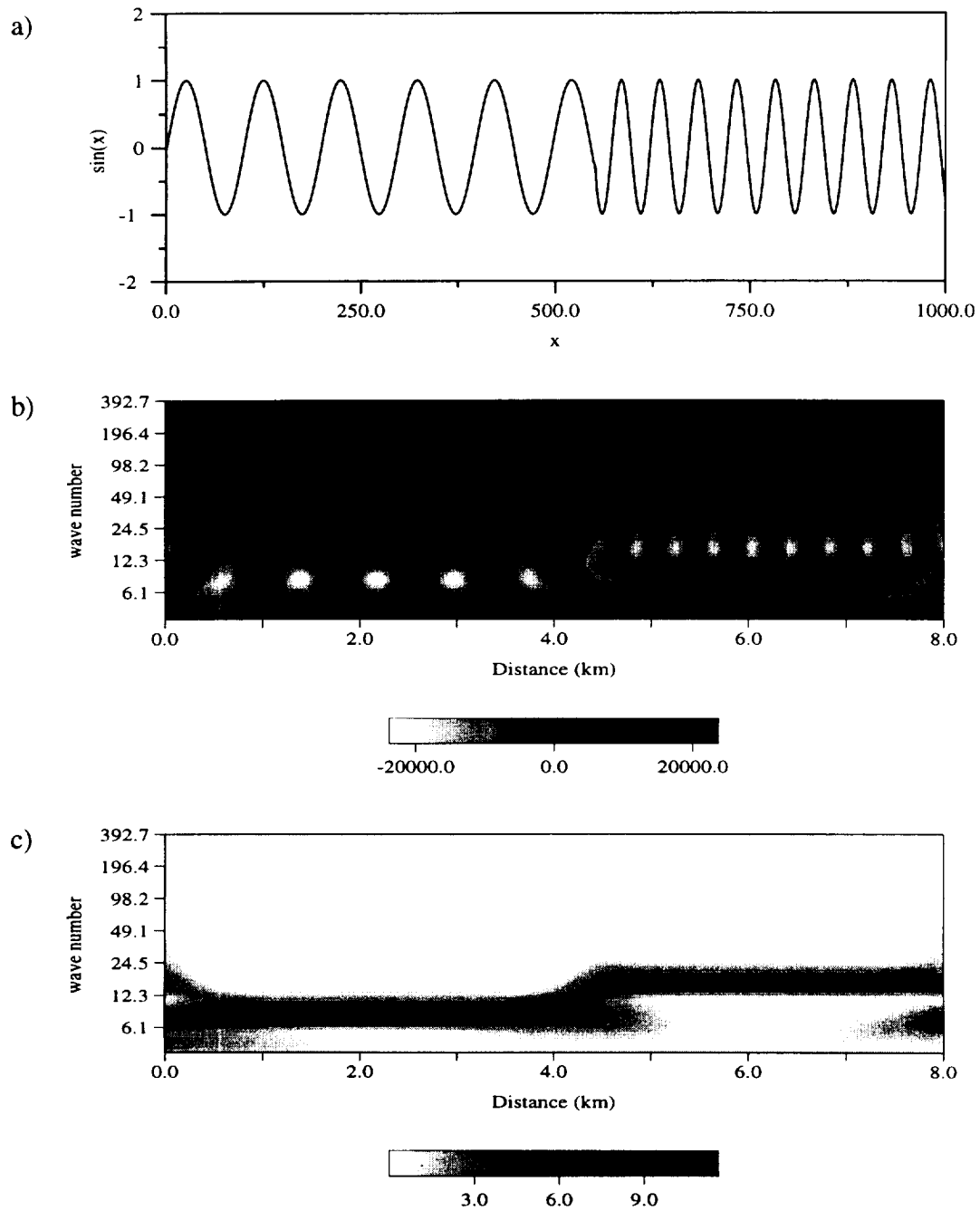
Figure 6.2 Wavelet scalogram with the vertical axis as wave number (km^{-1}) and horizontal axis as distance (km) for the sine wave function (a). 6.2b is the scalogram of the real coefficients and 5.5c is the scalogram of the modulus.
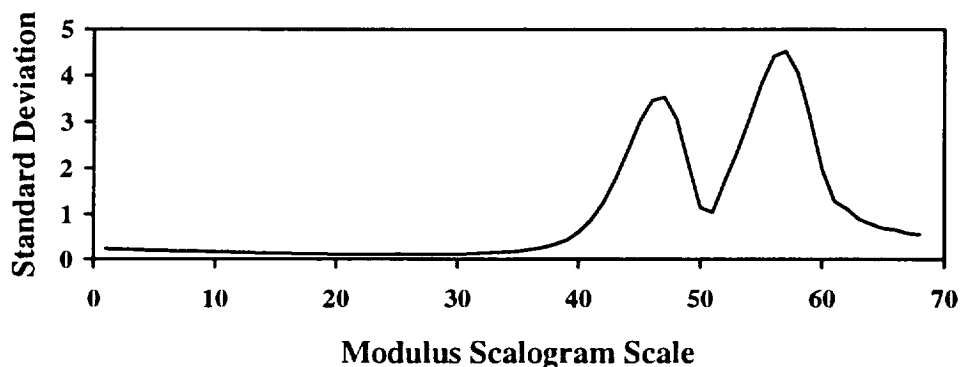
Figure 6.3 The standard deviation of each scale of the modulus scalogram from the two frequency sine example.

a. Power Spectrum

Figure 6.4 is the averaged Fourier transform power spectrum of the 18 LWC data files. The power spectrum exhibits a definite slope from smaller to larger wave numbers. This indicates that the energy is being transferred from the larger to the smaller scales in the cloud due to its turbulent characteristics. Since the absolute value of the slope of the power spectrum, m ≈ 2.55, is greater than the "5/3" law (Kolmogorov, 1941) the energy is not evenly distributed among the scales of the cloud. It can be assumed that when the absolute value of the power spectrum slope is greater than 5/3 that there is more energy in the larger scales than in the smaller scales; loosely, this can indicate cloud development. If, on the other hand, the absolute value of the slope is less than 5/3 then there is more energy in the smaller scales and possible cloud dissipation. Since the absolute value of the slope in Figure 6.4 is greater than 5/3 it will be considered that from the LWC data there is more energy in the larger scales and cloud development could be taking place.

An interesting thing to note in the power spectrum is a scale break toward the higher wave numbers, between 100 to 200 km^{-1}. This break in scale changes the absolute value power spectrum slope to greater than 5.0. The break has also been observed by Gollmer (1994) while looking at Landsat liquid water path data of marine stratocumulus
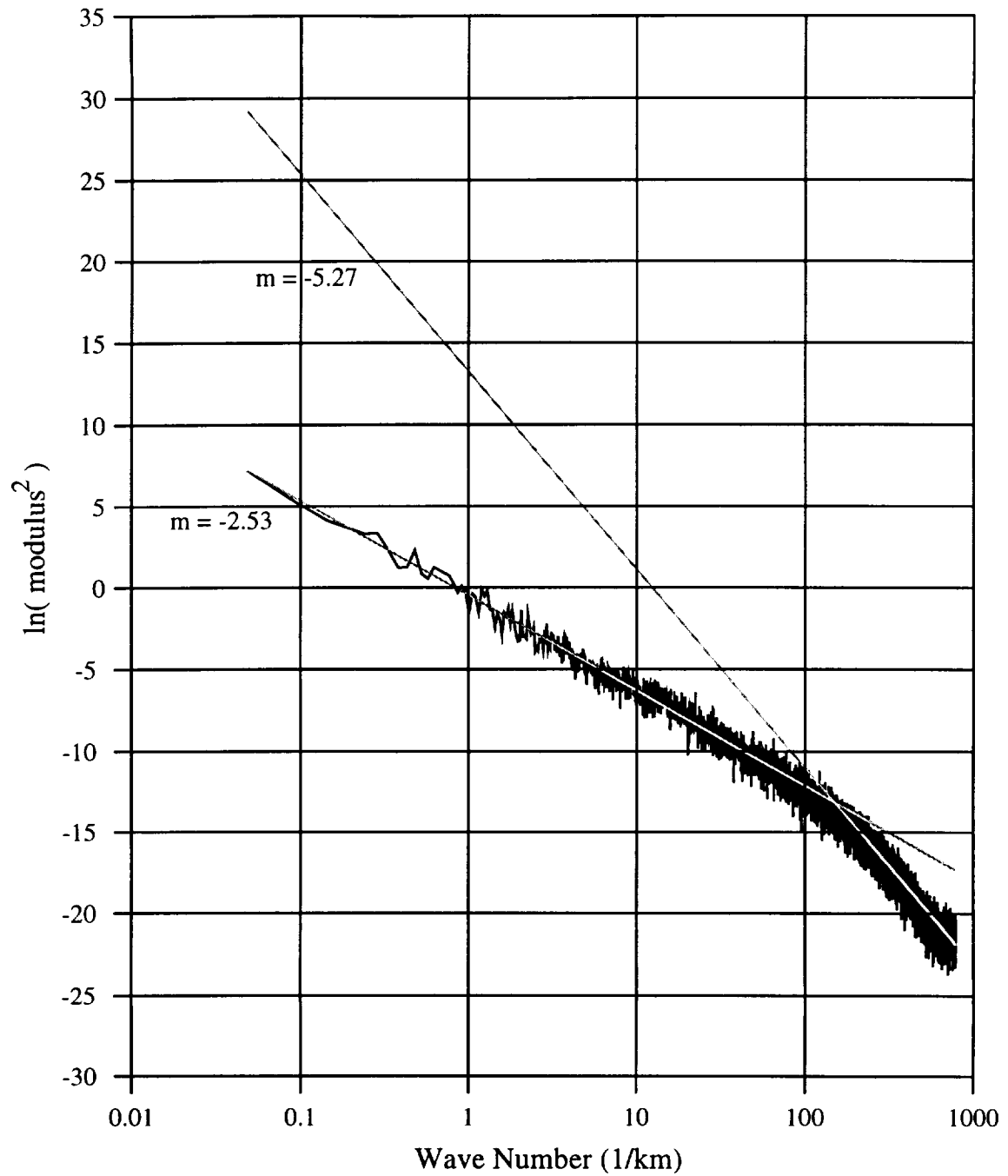
Figure 6.4 Power Spectrum for LWC data sets from PVM-100A taken during the ASTEX project.

clouds. He explained that the scale break was possibly due to dynamic or radiative effects in the clouds. Davis et al. (1996) also observed a similar scale break in the ASTEX LWC data and suspected that it was due to the presence of large jumps at the smaller scales.

b. Wavelet Analysis

Figures 6.5 and 6.6 displays the time series and associated modulus scalogram for four of the data samples. As was pointed out before, the modulus scalogram represents the modulus, or energy, calculated from the complex coefficients of the wavelets at different scales. Each scale is an increase in the voice and is represented by a different row in the scalogram. In Figures 6.5 and 6.6 the vertical axis is a plot of the scale where in this case scale has been equated with wave number in km^{-1}. The scalograms are useful in pinpointing the location of events at a given time or distance interval. For example there is a pronounced maximum in the modulus for the June 8 time series (Figure 6.5c) as shown in Figure 6.5d between wave number octaves 12.3 and 6.1 km^{-1} and halfway between 8.0 and 12.0 km. This indicates that a scale of 0.5 to 1.0 km (12.3 to 6.1 wave numbers) exists in the cloud for a time equivalent distance of approximately 1.0 km. A more important detail that appears in all four of the modulus plots, is that the higher magnitudes of the modulus, or energy, is in the bottom portion of the scalogram or at the larger scales. This helps in verifying the Fourier power spectrum (Figure 6.4) which indicated that there is more energy at larger scales than at smaller scales.

Figure 6.7 though 6.9 displays standard deviation ratios of the smaller scale to the larger scale at three different intervals. The horizontal axis represents the ratio of standard deviations of two scales for a data sample modulus scalogram. The first interval (Figure 6.7) is a ratio between the octaves, the second interval (Figure 6.8) is a five voice ratio, and the third interval (Figure 6.9) is a four voice ratio. The first thing to note is the comparison of the standard deviation at the smallest scales, between the first and second octave (Figures 6.7a, 6.8a and 6.9a), the ratio is greater than 1.0. A ratio greater than 1.0 would indicate that there is more energy at the smaller scale than the larger scale. This would differ with the original premise that the larger scales have more energy. The larger
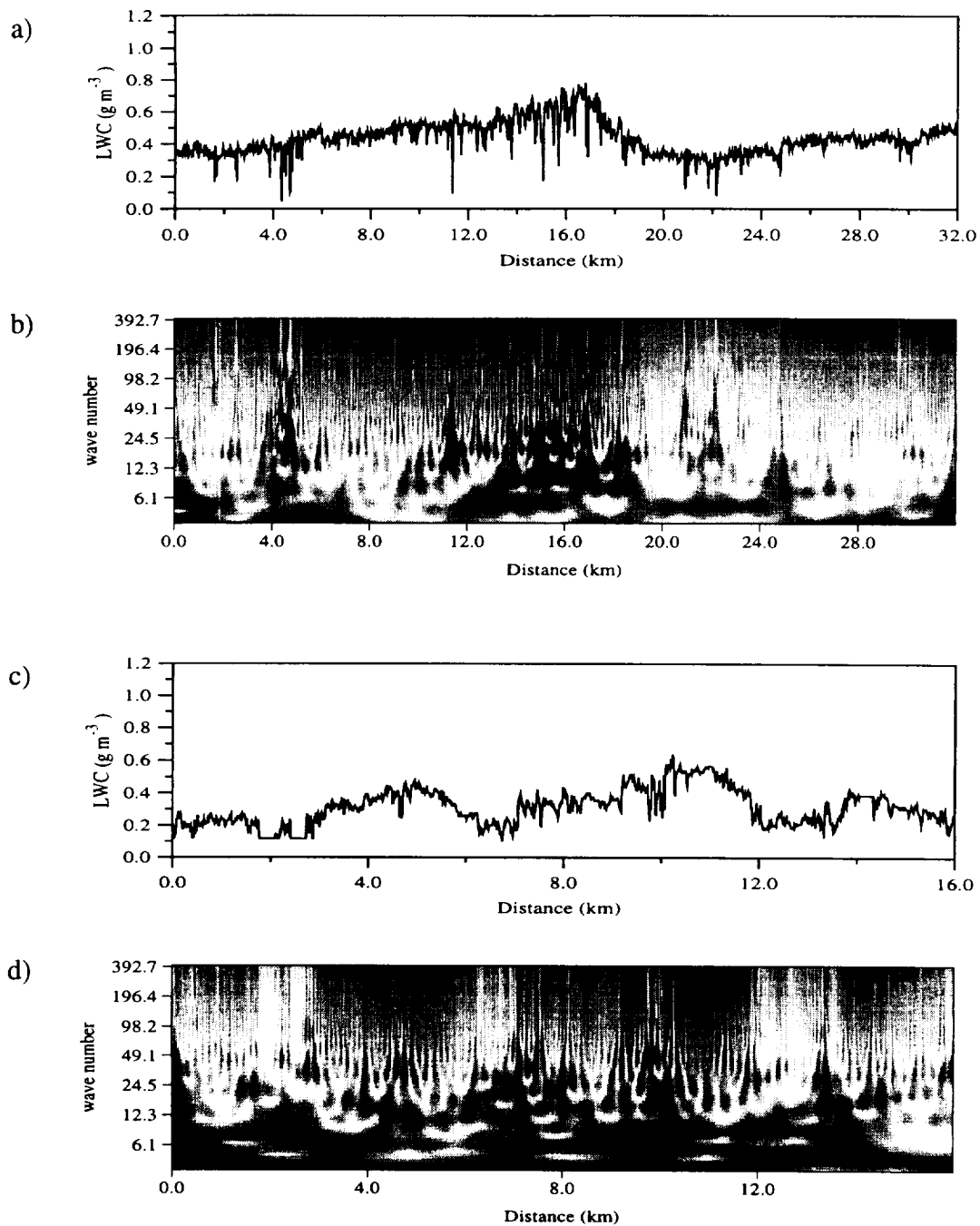
Figure 6.5 Time series data samples and modulus scalograms where wave number is in units of km⁻¹, and darker areas correspond to higher magnitudes and lighter areas correspond to lower magnitudes in the scalograms. For time series from (a) June 2, 1992 and (c) June 8, 1992 along with their modulus scalograms (b) and (d) respectively.
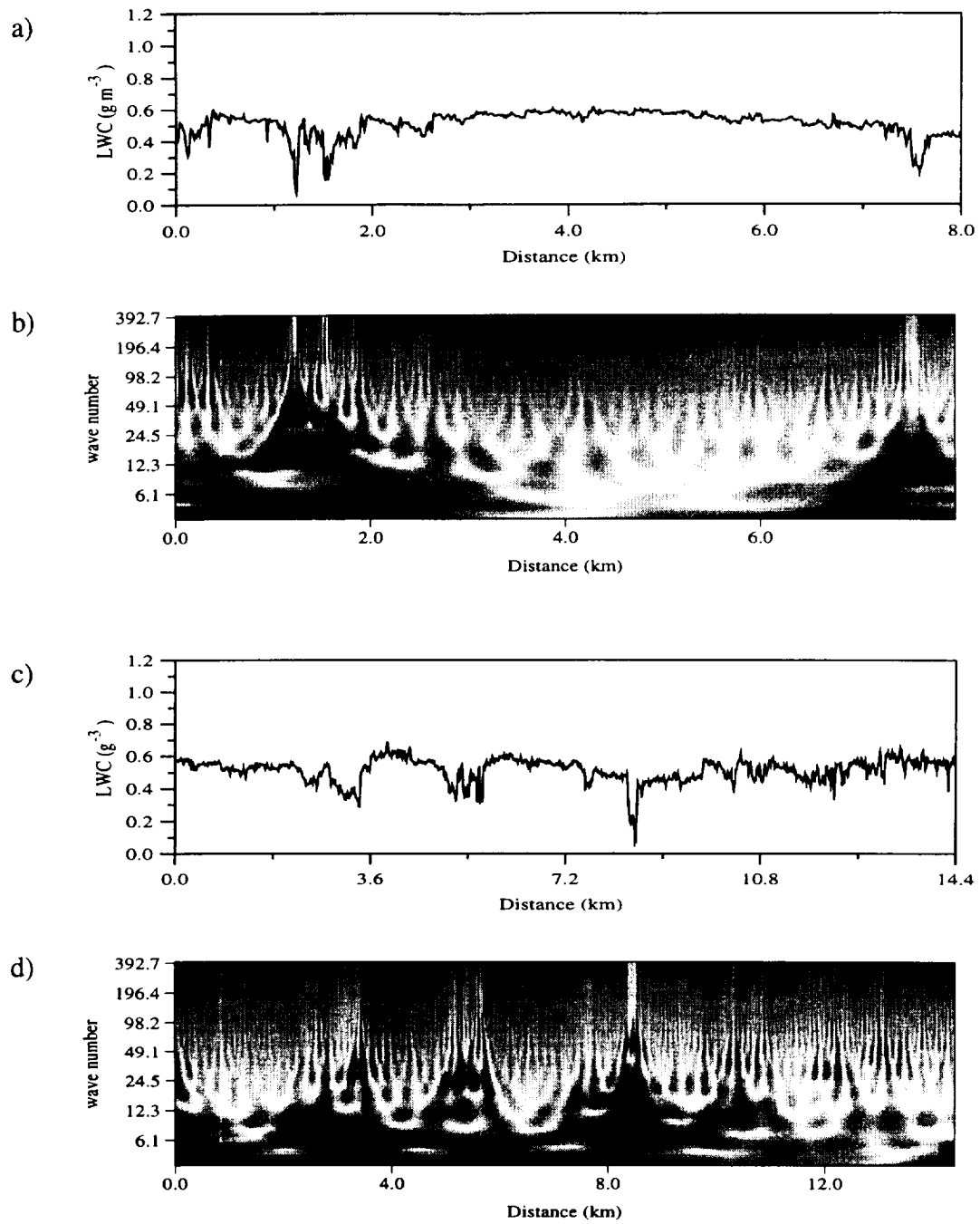
Figure 6.6 Same as Figure 6.5 except for time series from (a) June 13, 1992 and (c) June 17, 1992 along with their modulus scalograms (b) and (d) respectively.

ratios are not due to more energy at smaller scales but due to the noise at these scales. In order to look at the correlation between the data and the wavelet at the smallest scales, the wavelet scaling parameter, a, must be set very small. This causes the analysis to be done with a very narrow looking wavelet. Consider Figure 5.3a where the scaling parameter is so small that the resulting wavelet appears as a straight line. This will result in the noise in the data taking over and biasing the analysis at the smaller scales. The noise in the data is evident in the power spectrum (Figure 6.4) by the flattening out of the energy into a white noise pattern. Also the ratio is greater than 1.0 between the second two octaves (Figures 6.7b, 6.8b and 6.9b), not as much as between the first octave, but still greater than 1.0. Wavelets are not as good as Fourier analysis at filtering the noise, therefore, some of the noise seen in the ratios between the first two octaves leaks over to the ratios taken between the second two octaves causing the ratio to appear larger.

The standard deviation ratios beyond the noise barrier indicate a good correlation between the smaller and larger scales. The mean of the ratios are approximately less than 1.0 for all of the plots, these range from 0.7 to 0.9, indicating that the variability, or energy, is greater in the larger scales.

The mean value of the ratio increases towards 1.0 as the interval between the scales decreases. This can be seen by comparing the ratios between the octaves (Figure 6.10a) and the ratios between the interval of four voices (Figure 6.10c). Figure 6.10 displays the mean value of the ratios where the horizontal axis represents each ratio. This just indicates that as the interval of comparison between the variability of scales becomes smaller the energies are closer. It must be noted that the size of the interval is not linear, the interval needs to be much smaller at the larger scales than at the smaller scales to have the same mean value since the variability is higher at the larger scales. As the interval between the scales approaches an infinitesimally small interval the mean of the ratio will approach 1.0.

A step further could be taken in this study by ratioing the local variations in energy of a single scalogram. This is left for future study.
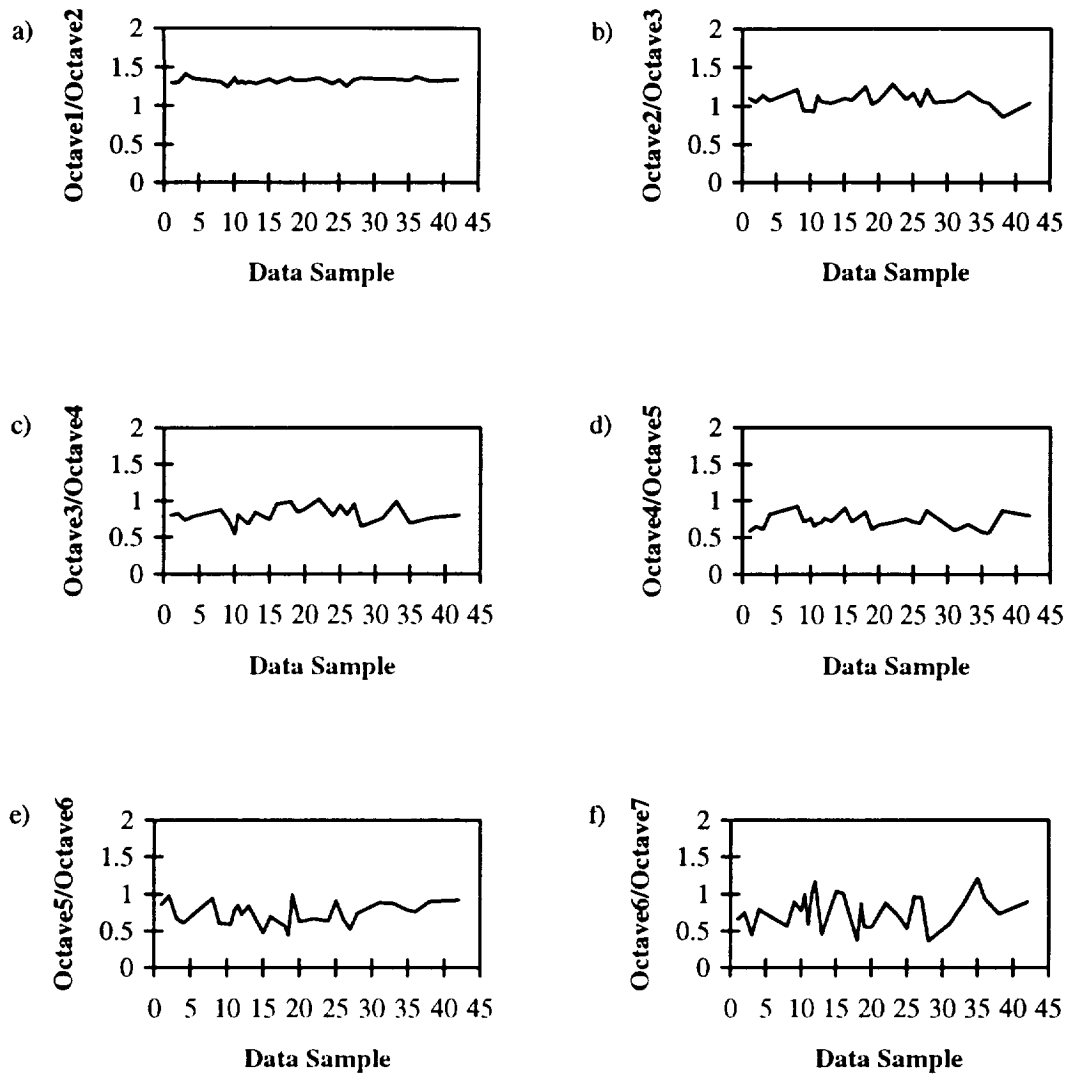
Figure 6.7 Ratio of the wavelet's standard deviation of the octaves, where the numerator is the lower scale and the denominator is the larger scale. Horizontal axis represents the data sample for which the wavelet was computed.
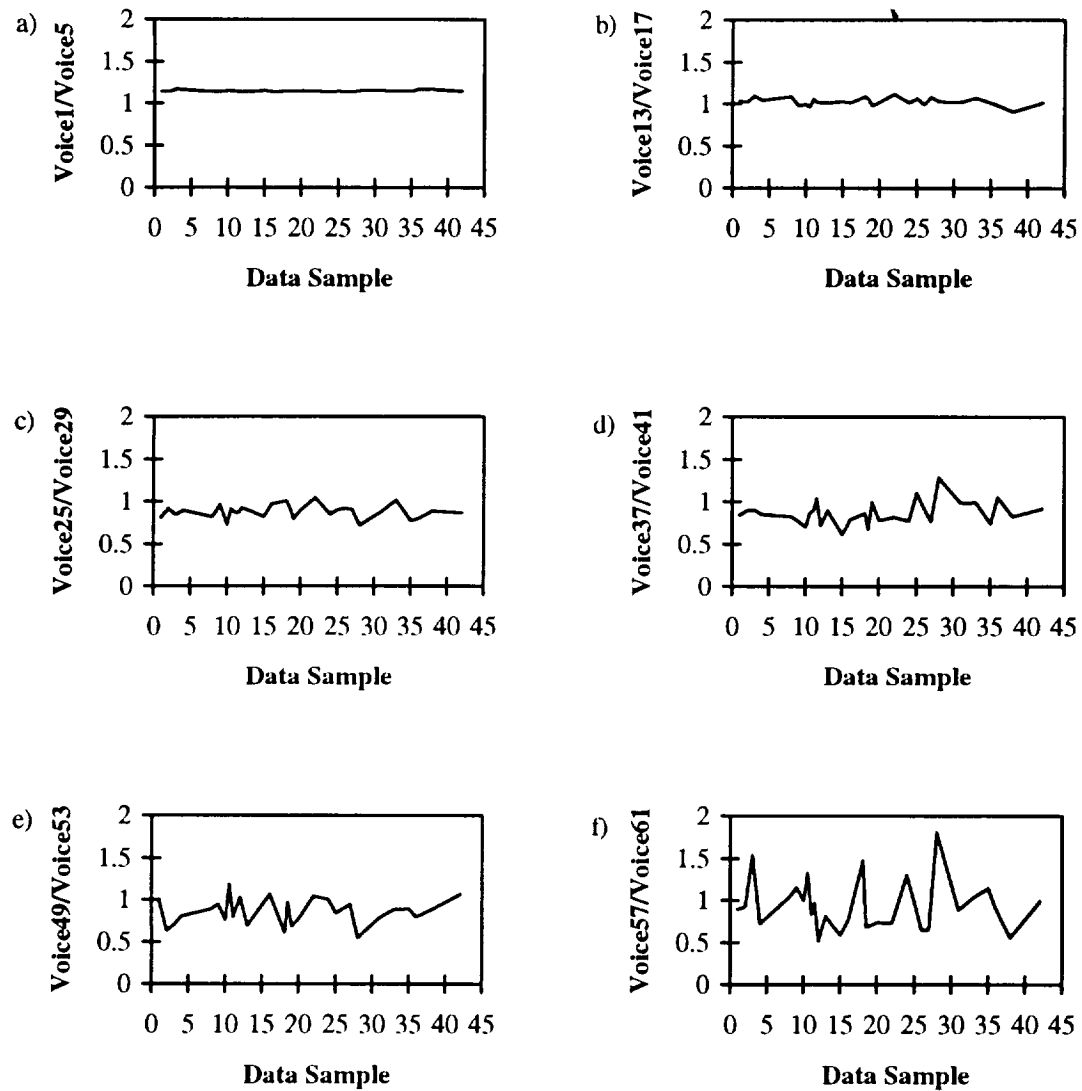
Figure 6.8 Ratio of the wavelet's standard deviation of the smaller scale, lower voice, to the larger scale, higher voice at an interval of five scales. Horizontal axis represents the data sample for which the wavelet was computed.
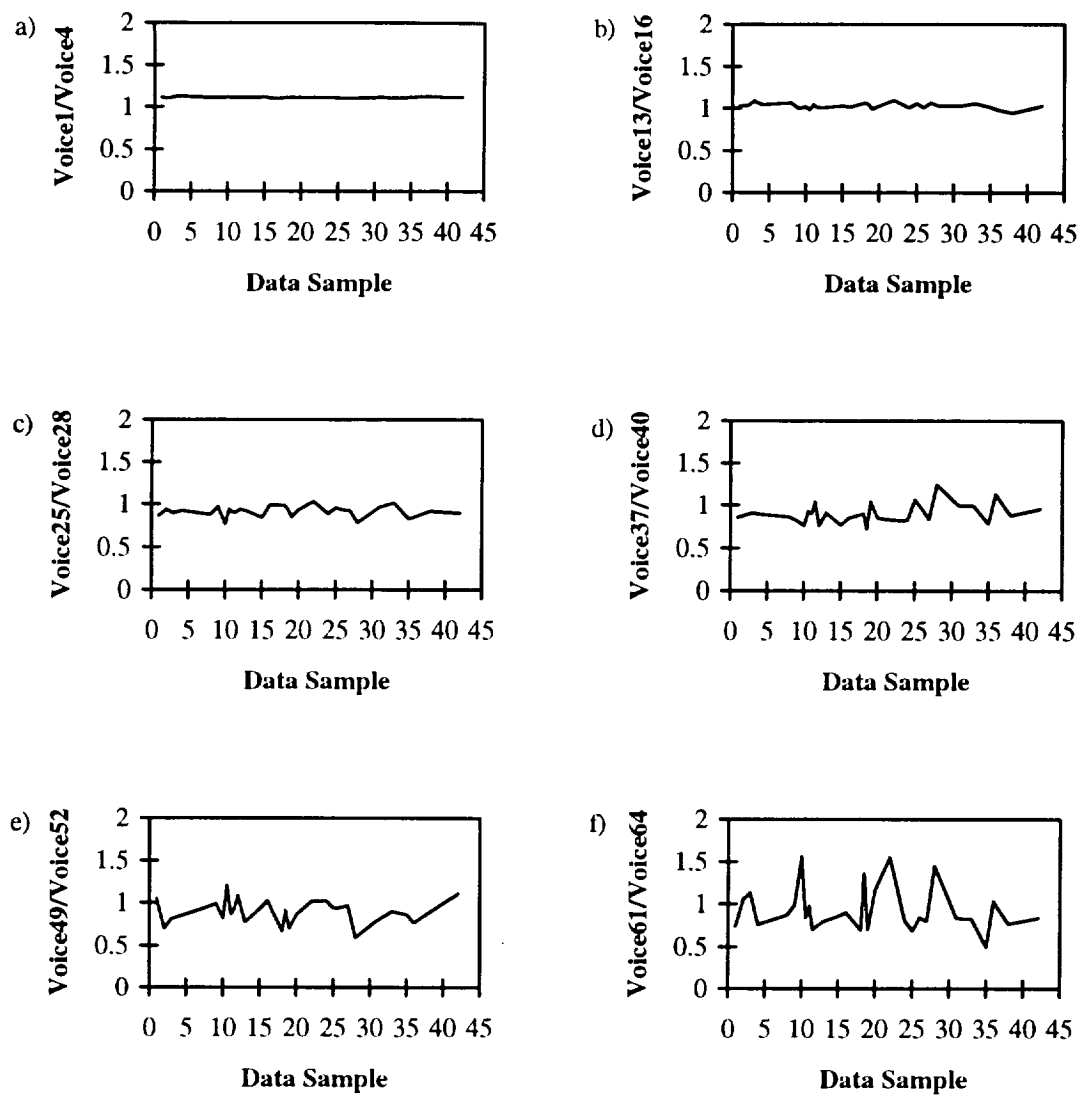
Figure 6.9 Same as figure 6.8 except for an interval of four scales.
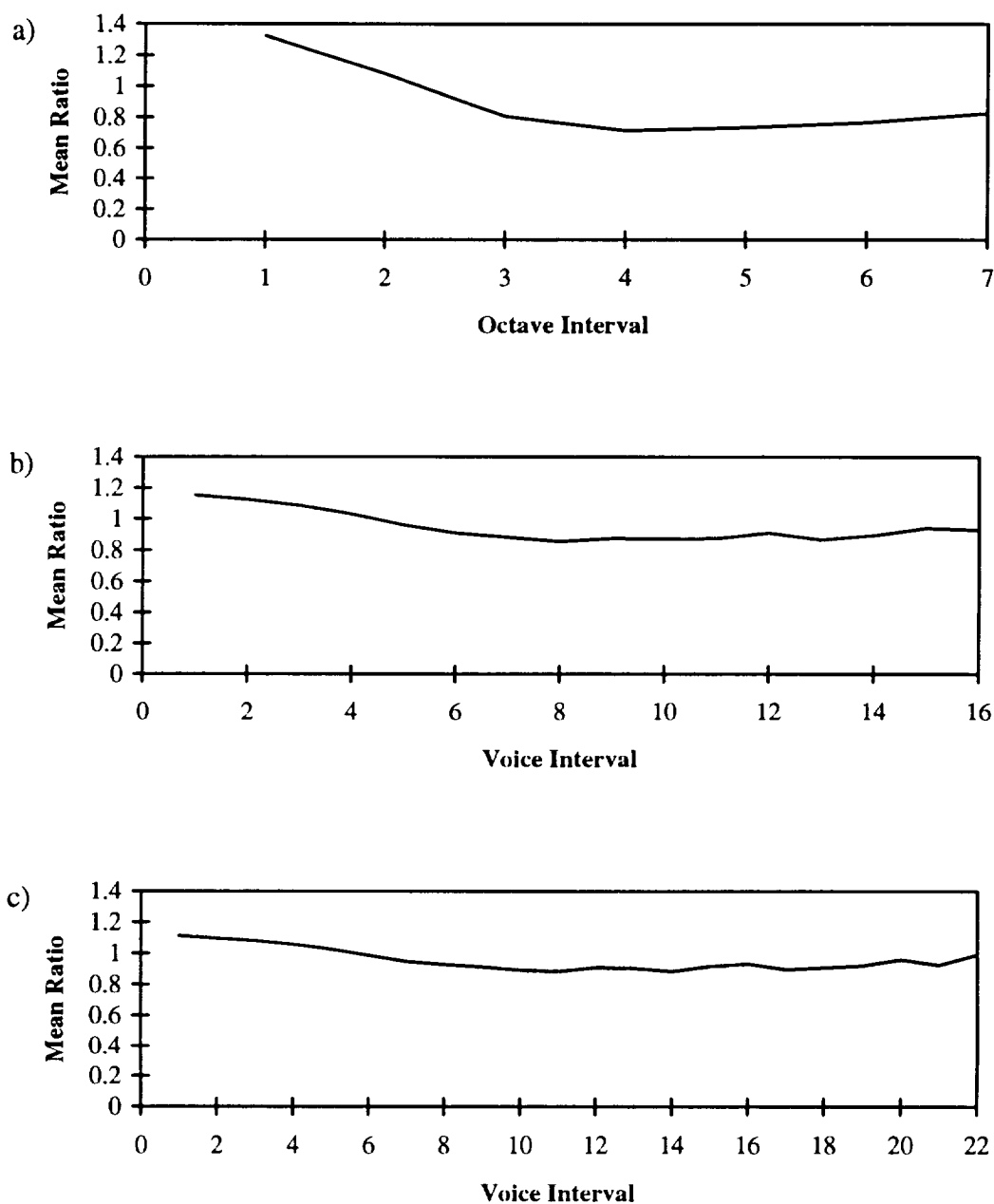
Figure 6.10 Mean ratios of for the (a) octave ratios, (b) interval of five voices ratios, and (c) interval of four voices ratios. The horizontal axis is each standard deviation ratio starting from the smallest scale ratioed to the next sized scale at the left up to the ratio of the largest scales at the right.

CHAPTER 7. SUMMARY AND CONCLUSION

Two different studies have been conducted to look at clouds and their effect on the atmosphere. The goal of the first study was to examine the radiative properties of the cloud through the use of Monte Carlo models. A focus was given especially to the absorption of photons in the visible and near-infrared part of the spectrum. This was due to recent findings of clouds absorbing more solar radiation than previously determined from radiative transfer theory. The second study focused more on the inhomogeneous nature of the cloud in order to find some relationship between the spectral scales within the cloud itself. This part of the study used both Fourier and wavelet transforms to decompose the clouds into frequency space.

In the first study the Monte Carlo looked first at absorption by a cloud that became progressively more inhomogeneous by the use of a cloud model cascade routine. From the result of the mean system absorptance, reflectance and transmittance, as the cloud became more inhomogeneous both the absorption and reflection of photons decreased while the transmittance increased. This indicates that the excess absorption observed from clouds may not be due to their inhomogeneity. The cloud forcing ratio remained basically unchanged giving indication that the absorption remained the same. This showed that the cloud forcing ratio does not become affected by increases or decreases in the inhomogeneity of the cloud.

The next step was to look at how the cloud absorbs solar and infrared radiation for two cases in a simplified cloud model. The simplified cloud model was a cloud/clear system where the cloud was considered homogeneous. Monte Carlo runs were made for different geometric and optical properties of the cloud. The first case examined absorption for a cloud that has conservative droplet scattering for different vapor

absorption potentials, and the second case looked at absorption by cloud droplets but not for vapor in the vapor absorption windows. Both cases were considered similar to looking at the absorption in visible and near-infrared wavelengths for vapor and liquid water.

The first focus of the simplified cloud model analysis was to examine how the local absorptance of solar radiation in clouds is calculated given local reflectance and local transmittance. It was concluded that the apparent absorptance was not always correct when calculated for non plane-parallel cloud systems, giving negative absorptances. The next step was to test a correction method for calculating near-infrared absorptances introduced by Ackerman and Cox (1982) and used by Hayasaka et al. (1995). The correction method worked well for nearly plane parallel clouds where the optical properties are homogeneous in the first case. It did not work well in the second case for near plane-parallel clouds by overestimating the absorption in the clear portions and causing large errors. The correction method when compared to actual absorptances from the Monte Carlo was found to overestimate and underestimate the absorptance at a cloud edge especially for the second case. These Monte Carlo cases dealt with specific spectral regions and concluded that much caution should be used when using the correction method, or similar correction methods for spectral regions. On the other hand Hayasaka et al. (1995) found the correction method to work well across the broad band. The correction method was found to not give reliable results for a cloud field with broken cloud cover.

From the Monte Carlo model calculations the mean absorptance and reflectance were plotted against the cloud fraction for both studies (Figures 3.45 to 3.48) for all cloud geometries and optical properties. From these plots the ratio of the effective cloud fraction to the actual cloud fraction, N_e/N_c, could be examined from both the perspective of the reflectance and the absorptance. For the first case the ratio determined by the absorptance was found to be near unity for smaller single scatter albedos, which agreed with that found by the reflectance. This was not true for the second case, the absorptance plots showed that as the cloud's single scatter albedo decreased the ratio increased away

from unity especially for clouds with higher aspect ratios. The reflectance for the second case indicated that the ratio was greater than unity but was decreasing toward unity instead of increasing. This created a contradiction between the reflectance and absorptance on the size of the effective cloud fraction.

The next focus was on the edge of the cloud in the simplified cloud model. From the transmittance and reflectance plots (Figures 3.5-3.28 a and b) the edge of the cloud could be detected due to the photons leaking into that part of the system and causing a maximum, or spike, to develop. This was especially evident from the Monte Carlo runs where conservative scattering was assumed for modeling visible wavelengths. The reflectance was considered to be the more important radiative property since this is what the satellite will see in the visible and near-infrared. The cloud edge became harder to detect due to two different effects, geometric effects and radiative effects. As the cloud's aspect ratio increased, the maximum in reflectance moved from the edge of the cloud to the center of the cloud making it harder to determine. Also as the cloud's absorption ability was increased to model near-infrared wavelengths, the spike decreased to where it would flatten out for the more absorbing clouds, i.e. lower single scatter albedos. Since there can be an overestimate of retrieved optical depths at cloud edges from satellites, it was concluded that a correction could be applied by comparing visible and near-infrared channels. It was suggested that the comparison be done by focusing on the difference in magnitude of the spike at the two different wavelengths.

Future work with the Monte Carlo will be to examine the broad band effects, and that more study could be done on the effective cloud fraction. The first part is to examine the correction method for use across the broad band and to confirm Hayasaka et al.'s (1995) results. For the effective cloud fraction the ratio from both reflectance and absorptance needs to be examined at other zenith and azimuth angles.

Also, and more importantly, future work will focus on examining the excess absorption in specific spectral regions. Since studying the inhomogeneity of clouds was found to give a decrease in absorption and not an excess the next step is to look at the absorption of solar radiation in specific spectral regions (Harshvardhan et al., 1996).

The second study examined the inhomogeneous nature of clouds focusing on the relationship of the scales, or wavelengths, of a cloud in frequency space. The analysis examined one dimensional LWC data taken during the ASTEX project with a PVM-100A probe (Gerber et al., 1994). The data was chosen to represent a marine stratocumulus cloud. To do the analysis both Fourier and continuous wavelet transforms were used to break the data up into different scales. The slope of the power spectrum, calculated from the Fourier transforms, was found to have an absolute value greater than the 5/3 rule, this indicated that the energy in the cloud is not evenly distributed among the scales. Since the slope is greater than 5/3 it can be said that there is more energy in the larger scales than in the smaller scales. This was confirmed by the wavelet transform modulus scalograms, which represents the energy of each scale in a two dimensional format. Since comparing the variability of two scales is similar to comparing the energy of two scales the standard deviation of smaller scales was compared to the standard deviation at larger scales for all data samples. The variability comparison found that the energy was greater at the larger scales.

Future work with the wavelet transforms would be to look at a comparison of the variability at two different scales for localized sections of the scalogram. For this study the standard deviation was calculated for all the coefficients in each scale of the scalogram. Due to the ability of wavelets to do analysis for a specific time or spatial location in a scale the next logical step would be to compare the variability at specific locations within the scalogram.

LIST OF REFERENCES

LIST OF REFERENCES

Ackerman, S. A. and S. K. Cox, 1982: Aircraft Observations of the Shortwave Fractional Absorptance of Non-Homogeneous Clouds. *J. Appl. Meteor.*, **20**, 1510-1515.

Albrecht, B. A., C. S. Bretherton, D. Johnson, W. H. Scubert, and A. S. Frisch, 1995: The Atlantic Stratocumulus Transition Experiment-ASTEX, *Bull. Amer. Meter. Soc.*, **76**, 889-904.

Binder, K., 1984: *Topics in Current Physics, Applications of the Monte Carlo Method in Statistical Physics.* Springer-Verlag, 311 pp.

Cahalan, R. F., W. Ridgway, W. J. Wiscombe, T. L. Bell, and J. B. Snider, 1994a: The Albedo of Fractal Stratocumulus Clouds. *J. Atmos. Sci.*, **51**, 2434-2455.

Cahalan, R. F., W. Ridgway, W. J. Wiscombe, S. Gollmer, and Harshvardhan, 1994b: Independent Pixel and Monte Carlo Estimates of Stratocumulus Albedo. *J. Atmos. Sci.*, **51**, 3776-3790.

Cess, R. D., M. H. Zhang, P. Minnis, L. Corsetti, E. G. Dutton, B. W. Forgan, D. P. Garber, W. L. Gates, J. J. Hack, E. F. Harrison, X. Jing, J. T. Kiehl, C. N. Long, J.-J. Morcrette, G. L. Potter, V. Ramanathan, B. Subasilar, C. H. Whitlock, D. F. Young, and Y. Zhou, 1995: Absorption of Solar Radiation by Clouds: Observations Versus Models. *Science*, **267**, 496-499.

Chou, M.-D, A. Arking, J. Otterman, and W. L. Ridgway, 1995: The Effect of Clouds on Atmospheric Absorption of Solar Radiation. *Geophys. Res. Lett.*, **22**, 1885-1888.

Chui, C. K., 1992: *An Introduction to Wavelets.* Academic Press, 266 pp.

Combes, J. M., A. Grossmann, and Ph. Tchamitchian, 1989: *Wavelets Time-Frequency Methods and Phase Space.* Springer-Verlag, 315 pp.

Daubechies, I., 1992: *Ten Lectures on Wavelets.* Capital City Press, 357 pp.

Davies, R, W. L. Ridgway, and K.-E. Kim, 1984: Spectral Absorption of Solar Radiation in Cloudy Atmospheres: A 20 cm^{-1} Model. *J. Atmos. Sci.*, **41**, 2126-2137.

Davis, A, A. Marshak, W Wiscombe, and R. Cahalan, 1994: Multifractal Characterizations of Nonstationarity and Intermittency in Geophysical Fields: Observed, Retrieved, or Simulated. *J. Geophys. Res.*, **99** (D4), 8055-8072.

Davis, A, A. Marshak, W. Wiscombe, and R. Cahalan, 1996: Scale Invariance of Liquid Water Distributions in Marine Stratocumulus. Part I: Spectral Properties and Stationarity Issues. *J. Atmos. Sci.*, **53**, 1538-1558.

Davis, J. M., S. K. Cox, and T. B. McKee, 1979: Vertical and Horizontal Distributions of Solar Absorption in Finite Clouds. *J. Atmos. Sci.*, **36**, 1976-1984.

Espinoza, R. C., Jr., and Harshvardhan, 1996: Parameterization of Solar Near Infrared Radiative   Properties of Cloudy Layers. *J. Atmos. Sci*, **53**, 1559-1568.

Farge, M., 1992: The Continuous Wavelet Transform of Two-Dimesional Turbulent Flows. *Wavelets and Their Applications*, M B. Ruskai, G. Beylkin, R. Coifman, I. Daubechies, S. Mallat, Y. Meyer, and L. Raphael, Eds., Jones and Bartlett Publishers, 275-302.

Fritz, S., and T. H. MacDonald, 1951: Measurements of Absorption of Solar Radiation by Clouds. *Bull. Amer. Meteor. Soc.*, **32**, 205-209.

Gerber, H., 1992: New Microphysics Sensor for Aircraft Use. *Proc. 11th Int. Conf. Clouds and Precipitation*, Motreal, 1992, 942-944.

Gerber, H., 1991: Direct Measurement of Suspended Particle Volume Concentration and Far-Infrared Extinction Coefficient With a Laser-Diffraction Instrument. *Appl. Opt.*, **30**, 4824-4831.

Gerber, H., B. G. Arends, and A. S. Ackerman, 1994: New Microphysics Sensor for Aircraft Use. *Atmospheric Research*, **31**, 235-252.

Gollmer, S. M., 1994: *Wavelet Analysis and Modelin of Marine Stratocumulus Inhomogeneity*. Doctoral Thesis, 198 pp.

Gollmer, S. M., Harshvardhan, R. F. Cahalan, and J. B. Snider, 1995: Windowed and Wavelet Analysis of Marine Stratocumulus Cloud Inhomogeneity. *J. Atmos. Sci.*, **52**, 3013-3030.

Grossmann, A. and J. Morlet, 1984: Decomposition of Hardy Functions Into Square Integrable Wavelets of Constant Shape. *SIAM J. Math. Anal.*, **15**, 723-736.

Harshvardhan, and R. W. L. Thomas, 1984: Solar Reflection from Interacting and Shadowing Cloud Elements. *J. Geophys. Res.*, **89 (D5)**, 7179-7185.

Harsvardhan, W. Ridgway, V. Ramaswamy, S. M. Freidenreich, and M. Batey, 1996: Solar Absorption in Cloudy Atmospheres. *Proc. 7th Symp on Global Change Studies*, 127-133.

Hayasaka, T, N, Kikuchi, and M. Tanaka, 1995: Absorption of Solar Radiation by Stratocumulus Clouds: Aircraft Measurements and Theoretical Calculations. *J. Appl. Meteor.*, **34**, 1047-1055.

Kolmogorov, A. N., 1941: Local Structure of Turbulence in an Incompressible Liquid for Very Large Reynolds Number. *Dokl. Akad. Nauk SSSR*, **30**, 299-303.

Kumar, P., and E. Foufoula-Georgiou, 1994: *Wavelets in Geophysics*. Academic Press, 373 pp.

Lau, K.-M., and H. Weng, 1995: Climate Signal Detection Using Wavelet Transform: How to Make a Time Series Sing. *Bull. Amer. Meter. Soc.*, **76**, 2391-2402.

Mallat, S. G., 1989: A Theory for Multiresolution Signal Decomposition: The Wavelet Representation. *IEEE Trans. on Pattern Anal. and Mach. Intel.*, **11** (7), 674-693.

Marchuk, G., G. Mikhailov, M. Nazareliev, R. Darbinjan, B, Kargin, and B. Elepov, 1980: *The Monte Carlo Methods in Atmospheric Optics*, Spriger-Verlag, 208pp.

Marshak, A., A. Davis, W. Wiscombe, and G. Titov, 1995a: The Verisimilitude of the Independent Pixel Approximation Used in Cloud Remote Sensing. *Remote Sens. Environ.*, **52**, 71-78.

Marshak, A., A. Davis, W. Wiscombe, and R. Cahalan, 1995b: Radiative Smoothing in Fractal clouds. *J. Geophys. Res.*, **100** (D12), 26247-26261.

Meyers, S. D., B. G. Kelly, and J. J. O'Brien, 1993: An Introduction to Wavelet Analysis in Oceanography and Meteorology: With Application to the Dispersion of Yanai Waves. *Mon. Wea. Rev.*, **121**, 2858-2866.

Morlet, J. G., A. E. Fourgeau, and D. Giard, 1982a: Wave Propogation and Sampling Theory - Part 1: Complex Signal and Scattering in Multilayered Media. *Geophysics*, **47**, 203-221.

Morlet, J. G., A. E. Fourgeau, and D. Giard, 1982b: Wave Propogation and Sampling Theory - Part 2: Sampling Theory and Complex Waves. *Geophysics*, **47**, 222-236.

Pilewskie, P., and F. P. J. Valero, 1995: Direct Observations of Excess Solar Absorption by Clouds. *Science*, **267**, 1626-1629.

Ramanathan, V., B. Subasilar, G. L. Zhang, W. Conant, R. D. Cess, J. T. Kiehl, H. Grassl, and L. Shi, 1995: Warm Pool Heat Budget and Shortwave Cloud Forcing: A Missing Physics? *Science*, **267**, 499-503.

Rioul, O., and M. Vetterli, 1991: Wavelets and Signal Processing. *IEEE Signal Processing Magazine*, **8** (10), 14-38.

Spedding, G. R., F. K. Browand, N. E. Huang, and S. R. Long, 1993: A 2-D Complex Wavelet Analysis of an Unsteady Wind-Generated Surface Wave Field. *Dynamics of Atmospheres and Oceans*, **20**, 55-77.

Stephens, G. L., and S.-C. Tsay, 1990: On the Cloud Absorption Anomaly. *Quart. J. Roy. Meteor. Soc.*, **116**, 671-704.

Weng, H., and K.-M. Lau, 1994: Wavelets, Period Doubling, and Time-Frequency Localization with Application to Organization of Convection over the Tropical Western Pacific. *J. Atmos. Sci.*, **51**, 2523-2541.

Wertheimer, A. L. and W. L. Wilcock, 1976: Light Scattering Measurements of Particle Distributions. *Appl. Opt.*, **15**, 1616-1620.